Project No. 11-3099

Laser-Arc Hybrid Welding of Thick Section Ni-base Alloys – Advanced Modeling and Experiments

Nuclear Energy Enabling Technologies

Dr. Tarasankar Debroy
Pennsylvania State University

In collaboration with:
Oak Ridge National Laboratory

Alison Hahn, Federal POC
Jack Lance, Technical POC

Nuclear Energy University Programs
U.S. Department of Energy

Final Report Abstract
Laser-Arc Hybrid Welding of Thick Section Ni-base Alloys – Advanced Modeling and Experiments
The Pennsylvania State University

Hybrid laser-arc welding of nickel-base alloys can increase productivity and decrease costs during construction and repair of critical components in nuclear power plants. However, laser and hybrid welding of nickel-base alloys is not well understood. This project sought to understand the physical processes during hybrid welding necessary to fabricate quality joints in Alloy 690, a Ni-Cr-Fe alloy. This document presents a summary of the data and results collected over the course of the project. The supporting documents are a collection of the research that has been or will be published in peer-reviewed journals along with a report from the partner at the national lab.

Understanding the solidification behavior of Alloy 690 is important for knowing the final properties of the weldment. A study was undertaken to calculate the solidification parameters, such as temperature gradient, solidification rate, and cooling rate in Alloy 690 welds. With this information and measured cell and dendrite arm spacings, an Alloy 690 map was constructed to guide process parameter development and interpret fusion zones in later hybrid welds. This research is contained in “Solidification Map of a Nickel Base Alloy.”

The keyhole formed under high laser intensity gives the hybrid welding technique the greater penetration depths compared to arc welding. However, keyhole behavior can form defects in the material, so knowing transient keyhole characteristics is important. With international collaborators, a study was undertaken to validate a new process monitoring tool known as inline coherent imaging (ICI), which is able to measure the keyhole depth with spatial and temporal resolutions on the order of 10 microns and 10 microseconds. ICI was validated for five alloy systems, including Alloy 690. Additionally, the keyhole growth rates at the start of welding were measured with unprecedented accuracy. This research is contained in “Real Time Monitoring of Laser Beam Welding Keyhole Depth by Laser Interferometry.”

During full penetration welding of thick sections, root defects can form, which result in unacceptable weld quality. A study was undertaken to determine the competing forces in root defect formation by independently changing the weight forces and surface tension forces. The weight force was altered by changing the plate thickness, and the surface tension force was altered by changing the surface condition at the bottom surface. Root defects do depend on these two forces. This research is contained in “Mitigation of Root Defect in Laser and Hybrid Laser-Arc Welding.”

Validation of the hybrid laser-arc model is necessary to properly model heat and mass transfer and fluid flow in Alloy 690 hybrid welds. Therefore, the developed model was validated for low

carbon steel. Temperatures calculated by the model were included into a microstructural model in order to calculate the phase fractions. Process maps were developed for the selection of welding parameters to avoid martensite formation. This research is contained in “Fusion Zone Microstructure in Full Penetration Laser-Arc Hybrid Welding of Low Alloy Steel.”

Alloy 690 suffers from ductility dip cracking, a form of hot cracking. This type of cracking inhibits the use of multipass welding to join Alloy 690. Our partners at ORNL performed some hot ductility testing with Alloy 690 samples using digital image correlation. The results of this work is contained in the report “Summary of 690 ductility dip cracking testing using Gleeble and digital image correlation.”

Macro-porosity is a limiting factor in the widespread deployment of laser and hybrid laser-arc welding for construction and repair of nuclear power plant components. Keyhole instability and fluctuation results in the formation of large bubbles, which become trapped at the advancing solid-liquid interface as pores. Laser and hybrid laser-arc welds were fabricated for a range of conditions. Porosity levels in the welds were measured in X-ray computed tomography (CT), which provides very detailed data on the size and locations of the pores inside the weld. Based on the porosity size and location distributions, the mechanism that leads to lower porosity in higher power hybrid-laser arc welds was determined. This research is explained in detail in “Porosity in Thick Alloy 690 Welds – Experiments, Modeling, Mechanism, and Remedy”.

Objectives and Accomplishments

1. Process Development and Weld Characterization

Parameters were developed for the successful laser and hybrid laser-gas metal arc (GMA) welding of Alloy 690. Dozens of trial GMA welds were fabricated to determine the correct voltage, current, wire feed speed, shielding gas composition, and torch angle for successful welding of Alloy 690 with different consumables. The correct GMA conditions were combined with a laser to perform the first hybrid laser-GMA welds on Alloy 690.

The resulting welds were characterized in terms of welding defects, such as pores, root defects, ductility dip cracks, and solidification cracks. The fusion zone profile and solidification structures were also analyzed. Micro-hardness measurements were performed on the welds to determine the effect of welding on mechanical properties.

Appendices A, B, C, and D provide additional details on welding process development and weld characterization.

2. Heat and Fluid Flow and Thermal Cycle Modelling

An existing heat transfer and fluid flow model was adapted to calculate the temperature and fluid velocity fields during laser welding of Alloy 690. Thermal cycles, cooling rates, temperature gradients, solidification rates, solidification morphology parameters, and spatial variation of solidification parameters were calculated using the adapted model, which models the keyhole heat source with a point by point heat balance at the keyhole walls.

Additional developments led to a heat transfer and fluid flow model for the simulation of hybrid laser-GMA welding, which requires the introduction of a volumetric heat source to model the addition of a consumable electrode into the weld pool. The temperature outputs were coupled with a microstructure model to accurately predict the effects of welding speed and laser-arc separation distance on the resulting microstructure in full penetration welds. This work led to process maps demonstrating the effects of different process parameters on final microstructure.

Appendices A and D provide additional details on heat and fluid flow and thermal cycle modeling.

3. Solidification and Microsegregation

Solidification of Alloy 690 welds was thoroughly characterized in terms of spatial variations of scale and morphology (i.e. cells and columnar dendrites). The sizes and morphologies were correlated to the calculated cooling rates and morphology parameters from the heat transfer and fluid flow model. This correlation was used to construct a solidification map for Alloy 690 showing the effects of temperature gradients and solidification rates on scale and morphology of the solidification structures.

Scheil calculations predicted limited partitioning of alloying elements to the liquid during solidification. A slight increase in chromium was expected. The small interdendritic regions and EDS analysis confirmed that microsegregation was limited in Alloy 690 compared to other nickel-base alloys.

Appendix A provides additional details on solidification and microsegregation Please refer to appendix A for more information.

4. Calculation and Measurement of Residual Stress

Great progress has been made with the calculation of residual stress fields. A key ingredient for these calculations is knowledge of the 3D temperature fields during welding. These fields have been determined for number laser and hybrid laser-arc welding conditions. Depending on the heating and cooling rates, the residual stress fields will differ. The spallation neutron source at Oak Ridge National Lab can be used to measure residual stress fields. Diffraction of the neutrons at the weld sample can be translated into residual stress. A proposal was written and revised in order to obtain beam time at the spallation neutron source. Unfortunately, the proposal was not selected over the course of three reviews.

5. Mechanical Property Testing

Extensive mechanical property testing was undertaken at Oak Ridge National Lab (ORNL). As-machined and annealed testing samples were mechanically tested at room temperature. A hot ductility test was performed where the sample is rapidly heated and cooled at rates up to 110˚C/s and then strained to fracture at 871˚C in a Gleeble thermos-mechanical simulator. During testing digital image correlation (DIC) was used to measure the local strain field near the location of failure. The initial speckle pattern application procedure for DIC was not appropriate for the high temperatures, which were tested in this study. So, the co-investigators at ORNL developed a new coating technique, which can withstand higher testing temperatures. Appendix E provides additional details on mechanical property testing.

Publications and Presentations

J.J. Blecher, T.A. Palmer, and T. DebRoy, “Porosity in Thick Alloy 690 Welds – Experiments, Modeling, Mechanism, and Remedy”, in preparation.

H.L. Wei, J.J. Blecher, T.A. Palmer, and T. DebRoy, “Fusion Zone Microstructure in Full Penetration Laser-Arc Hybrid Welding of Low Alloy Steel”, *Welding Journal*, **94**, 135s-144s (2015).

J.J. Blecher, T.A. Palmer, and T. DebRoy, “Mitigation of Root Defect in Laser and Hybrid Laser-Arc Welding”, *Welding Journal*, **94**, 73s-82s (2015).

J.J. Blecher, C.M. Galbraith, C. Van Vlack, T.A. Palmer, J.M. Fraser, P.J.L. Webster, and T. DebRoy, ‘Real Time Monitoring of Laser Beam Welding Keyhole Depth by Laser Interferometry,’ *Science and Technology of Welding and Joining*, **19**, 560-564 (2014).

J.J. Blecher, T.A. Palmer, and T. DebRoy, ‘Solidification Map of a Nickel Base Alloy,’ *Metallurgical and Materials Transactions A*, **45A**, 2142-2151 (2014).

J.J. Blecher, T.A. Palmer, and T. DebRoy, ‘Root Defects in Laser and Hybrid Laser-Arc Welds,’ presented at AWS Professional Program at FABTECH, 2014, 11 – 13 November 2014, Atlanta, GA.

J.J. Blecher, H. Wei, T.A. Palmer, and T. DebRoy, ‘Solidification in High-Power Laser Welding of Inconel® Alloy 690,’ presented at AWS Professional Program at FABTECH, 2013, 18 – 21 November 2013, Chicago, IL.

U.S. DEPARTMENT OF ENERGY
Nuclear Energy

Laser-Arc Hybrid Welding of Thick Section Ni-base Alloys – Advanced Modeling and Experiments

OVERVIEW

Purpose: This work seeks to demonstrate the utility of laser-GMA hybrid welding to thick sections of Ni-base alloys through numerical modeling of the heat transport, fluid flow, solidification, and residual stress.

Objectives:

- Perform laser-GMA hybrid welds on Inconel Alloy 690 with various filler metals.
- Characterize resulting microstructure and segregation of the alloying elements in the fusion zone.
- Develop an existing heat transfer and fluid flow model to understand the phenomena that occur during laser-GMA hybrid welding.
- Calculate and measure the residual welding stress field.
- Measure the mechanical properties of the weld.

IMPACT

Logical Path:

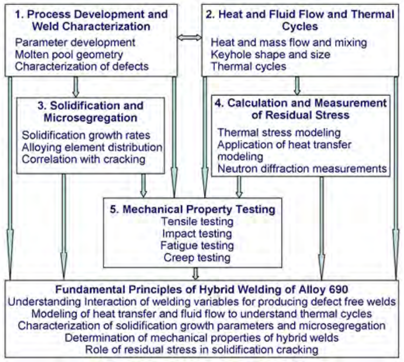

1. Process Development and Weld Characterization
Parameter development
Molten pool geometry
Characterization of defects

2. Heat and Fluid Flow and Thermal Cycles
Heat and mass flow and mixing
Keyhole shape and size
Thermal cycles

3. Solidification and Microsegregation
Solidification growth rates
Alloying element distribution
Correlation with cracking

4. Calculation and Measurement of Residual Stress
Thermal stress modeling
Application of heat transfer modeling
Neutron diffraction measurements

5. Mechanical Property Testing
Tensile testing
Impact testing
Fatigue testing
Creep testing

Fundamental Principles of Hybrid Welding of Alloy 690
Understanding Interaction of welding variables for producing defect free welds
Modeling of heat transfer and fluid flow to understand thermal cycles
Characterization of solidification growth parameters and microsegregation
Determination of mechanical properties of hybrid welds
Role of residual stress in solidification cracking

Outcomes: The outcomes of this work include a quantitative understanding of the laser-GMA hybrid welding process of Alloy 690. The effect of welding conditions on weld pool geometry, solidification parameters, microsegregation, residual stress fields, mass transport, and mechanical properties will be determined.

DETAILS

Principal Investigator: Dr. Tarasankar DebRoy

Institution: The Pennsylvania State University

Collaborators: Dr. T.A. Palmer (ARL/PSU) and Dr. W. Zhang (OSU)

Duration: Oct. 2011 to Dec. 2014

TPOC: Herschel Smartt

Workscope: MS-NT4

Project Number #:
120327

Total Funding Level: $482,503

RESULTS

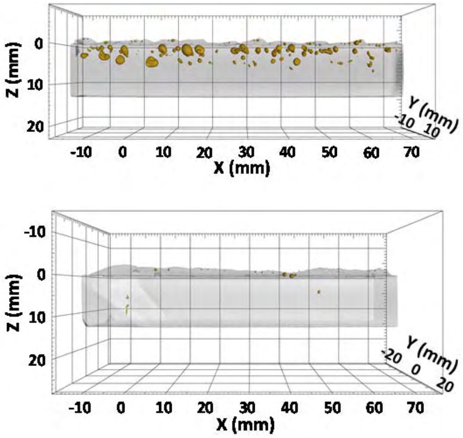

Accomplishments: A manuscript describing the differences between laser and hybrid laser-arc welding is in preparation. One of the differences discussed is the effect of technique on keyhole porosity as shown above in the X-ray CT images. The top image is a laser weld. The bottom image is a hybrid weld.

Appendix A:

Solidification Map of a Nickel-Base Alloy

Solidification Map of a Nickel-Base Alloy

J.J. BLECHER, T.A. PALMER, and T. DEBROY

The solidification behavior of the advanced nickel-base alloys, such as Inconel® Alloy 690, is important for understanding their microstructure, properties, and eventual service behavior in nuclear power plant components. Here, an experimental and theoretical program of research is undertaken with the aim of developing a quantitative understanding of the solidification behavior under a wide range of temperature gradients and solidification growth rates. The temperature gradient and solidification rates vary spatially by several orders of magnitude during keyhole mode laser welding. Therefore, the solidification structure is experimentally characterized from microscopic examinations of the resulting fusion zones and correlated with fundamental solidification parameters to provide a widely applicable solidification map that can be employed for a broad range of solidification processes. The cell and secondary dendrite arm spacings are quantitatively correlated with cooling rates. An Alloy 690 solidification map, which illustrates the effect of temperature gradient and solidification rate on the morphology and scale of the solidification structures, is also presented.

DOI: 10.1007/s11661-013-2149-1
© The Minerals, Metals & Materials Society and ASM International 2013

I. INTRODUCTION

HIGH performance nickel-base alloys are widely used in industry[1–5] because of their superior structural stability, desirable mechanical properties, and high resistance to stress corrosion cracking. For example, Inconel® Alloy 690, a high chromium content nickel-base alloy, is widely used in installation and repair of the steam generator tubing and pressurized water reactor components.[6] Fabrication and maintenance of these alloy parts require an understanding of their solidification behavior because of its significant impact on the mechanical properties. Unlike well established alloy systems, such as stainless steels,[7] a quantitative understanding of Alloy 690 solidification behavior is not currently available.

Previous studies on the solidification behavior of Alloy 690 have provided useful knowledge about the morphology of the solidification structure. Cellular and columnar dendritic structures were observed in both arc and laser welded fusion zones.[8–13] Characterization of the solidification structures showed that cell spacings and the secondary dendrite arm spacings varied with heat input per unit length during the fabrication process. The scale of the solidification structures were correlated with heat input because the heat input could be accurately determined. However, it is now well established that the heat input does not uniquely define the solidification structure because the same heat input can result in significantly different thermal conditions depending on the fabrication speed and the power used.[14]

The scale of the cells or dendrites depends primarily on the fundamental solidification parameters, such as the temperature gradient (G) and the solidification growth rate (R). The cooling rate can be directly related to the scale of the solidification structures, regardless of the heat input or other attributes of a fabrication process.[15] A morphological map showing solidification structures as a function of fundamental solidification parameters can provide significant benefits to the construction of new power plants and the refurbishment of existing plants. This enhanced understanding of the solidification mechanisms will lead to improved fabrication and performance of Alloy 690 in high temperature applications.

Realistic calculations of the solidification parameters during welding have been enabled by recent advances in numerical modeling. For example, Zhang *et al.*[16] utilized a heat transfer and fluid flow model and showed that calculated thermal cycles during cooling after arc spot welding agreed well with the corresponding experimental thermal cycles. Rai *et al.*[17–19] calculated G, R, GR, and the morphology parameter (G/R) at the trailing edge of the weld pool during laser welding of a wide range of alloys. Anderson *et al.*[5,20] made use of the columnar to equiaxed transition (CET) model[21–23] in order to study stray grain formation in single crystal alloys. Using coupled models, Tan *et al.*[24] determined the temperature field during laser spot welding of stainless steel to calculate a number of solidification characteristics, such as grain growth direction, morphology, and cell and secondary dendrite arm spacing. Numerical modeling has been used extensively to calculate solidification parameters[5,16–20,24] and to study the solidification behavior of alloys.

In this study, the solidification behavior of a Ni-Cr-Fe alloy, Alloy 690, is investigated based on experimentally determined solidification structure and theoretically

---

J.J. BLECHER, Ph.D. Candidate, T. DEBROY, Professor, and T.A. PALMER, Associate Professor, are with the Department of Materials Science and Engineering, The Pennsylvania State University, University Park, PA 16802. Contact e-mail: jjb5120@psu.edu

Manuscript submitted August 12, 2013.
Article published online December 24, 2013

calculated solidification parameters, such as temperature gradients and the solidification growth rates. During microscopic analysis, the laser welds exhibit a wide range of cellular and columnar dendritic structures across the fusion zone. The local temperature gradients and solidification rates during keyhole mode laser welding are calculated with a well-tested numerical heat transfer and fluid flow model. In addition, the scale of cellular and dendritic structures are then correlated to the cooling rates, allowing relations between cooling rate and cell and secondary dendrite arm spacing to be developed. The critical G/R parameter for the transition from cells to dendrites is then determined and used to calculate the area fractions of columnar dendrites in the transverse cross sections of the experimental fusion zones. A solidification map for Alloy 690 is then constructed to predict the formation of cells and dendrites and the scale of the cells and dendrite arms for given values of G and R.

II. EXPERIMENTS AND MODEL DEVELOPMENT

A. *Experimental Welds*

Autogenous bead-on-plate welds were made on 12.7 mm thick Inconel® Alloy 690 plate with an IPG Photonics® YLR-12000-L ytterbium fiber laser. The 1070 to 1100 nm wavelength laser light was directed to the workpiece through a 200 μm process fiber and focused with a YW50 Precitec® welding head. The optics included 200 mm focus length collimating and focusing lenses. Beam characterization with a PRIMES® Focus Monitor confirmed a 200 mm focus length, a 300 μm beam diameter at focus, and a divergence angle of 150 mrad. The focus plane of the laser beam was positioned at the surface of the workpiece with no offset. Laser power varied between 1.0 and 5.6 kW, and travel speed was held constant at 34 mm s^{-1}. The composition of the Alloy 690 plate is shown in Table I.

Standard metallographic techniques were used to prepare transverse sections of the laser welds. Electrolytic etching in 10 wt pct oxalic acid for several seconds revealed the microstructure of the fusion zone and base metal. A Nikon® Epiphot microscope imaged the microstructures at magnifications between 100 and 1000 times magnification. A Nikon® DS-Fi2 camera and Nikon® NIS Elements software were used to capture micrographs. Series of 10 to 30 images at 100 times magnification were stitched together into larger images using Adobe® Photoshop CS5. Secondary dendrite arm spacing, cell spacing, and morphology area measurements were performed with ImageJ software. The linear intercept method was used to measure the secondary arm spacings and cell spacings. Four measurements per micrograph at 1000 times magnification were used to determine cell spacings for each location and corresponding cooling rate. If one cell spacing measurement fell outside of the mean plus or minus one standard deviation, it was not included in the reported mean. The reported secondary arm spacings are an average of three or more measurements in one 1000 times magnification micrograph. Each dendrite used in the measurement had a minimum of seven arms.

B. *Mathematical Modeling and Solidification Calculations*

The three-dimensional (3D) finite difference based heat transfer and fluid flow model used in this paper has been documented elsewhere in the literature,[17–19,25–28] so only a brief description of the features will be presented here. Calculation of the keyhole profile is done before the heat transfer and fluid flow calculations and is based on the method proposed by Kaplan,[29] which performs a point by point heat balance at the keyhole wall. The profile and resulting heat flux at the keyhole wall are then incorporated into the heat transfer and fluid flow model as a heat source. The equations for the conservation of mass, momentum, and energy are solved for enthalpy and fluid velocity. The resulting temperature fields are used to determine the solidification parameters. The Alloy 690 material properties used for these calculations are shown in Table II.

The heat transfer and fluid flow model has been extensively evaluated and validated for keyhole mode laser beam welding for a variety of materials, including aluminum, stainless steel, tantalum, titanium, vanadium, and structural steel alloys.[17–19] In addition to accurately predicting the experimental weld pool dimensions for various welding powers, speeds, and laser beam profiles, the solidification parameters G, GR, and G/R were calculated at the weld centerline.[18] The model has also been employed to quantitatively study the solidification of austenitic stainless steels[35] and the effect of cooling rate on the primary solidification phase. The calculated and measured thermal cycles and cooling rates agreed, which allowed for the establishment of relations between cooling rates (1000 to 10,000 K s^{-1}) and spacings of primary and secondary dendrites.

The temperature gradient (G) and solidification growth rate (R) are calculated from the temperature field, which is output by the heat transfer and fluid flow model. These parameters, G and R, have been calculated for every position along the solidification front, which is a 3D surface from which the 2D transverse cross-section is extracted. The combined forms of G and R include the cooling rate (GR) and the solidification morphology parameter (G/R). The cooling rate can be directly

Table I. Composition of Alloy 690 Plate

Composition (Wt Pct)	Ni	Cr	Fe	Mn	Si	C	Cu	S
Alloy 690	59.96	29.62	9.68	0.19	0.08	0.03	<0.01	0.004

Table II. Material Properties of Alloy 690 Used in the Calculations

Material Property	Value	Reference
Absorptivity of liquid	0.313	[30]
Density of liquid at the melting point (kg m^{-3})	7500	[31]
Density of liquid at the boiling point (kg m^{-3})	6100	[31]
Viscosity of liquid (kg m^{-1} s^{-1})	0.0051	[31]
Solidus temperature [K (°C)]	1616 (1343)	[32]
Liquidus temperature [K (°C)]	1650 (1377)	[32]
Enthalpy of solid at solidus (kJ kg^{-1})	879	[33]
Enthalpy of liquid at liquidus (kJ kg^{-1})	1200	[33]
Specific heat of solid (J kg^{-1} K^{-1})	665	[33]
Specific heat of liquid (J kg^{-1} K^{-1})	673	[33]
Thermal conductivity of solid (J m^{-1} s^{-1} K^{-1})	33	[34]
Thermal conductivity of liquid (J m^{-1} s^{-1} K^{-1})	46	[31]
Thermal conductivity of liquid at boiling point (J m^{-1} s^{-1} K^{-1})	47	[31]
Coefficient of thermal expansion (K^{-1})	1.0×10^{-6}	[31]
Temperature coefficient of surface tension (mN m^{-1} K^{-1})	−0.37	[31]

related to the size of the features in the fusion zone. The morphology parameter can be used to describe the shape of the solidification structures, such as (from highest G/R value to lowest) planar, cellular, columnar dendritic, and equiaxed dendritic.

In order to calculate G and R, the direction of heat flow at the liquidus temperature must be determined, which is the gradient of the temperature field

$$\nabla T = \frac{\partial T}{\partial x} i + \frac{\partial T}{\partial y} j + \frac{\partial T}{\partial z} k, \qquad [1]$$

where T is temperature and i, j, and k are unit vectors in the x, y, and z direction, respectively. The heat flow direction at a certain position in space is expected to be normal to the 3D liquidus surface. The temperature gradient, G, is

$$G = \|\nabla T\| = \sqrt{\left(\frac{\partial T}{\partial x}\right)^2 + \left(\frac{\partial T}{\partial y}\right)^2 + \left(\frac{\partial T}{\partial z}\right)^2}, \qquad [2]$$

which is simply the magnitude of the vector. The solidification direction is assumed to be aligned opposite to the heat transfer direction. Therefore,

$$\cos \alpha = \frac{-\frac{\partial T}{\partial x}}{\|\nabla T\|}, \qquad [3]$$

where α is the angle between the welding direction and solidification growth direction. In order for the assumption to be valid, the orientation of the easy growth direction, $\langle 100 \rangle$, of the pre-existing grain must be parallel to the solidification direction. In polycrystalline material with randomly oriented grains, this condition is not usually met, however, with mean grain sizes much smaller than the dimensions of the weld, competitive growth will quickly select the best orientation during solidification. The solidification rate, R, is

$$R = U \cos \alpha, \qquad [4]$$

where U is the welding speed. Figure 1(a) shows the relationship between U, R, and α on the 3D solidification surface and the resulting transverse cross-section of the weld. The variation of α with depth along the central longitudinal plane for a 2.8 kW weld is shown in Figure 1(b). It should be noted that R is also a function of the angle between the easy growth direction of the grain and the welding direction. However, this angle is typically neglected for the case of polycrystalline materials.

III. RESULTS AND DISCUSSION

A. *Microstructural Characterization*

Bead-on-plate laser welds were made on Alloy 690 plates at a travel speed of 34 mm s^{-1} and powers ranging from 1.0 to 5.6 kW. The combination of laser power and welding speed resulted in the formation of a keyhole in each weld. Calculated temperature and fluid velocity fields are shown in Figure 2 for powers of 1.0, 2.8, and 4.7 kW. The boiling [3085 K (2812 °C)], liquidus [1650 K (1377 °C)], and solidus [1616 K (1343 °C)] temperature contours are plotted. The characteristic high depth to width ratio of keyhole mode laser weld pools is observed as is the Marangoni effect driven fluid flow, which drives molten metal to the edges of the pool. As expected, an increase in the laser power produces a larger pool overall. The width of the two phase mushy region also increases, which suggests different thermal cycles along the solidification front. A comparison of the experimental and calculated weld pool dimensions is shown in Figure 3. Good agreement is observed between both sets of values, except at the 5.6 kW width where material expulsion was observed. At powers exceeding 5.6 kW and up to 10.6 kW, significant liquid metal expulsion occurred, indicating the onset of drilling.

Examination of the fusion zone microstructure revealed two distinct morphologies, cells and columnar dendrites, and a range of scales. Figure 4 shows representative micrographs of cells and columnar dendrites in the transverse fusion zone of the 3.8 kW weld. The micrograph of the cells is taken near the root of the weld, where the scale of the cell spacing is about 3 μm due to the relatively high cooling rates. At this location, cell growth occurs in a variety of directions, and the cells

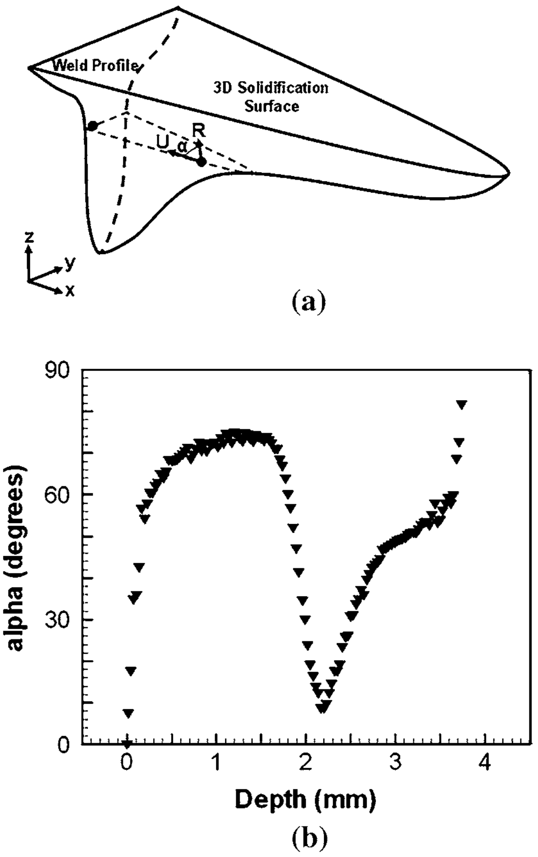

Fig. 1—The 3D solidification surface and resulting weld profile, (*a*), and variation of the angle α with depth along the central longitudinal plane for a 2.8 kW weld, (*b*), are shown. Also shown is the relationship between the welding speed, *U*, the solidification rate, *R*, and angle between the two vectors, α.

are elongated reaching lengths of 60 μm or longer. While not observable in Figure 4, some cells grew perpendicular to the transverse plane. On the other hand, columnar dendrites are located near the center of the weld finger and are much coarser than the cells with dendrite arm sizes of 4 to 5 μm. The middle and right hand side portion of Figure 4(b) shows well developed columnar dendrites, and left hand side shows tertiary dendrites and the weld centerline.

A broader overview of the 2.8 kW weld fusion zone along with the calculated solidification direction (*i.e.*, $-\nabla T$) is given in Figure 5. Overall, the general wineglass shape of keyhole mode laser welds is observed as well as some porosity near the bottom of the weld due to keyhole instability. In terms of cell, dendrite, and grain orientation, the direction of growth is a function of position in the weld. The calculated orientation vectors are shown as unit vectors, so in 3D, the vectors have the same magnitude. Small vectors indicate significant growth in the *x*-direction, perpendicular to the page. In the middle part of the weld finger, mainly horizontal growth dominates. For rest of the weld, the solidification structures grow vertically towards the top surface of the workpiece but to different degrees. At the top of the weld, growth is at 45 deg to the horizontal, while at the weld root growth is almost vertical.

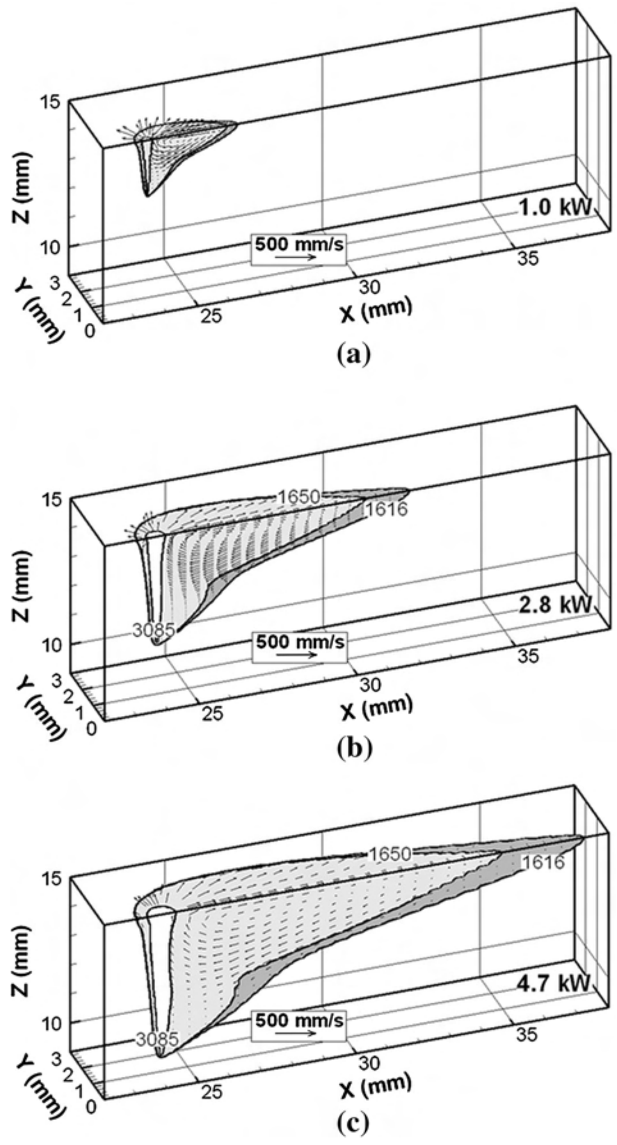

Fig. 2—The calculated molten pool profiles during keyhole mode laser welding are shown at different laser powers, (*a*) 1.0 kW, (*b*) 2.8 kW, and (*c*) 4.7 kW. The boiling point, liquidus temperature, and solidus temperatures are 3085 K, 1650 K, and 1616 K (2812 °C, 1377 °C, and 1343 °C), respectively. The fluid velocity reference vector of 500 mm s^{-1} is also shown.

The large spatial variation of solidification structure size and morphology in both the whole fusion zone and individual micrographs is illustrated in Figures 5(b) through (d). Part b shows the microstructure near the top of the weld. Cells and dendrites exist together in this micrograph with cells towards the left and dendrites in the center and towards the right. This spatial variation indicates that the morphology parameter G/R is decreasing from left to right in Figure 5(b). The orientation of growth becomes steeper from the fusion line to the center of the weld. Figure 5(c) also shows both cells and dendrites, but variation in scale is clear. Individual cells are barely resolved at the fusion line, while relatively large dendrite arms can be seen at the centerline. This observation indicates that the cooling rate has decreased dramatically from the fusion line to the centerline.

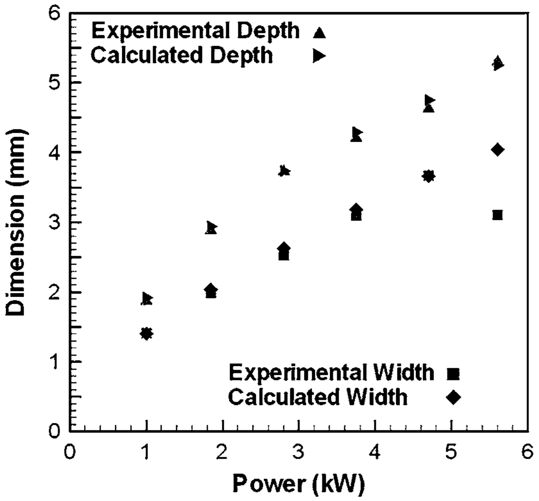

Fig. 3—The calculated and experimental molten pool dimensions are shown as a function of laser power for a travel speed of 34 m s^{-1}. The experimental and calculated molten pool widths and depths show good agreement.

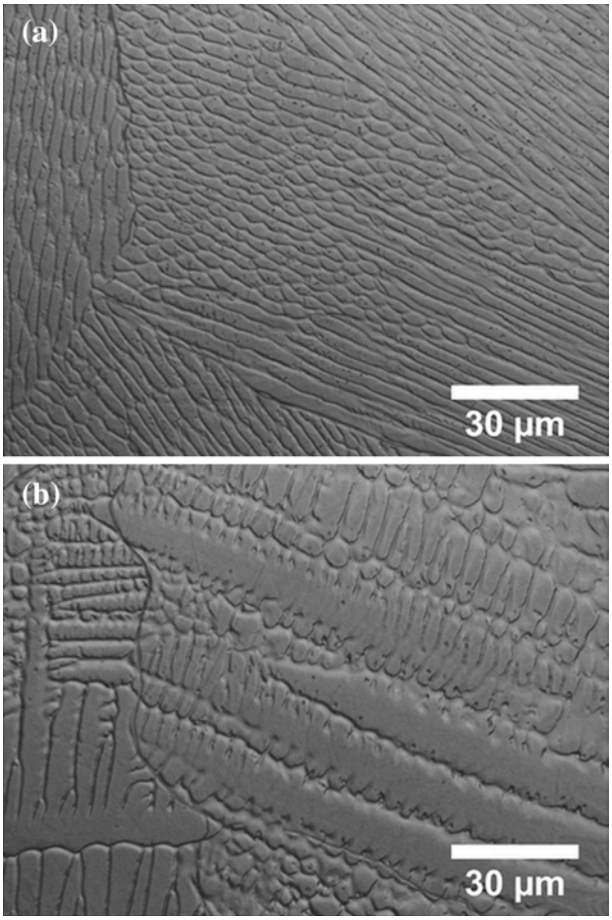

Fig. 4—The solidification structures observed in this study are (*a*) cells and (*b*) dendrites. The cells and dendrites near the root and center of the fusion zone, respectively, of a 3.8 kW weld are shown.

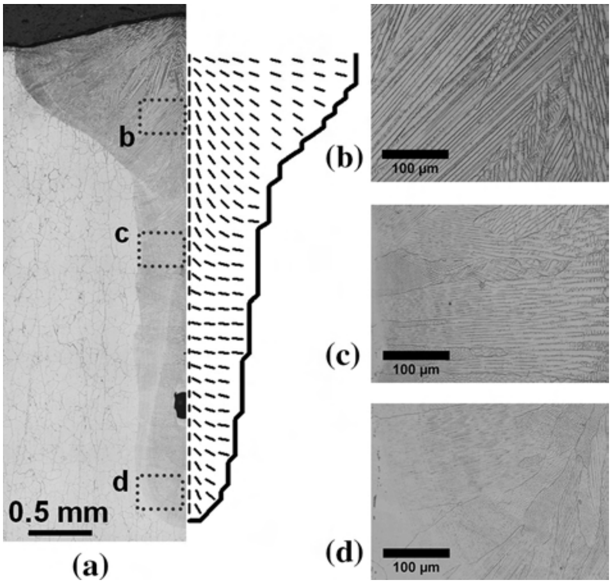

Fig. 5—The scale, mode, and orientation of solidification varies across the transverse section of the 2.8 kW weld. In (*a*) the general profile is shown with the positions of (*b*), (*c*), and (*d*) highlighted with rectangles. The calculated orientation of the solidifying cells, dendrites, and grains are shown in (a) based on the direction of heat flow at those positions.

Significant horizontal columnar dendrite growth is shown in Figure 5(c). Only fine cells growing in a nearly vertical direction are observed in Figure 5(d). This observation indicates relatively high values of GR and G/R are expected.

Qualitatively, the observed growth directions and calculated growth directions agreed well, indicating that the experimental and calculated heat transfer directions are quite close. While observation of the fusion zone indicates that G/R varied enough to produce cells and columnar dendrites, the variation was not significant enough to produce equiaxed dendrites or significant amounts of planar solidification, which is observable just at the edge of the fusion zone in Figure 5. With typical values for alloying element diffusion in liquid metal, the minimum G/R value necessary for planar solidification can be estimated[15] and is on the order of 7000 K s mm^{-2}. So, based on experimental observations, G/R is at least 7000 K s mm^{-2} at the edge of the fusion zone, but at all other locations, the value is less.

B. *Solidification Parameters*

Figure 6 illustrates the variation of G and R as a function of depth along the central x–z plane in a 2.8 kW weld. The weld pool profile along the central longitudinal plane is shown as well in order to demonstrate how the shape of the solidification front affects the solidification parameters. The direction of heat transfer, which is aligned to the solidification direction, can be discerned by the slope of the liquidus contour [1650 K (1377 °C)]. A more vertical slope (*i.e.*, the surface normal is closer aligned to the weld direction) produces a higher solidification rate. If the slope is close to zero, or the liquidus contour is nearly horizontal, the solidification rate is low. The magnitude of temperature gradient is qualitatively represented by how close the

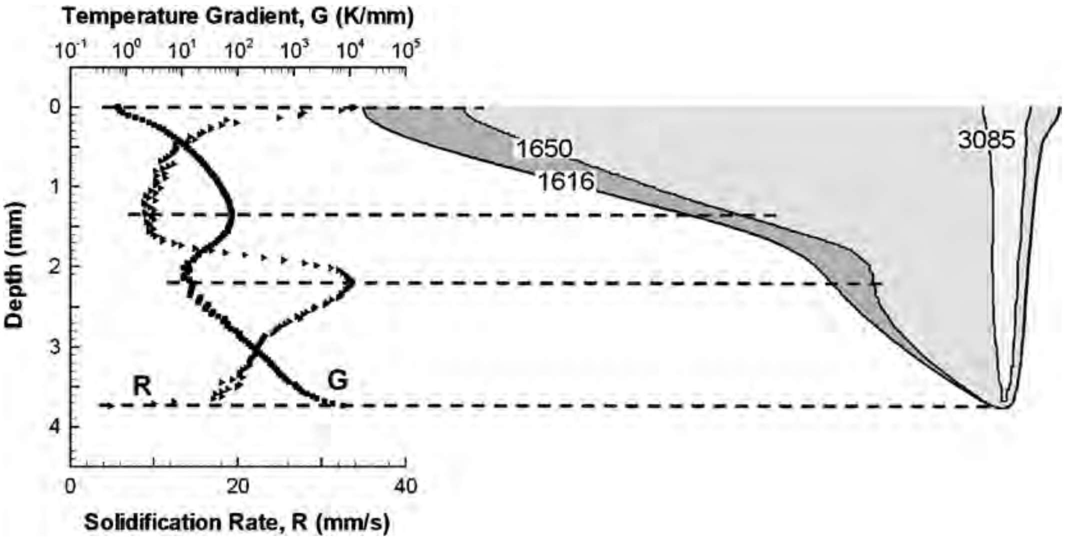

Fig. 6—The behavior of *G* and *R* as a function of depth along the central longitudinal plane for a 2.8 kW weld. The slope of the liquidus contour represents the solidification rate (*i.e.*, larger absolute slope, greater *R*), and the distance between the solidus and liquidus contours corresponds to the temperature gradient (*i.e.*, larger distance, lower *G*).

solidus and liquidus lines are to one another, or, alternatively, the width of the mushy zone. A larger mushy zone is associated with a lower temperature gradient.

In Figure 6, the slope of the liquidus contour and the width of the mushy zone decrease from the top to half the depth of the weld, which is represented by the increase in the temperature gradient and decrease in solidification rate. This behavior is typically observed in ellipsoidal weld pools produced by arcs and low intensity lasers.[36,37] However, due to the nature of the keyhole heat source, which extends into the depth of the weld pool, at half the depth along the weld centerline, both the verticality of the liquidus contour and mushy zone width increase sharply. This change results in a decrease of *G* and increase of *R*. These two characteristics, mushy zone width and liquidus contour slope, then decrease again as the liquidus contour approaches the bottom of the keyhole. Along the central *x*–*z* plane, the temperature gradient varies over four orders of magnitude from the top of the weld to the bottom, and the shapes of these two curves will impact the combined forms of *G* and *R*.

The temperature gradient (*G*) and solidification rate (*R*) along the central *x*–*z* plane for powers of 1.0, 2.8, and 4.7 kW and a travel speed of 34 mm s^{-1} are shown in Figure 7. Two-dimensional plots of *G* and *R* for the same powers are also shown. Each *G* curve exhibits a local minimum and maximum along the depth, and an increase in power tends to shift the curve down and increase the range over which *G* varies. For example, in the case of the 1 kW weld, the range over which *G* varies is three orders of magnitude, 10 to 10,000 K mm^{-1}, but for the 4.7 kW weld, *G* varies over four orders of magnitude from 0.2 K mm^{-1} at the top of the weld pool to 5000 K mm^{-1} near the bottom of the keyhole. A review of the temperature gradient plots inset in Figure 7(a) shows that increasing the power does not simply result in a larger weld profile with similar contours. At higher powers, lower temperature gradients and a higher degree of spatial variation are observed throughout the weld. Additionally, the higher temperature gradients are found near the fusion line and root of the weld, while the lower values are found near the top center.

In Figure 7(b), the solidification rate, *R*, varies from 4 to 34 mm s^{-1} (the welding speed). Similar to the *G* plots, a local minimum and maximum are observed. Power does not appear to have a significant effect on *R* at the central longitudinal plane. However in the 2D *R* plots, relatively lower solidification rates are observed at higher powers. In the 4.7 kW weld, *R* is mostly 5 mm s^{-1} or more at the top half, where in the 1.0 kW weld *R* is 20 mm s^{-1} or more. Along the cross section, *R* decreases from the center of the weld to the fusion line because the surface normal vector is becoming increasingly misaligned with the travel direction.

Both *G* and *R* exhibit complex behavior as a function of position along the solidification front and a high degree of spatial variability, which will lead to variability in the parameters that control solidification structure scale and morphology. Figure 8 shows *GR* and *G*/*R* as a function of depth along the central *x*–*z* axis and cross sections for 1.0, 2.8, and 4.7 kW. The shapes of the curves are similar to the previous plots of *G* and *R* with a local minimum and maximum near the half depth of the weld, and the curves tend to shift to lower values when the power increases. However, the values of *GR* and *G*/*R* are varying over four to five orders of magnitude. For 4.7 kW, the cooling rate varies from 6 to 40,000 K s^{-1}, and *G*/*R* varies from 0.005 to 600 K s mm^{-2}. The large spatial variation in cooling rates and *G*/*R* values explains the variation in scale and morphology observed in Figure 5.

The effect of laser power on the cooling rate can be observed in the inset contour plots. At 1.0 kW most of the weld is cooling at rates above 1000 K s^{-1}, but as the

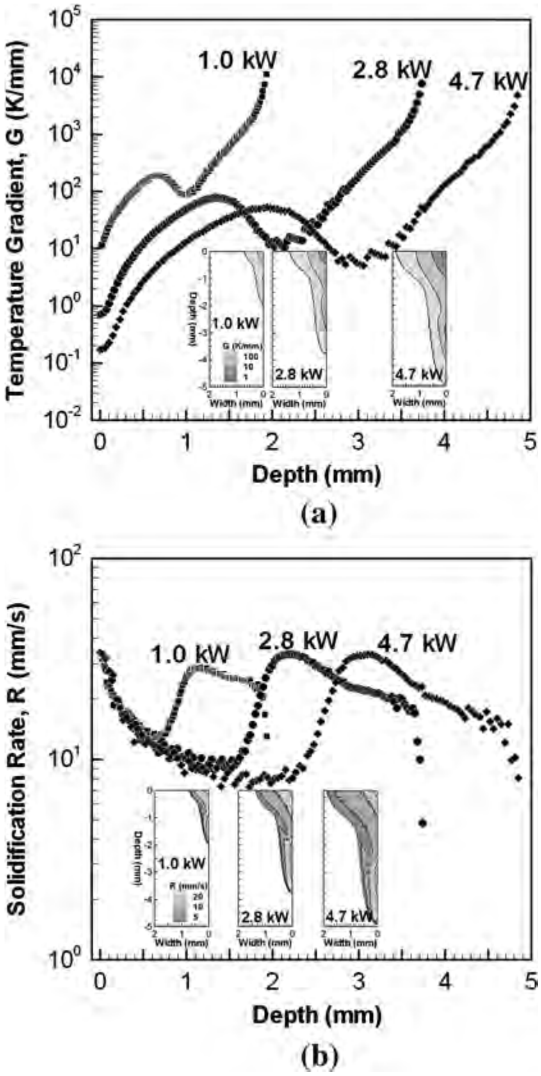

Fig. 7—The solidification parameters, (*a*) temperature gradient (*G*) and (*b*) solidification rate (*R*), are plotted as a function of depth along the central *x*–*z* plane and in 2D contour plots for various powers.

power increases, significant parts of the weld are cooling at rates less than 1000 K s^{-1}. At the highest power, a large section of the top of the weld is cooling at less than 100 K s^{-1}. The 2D G/R plots also show the effects of power on the distribution of the solidification structure morphology. The G/R contour of 13 K s mm^{-2} is chosen because it is close to the transition value from cellular to columnar dendritic morphologies, so at values less than 13 K s mm^{-2}, the morphology is likely to be dendritic. As power increases, the amount of the weld enclosed by the transition value contour increases, which means the area of the fusion zone containing dendritic structures should increase. Another observation of the same contour shows that it is not continuous along the depth for the 1 kW weld, indicating that transitions from dendrites to cells to dendrites may be observable at the center of the fusion zone.

The calculated solidification rates shown in Figure 8(a) are greater than 10 mm s^{-1} in most cases indicating that

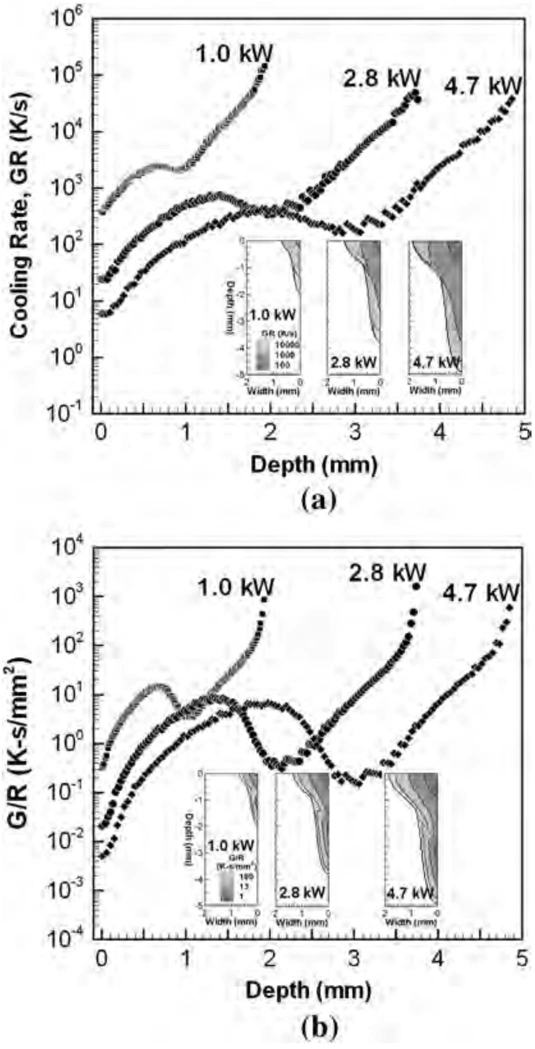

Fig. 8—The combined forms of solidification rate and temperature gradient, (*a*) cooling rate (*GR*) and (*b*) morphology parameter (*G*/*R*), are plotted as a function of depth along the central *x*–*z* plane and in 2D contour plots for various powers.

rapid solidification may play an important role in the fusion zones of these welds.[38] A calculation considering a Ni-30 wt pct Cr binary system shows that the undercooling is within the experimental range consistent with equilibrium solidification. If the thermal and kinetic undercooling are neglected, the total undercooling, ΔT, can be determined by[39]

$$\Delta T = \Delta T_C + \Delta T_R = \frac{DG}{R} - \frac{m_L Rr(1-k)C_0}{D} + \frac{2\phi}{r}, \quad [5]$$

where ΔT_C is the constitutional undercooling, ΔT_R is the undercooling due to curvature, D is the diffusion coefficient for chromium in molten nickel,[40] G/R is the morphology parameter, m_L is the slope of the liquidus line in the Ni-Cr binary phase diagram, R is the solidification rate, r is the radius of curvature of the growing cell or dendrite, k is the distribution coefficient in the Ni-Cr system,[41] C_0 is the composition of the Ni-Cr alloy, and ϕ is the Gibbs–Thomson coefficient. The G/R value is taken from Figure 8(b) for values at high

Table III. The Values Necessary for the Undercooling Calculation are Given

D Ref. [40]	G/R	m_L Ref. [41]	R	r Ref. [38]	k Ref. [41]	C_0	φ Ref. [38]
5×10^{-9} (m^2 s^{-1})	10^6 (K s m^{-2})	−2 (K/wt pct Cr)	0.034 (m s^{-1})	5×10^{-8} (m)	0.55	30 (wt pct Cr)	10^{-7} (K m)

solidification rates. The value for the radius of curvature and Gibbs–Thomson coefficient are typical values from Kurz and Fisher.[38] For the values given in Table III, the undercooling is 13 K. Kraus[42] measured undercoolings as high as 30 K in stainless steel weld pools, where equilibrium solidification was observed. Due to the low calculated undercooling, the effects of rapid solidification were not included in the model.

C. *Scale of the Solidification Structures*

The size and scale of cells and dendrites are known to vary as a function of cooling rate.[15] The cooling rate varied significantly over the range of laser powers investigated. The measured cell and secondary dendrite arm spacings were correlated to the calculated cooling rates (GR) at various positions in the weld cross section. Figure 9 shows the effect of the calculated cooling rate on experimental cell spacing and secondary dendrite arm spacing. The n value, which is defined as

$$\log(\text{spacing}) = n \log(GR) + \log(b) \qquad [6]$$

is provided for each structure. The relation in Eq. [6] is well established in the study of secondary arm spacings and is based on the solidification time being inversely proportional to the cooling rate.[15] A more detailed description by Kurz and Fisher,[38] which uses a similar relation, assumes competing growth between two cylinders (*i.e.*, secondary dendrite arms).

In Figure 9, the cell spacing ranges from 3.9 μm at 8000 K s^{-1} to 1.7 μm at 90,000 K s^{-1}. The secondary dendrite arm spacing varies from 4.0 μm at 200 K s^{-1} to 1.4 μm at 7000 K s^{-1}. These data compare well to similar data for 201 stainless steel.[43] Additionally, the measured cell and secondary arm spacings from the literature for Alloy 690 showed cell and dendrite arm spacings of about 4 μm for comparable heat inputs.[8,10] The data points shown in Figure 9 represent a combination of 87 and 58 linear intercept measurements for cells and dendrite arms, respectively. The standard deviations for the measurements vary from 0.06 to 1.01 μm. Median standard deviations are 0.35 and 0.28 μm for cell and secondary dendrite arm spacings, respectively, and are comparable to the standard deviations of similarly sized stainless steel spacing measurements.[35]

The following relations give the size of the solidification structures in microns as a function of cooling rate (K s^{-1}) in the general form $\lambda = b(GR)^n$, based on the fitted lines in Figure 9

$$\lambda_{\mathrm{CS}} = 60.6(GR)^{-0.31}, \qquad [7]$$

$$\lambda_{\mathrm{DAS}} = 17.9(GR)^{-0.29}, \qquad [8]$$

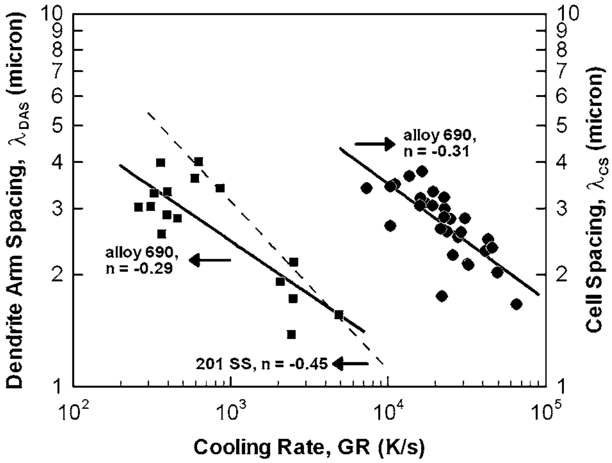

Fig. 9—The measured cell spacing (circles) and secondary dendrite arm spacing (squares) are shown as a function of calculated cooling rate. The 201 stainless steel[43] system is shown for comparison.

where λ_{CS} is the cell spacing and λ_{DAS} is the secondary dendrite arm spacing. These cooling rate relations are much more precise than any heat input relations since, as demonstrated previously, the cooling rate can vary significantly as a function of position in a weld pool for any given heat input. These data are not limited to just laser welding and can be applied to various processes that require or incorporate solidification processing, including casting, conventional arc welding, and other high energy beam processes.

D. *Morphology of the Solidification Structures*

The parameter G/R, which determines the morphology of the solidification structure, can be calculated and correlated to the experimental microstructure in the fusion zone. In the fusion zone, the solidification structure consisted mostly of cells and columnar dendrites since significant amounts of equiaxed dendrites and planar solidification were not observed. The area fractions of cells and columnar dendrites were measured by optical microscopy. The values of G/R were correlated with the observed solidification structure in the fusion zone. The computed G/R values were 13 K s mm^{-2} or lower in all areas where columnar dendrites were observed. Similarly, the computed G/R values were 21 K s mm^{-2} or higher where cellular structure was observed. The transition between columnar dendrites and cellular structure occurred between 13 and 21 K s mm^{-2}. By using the value of G/R that corresponds to the cells and columnar dendrites, the area fractions of the two solidification structures in the transverse cross-section of the weld can be calculated.

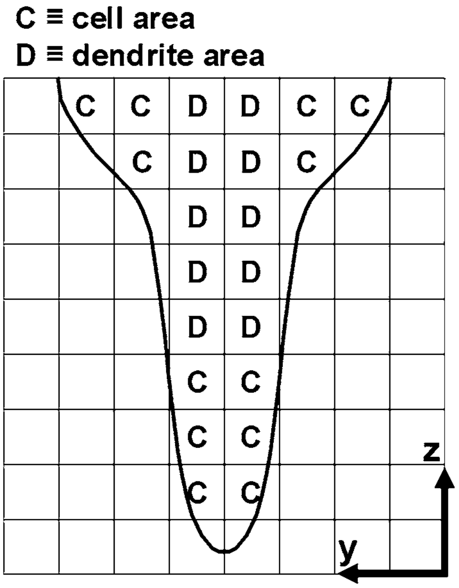

Fig. 10—A schematic of the calculated fusion zone shows how the area fractions of cells and dendrites are calculated. If the calculated *G*/*R* value of a given control volume is greater than the critical value, then the area of the *y*–*z* face is assigned to the cell area fraction. Otherwise, the area is added to the dendrite area fraction.

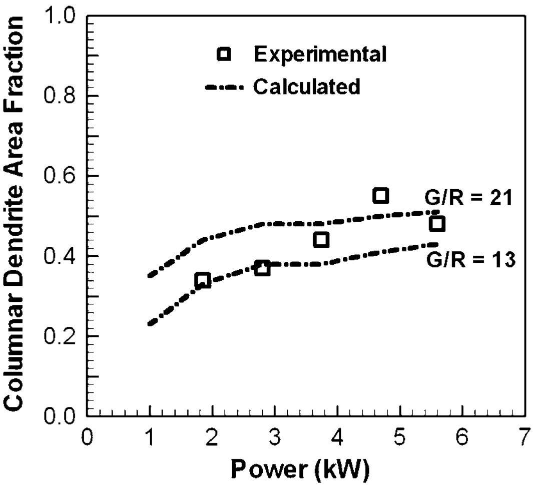

Fig. 11—A comparison between the calculated and experimental area fractions of columnar dendrites shows good agreement. The different *G*/*R* values represent the lowest value at which cells were observed and greatest value where columnar dendrites were observed.

A transverse cross section of the fusion zone is shown in Figure 10. If the *G*/*R* value is less than the critical value for the transition from dendrites to cells, then the *y*–*z* face of the control volume is assigned to the dendrite area, or *D* in the schematic. In this way the total area of cells and dendrites is determined. The area fractions are the areas of cells or dendrites divided by the total area. Figure 11 shows the experimental and calculated fusion zone area fractions of columnar dendrites with two different critical *G*/*R* values. Only the fraction of cells and columnar dendrites are considered, since significant amounts of equiaxed dendrites and planar solidification were not observed. For the conditions examined in this study, the area fraction of columnar dendrites barely exceeds 0.5 for a laser power of 4.7 kW. The model calculations and experimental measurements agree.

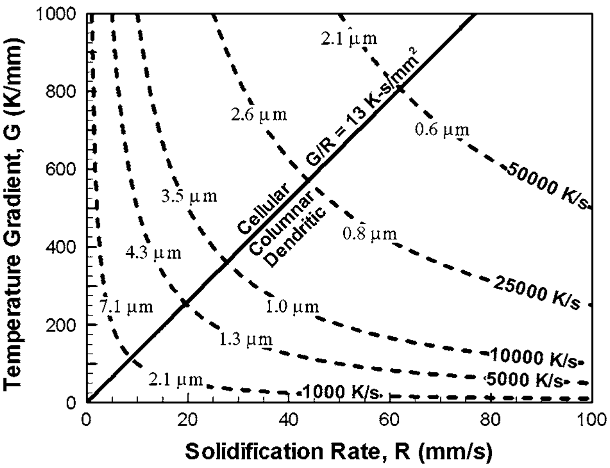

Fig. 12—The solidification map shows the transition from cellular to columnar dendritic morphology with various cooling rates. Along each cooling rate is the cell spacing and secondary dendrite arm spacing, which are determined from Eqs. [5] and [6]. With this map the scale and morphology of the solidification structures can be predicted quantitatively.

The size and morphology of the solidification structures within the experimental welds have been correlated to calculate solidification parameters. A solidification map for Alloy 690 can now be constructed to predict the solidification morphology and the scale of the structure. This map is shown in Figure 12. The solid straight line delineates the cellular and columnar dendritic regions of the map. Cooling rates are represented by the dashed curved lines and show the cell spacings and secondary dendrite arm spacings calculated from Eqs. [5] and [6], respectively. This map has a number of practical applications. For any given welding parameters, the minimum size of secondary arm spacings can be determined immediately based on the welding speed since the solidification rate can not exceed the welding speed. For example, if the welding speed is set to 25 mm s^{-1}, then a secondary arm spacing of 1.3 μm is possible, while a value of 1.0 μm is not. On the other hand, cell spacings greater than 2.6 μm would be expected for most of the weld, where the temperature gradient is 1000 K mm^{-1} or less. Spacings less than 2.6 μm would be confined to high temperature gradient and cooling rate regions, such as the root of the weld and near the fusion line. In addition, the wide range of *G* and *R* values makes the map applicable to any process, where solidification processing of Alloy 690 is necessary.

IV. SUMMARY AND CONCLUSIONS

The solidification parameters of Inconel® Alloy 690 during keyhole mode laser welding have been calculated using a mathematical model, and correlated with experimentally determined solidification structure. The large variation in the solidification parameter values in the fusion zone of the laser welds allowed for the construction of a solidification map that describes the scale and morphology of the solidification structures for given values of G and R.

1. A large spatial variation of the calculated solidification parameters was observed. Along the central longitudinal plane, the G/R value could vary up to five orders of magnitude. In both the transverse cross section and the central longitudinal plane, increases in laser power lead to a significant increase in the spatial variation of the solidification parameters.
2. The measured cell and secondary dendrite arm spacings were correlated to the calculated solidification parameters and expressed as functions of cooling rate in the form $\lambda = b(GR)^n$. These expressions can be applied for a variety of welding processes and conditions. G/R values of 13 and 21 K s mm^{-2}, which are associated with the transition from cellular to columnar dendritic solidification structures, were used to calculate the dendrite area fractions, which agreed with the measured values.
3. A map of solidification scales and morphologies for Alloy 690 was constructed based on the data presented in this work. The cell and dendrite arm sizes and the cellular and dendritic morphology regions are plotted as a function of the temperature gradient, G, and the solidification rate, R. The utility of the map was highlighted by describing how minimum secondary dendrite arm spacings can be selected based on the welding speed. Due to the large range of G and R values captured in these keyhole mode laser welds, the map has very wide applicability to a range of materials processes from casting to arc and laser welding.

ACKNOWLEDGMENTS

The authors would like to thank Mr. Jay Tressler and Mr. Ed Good for their assistance during the welding experiments and metallography. This research was performed using funding received from the DOE Office of Nuclear Energy's Nuclear Energy University Programs under Grant Number 120327.

REFERENCES

1. Q.Z. Zuo, F. Liu, L. Wang, and C. Chen: *Metall. Mater. Trans. A*, 2013, vol. 44A, pp. 3014–27.
2. F. Azarmi and C.P. Leither: *Metall. Mater. Trans. A*, 2012, vol. 43A, pp. 4703–10.
3. M. Xie, R. Helmink, and S. Tin: *Metall. Mater. Trans. A*, 2012, vol. 43A, pp. 1259–67.
4. C.L. Brundidge, D. Vandrasek, B. Wang, and T.M. Pollock: *Metall. Mater. Trans. A*, 2012, vol. 43A, pp. 965–76.
5. T.D. Anderson, J.N. DuPont, and T. DebRoy: *Acta Mater.*, 2010, vol. 58, pp. 1441–54.
6. T. Allen, J. Busby, M. Meyer, and D. Petti: *Mater. Today*, 2010, vol. 13, pp. 14–23.
7. S. Fukumoto and W. Kurz: *ISIJ Int.*, 1999, vol. 39, pp. 1270–79.
8. G.J. Abraham, R. Bhambroo, V. Kain, G.K. Dey, and V.S. Raja: *J. Mater. Eng. Perform.*, 2013, vol. 22, pp. 427–32.
9. S.-L. Jeng and Y.-H. Chang: *Mater. Sci. Eng. A*, 2012, vol. 555, pp. 1–12.
10. H.T. Lee and J.L. Wu: *Corros. Sci.*, 2009, vol. 51, pp. 439–45.
11. H.T. Lee and T.Y. Kou: *Sci. Technol. Weld. Join.*, 1999, vol. 4, pp. 246–56.
12. T.-Y. Kou, H.T. Lee, and C.C. Tu: *Sci. Technol. Weld. Join.*, 2003, vol. 8, pp. 39–48.
13. T.-Y. Kou and H.-T. Lee: *Mater. Sci. Eng. A*, 2002, vol. 338, pp. 202–12.
14. A. Raghavan, H. Wei, T.A. Palmer, and T. DebRoy: *J. Laser Appl.*, 2013, vol. 25, art. no. 052006.
15. S. Kou: *Welding Metallurgy*, 2nd ed., Wiley, Hoboken, NJ, 2003.
16. W. Zhang, G.G. Roy, J.W. Elmer, and T. DebRoy: *J. Appl. Phys.*, 2003, vol. 93, pp. 3022–33.
17. R. Rai, G.G. Roy, and T. DebRoy: *J. Appl. Phys.*, 2007, vol. 101, art. no. 054909.
18. R. Rai, J.W. Elmer, T.A. Palmer, and T. DebRoy: *J. Phys. D*, 2007, vol. 40, pp. 5753–66.
19. R. Rai, S.M. Kelly, R.P. Martukanitz, and T. DebRoy: *Metall. Mater. Trans. A*, 2008, vol. 39A, pp. 98–112.
20. T.D. Anderson, J.N. DuPont, and T. DebRoy: *Metall. Mater. Trans. A*, 2010, vol. 41A, pp. 181–93.
21. J.D. Hunt: *Mater. Sci. Eng.*, 1984, vol. 65, pp. 75–83.
22. M. Gaumann, R. Trivedi, and W. Kurz: *Mater. Sci. Eng. A*, 1997, vols. 226–228, pp. 763–69.
23. M. Gaumann, C. Bezencon, P. Canalis, and W. Kurz: *Acta Mater.*, 2001, vol. 49, pp. 1051–62.
24. W. Tan, N.S. Bailey, and Y.C. Shin: *J. Manuf. Sci. Eng.*, 2012, vol. 134, p. 041010.
25. W. Zhang, C.-H. Kim, and T. DebRoy: *J. Appl. Phys.*, 2004, vol. 95, pp. 5210–19.
26. H. Zhao and T. DebRoy: *J. Appl. Phys.*, 2003, vol. 93, pp. 10089–96.
27. B. Ribic, R. Rai, and T. DebRoy: *Sci. Technol. Weld. Join.*, 2008, vol. 13, pp. 683–93.
28. B. Ribic, S. Tsukamoto, R. Rai, and T. DebRoy: *J. Phys. D*, 2011, vol. 44, art. no. 485203.
29. A. Kaplan: *J. Phys. D*, 1994, vol. 27, pp. 1805–14.
30. S. Krishnan and P.C. Nordine: *J. Appl. Phys.*, 1996, vol. 80, pp. 1735–42.
31. W.F. Gale and T.C. Totemeier: *Smithells Metals Reference Book*, 8th ed., Elsevier Butterworth-Heinemann, Burlington, VT, 2004.
32. Special Metals Corporation: *INCONEL® Alloy 690 Data Sheet, Publication Number SMC-079*, 2009, http://www.specialmetals.com/documents/Inconel%20alloy%20690.pdf, Accessed 9 July 2013.
33. L.B. Pakratz: *Thermodynamic Properties of Elements and Oxides*, U.S. Dept. of the Interior, Bureau of Mines, District of Columbia, 1982.
34. Y.V. Glagoleva, N.B. Pushkareva, Y.E. Lapshova, O.V. Sadyreva, V.R. Polev, V.I. Gorbatov, S.G. Taluts, and I.G. Korshunov: *Phys. Met. Metallogr.*, 2006, vol. 102, pp. 48–54.
35. M.A. Valiente-Bermejo, L. Karlsson, and T. DebRoy: *14th Nordic Laser Materials Processing Conference*, 2013, pp. 3–14.
36. W. Liu and J.N. Dupont: *Acta Mater.*, 2004, vol. 52, pp. 4833–47.
37. J.M. Vitek: *Acta Mater.*, 2005, vol. 53, pp. 53–67.
38. W. Kurz and D.J. Fisher: *Fundamentals of Solidification*, 3rd ed., Trans Tech Publications, Brookfield, VT, 1989.
39. S.A. David and J.M. Vitek: *Int. Mater. Rev.*, 1989, vol. 34, pp. 213–45.
40. S. Nikolic, A. Golubovic, V. Radojevic, A. Valcic, and B. Jordovic: *J. Metall.*, 2004, vol. 10, pp. 289–93.
41. P. Nash: *Alloy Phase Diagrams*, ASM International, Materials Park, OH, 1991, vol. 3.
42. H.G. Kraus: *Weld. J.*, 1987, vol. 66, pp. S353–59.
43. A. Paul and T. DebRoy: *Metall. Trans. B*, 1988, vol. 19B, pp. 851–58.

Appendix B:

Real Time Monitoring of Laser Beam Welding Keyhole Depth by Laser Interferometry

Real time monitoring of laser beam welding keyhole depth by laser interferometry

J. J. Blecher*[1], C. M. Galbraith[2], C. Van Vlack[3], T. A. Palmer[4], J. M. Fraser[2], P. J. L. Webster[3] and T. DebRoy[1]

The utility of a new laser interferometric technique, inline coherent imaging, for real time keyhole depth measurement during laser welding is demonstrated on five important engineering alloys. The keyhole depth was measured at 200 kHz with a spatial resolution of 22 μm using a probe beam, which enters the keyhole coaxially with the process beam. Keyhole fluctuations limited average weld depth determination to a resolution on the order of 100 μm. Real time keyhole depth data are compared with the weld depths measured from the corresponding metallographic cross-sections. With the exception of an aluminium alloy, the technique accurately measured the average weld depth with differences of less than 5%. The keyhole depth growth rates at the start of welding are measured and compare well with order of magnitude calculations. The method described here is recommended for the real time measurement and control of keyhole depth in at least five different alloys.

Keywords: Laser keyhole, Welding, Weld monitoring, Laser interferometry, Keyhole depth, Keyhole growth rate

Introduction

The ability of lasers to produce deep penetration welds in thick plates of 20 mm and more depends on the formation of a stable keyhole.[1–5] At present there is no widely accepted technique for the real time measurement of keyhole depth during laser welding. While X-ray videography views the keyhole directly in plates thin enough to allow X-ray transmission,[6] the technique is not generally used outside a laboratory environment. Mathematical modelling of heat transfer can predict steady state keyhole depths for various materials[7,8] but requires access to a rigorously validated numerical model. Popular methods for monitoring depth and porosity generation rely on indirect observation of the keyhole behaviour, such as capturing the optical[9,10] and acoustic[11,12] signals produced by vapour escaping the keyhole.[13,14] Other techniques include measuring plasma charge,[15] viewing the weld with cameras,[10,16,17] or utilising a combination of sensors.[10,17] Owing to their nature, however, indirect measurements are subject to numerous difficulties, requiring additional calibration each time a process or material parameter changes. A need exists for a direct measurement of keyhole depth with a high degree of process flexibility.

Recently developed inline coherent imaging (ICI) directly measures the keyhole depth in real time.[18–20] The high quality spatial and temporal resolution inherent in this technique can capture keyhole depth changes smaller than 10 μm over time periods shorter than 10 μs.[20] ICI is an interferometric technique that directs a probe beam coaxially with the process beam into the keyhole. As long as a keyhole is present, ICI can directly measure the keyhole depth in any partial penetration weld regardless of other process parameters. For example, ICI has been used to measure the drill hole depth in ferrous alloys during laser machining,[18,19] and its application in laser welding is just beginning.[20]

In this paper, the utility of ICI to provide real time measurements of keyhole depth is demonstrated in DH36 steel, 304 stainless steel, Inconel® Alloy 690, Ti–6Al–4V, and 2219 aluminium alloys. A wide range of industries, including construction, energy, aerospace, and automotive, utilise and join the alloys used in this study or compositionally similar alloys. Keyhole depth measurements are performed for each alloy and compared with metallographic cross-sections. The initiation and growth of the keyhole at the beginning of welding for the five alloys are also studied with ICI. These data allow direct measurement of the keyhole growth rates in the first 5 ms of welding with unprecedented temporal resolutions on the order of 5 μs. The keyhole growth rates are estimated using energy balance between the laser energy and the energy necessary to evaporate the liquid metal. The theoretical growth rates show order of magnitude agreement with the measured rates, indicating the measured growth rates are realistic.

---

[1] Department of Materials Science and Engineering, The Pennsylvania State University, University Park, PA 16802, USA
[2] Department of Physics, Engineering Physics and Astronomy, Queen's University at Kingston, Kingston, Ontario, K7L 3N6, Canada
[3] Laser Depth Dynamics Inc., Kingston, Ontario, K7L 2L1, Canada
[4] Applied Research Laboratory, The Pennsylvania State University, University Park, PA 16802, USA

*Corresponding author, email jjb5120@psu.edu

© 2014 Institute of Materials, Minerals and Mining
Published by Maney on behalf of the Institute
Received 18 April 2014; accepted 25 May 2014
DOI 10.1179/1362171814Y.0000000225

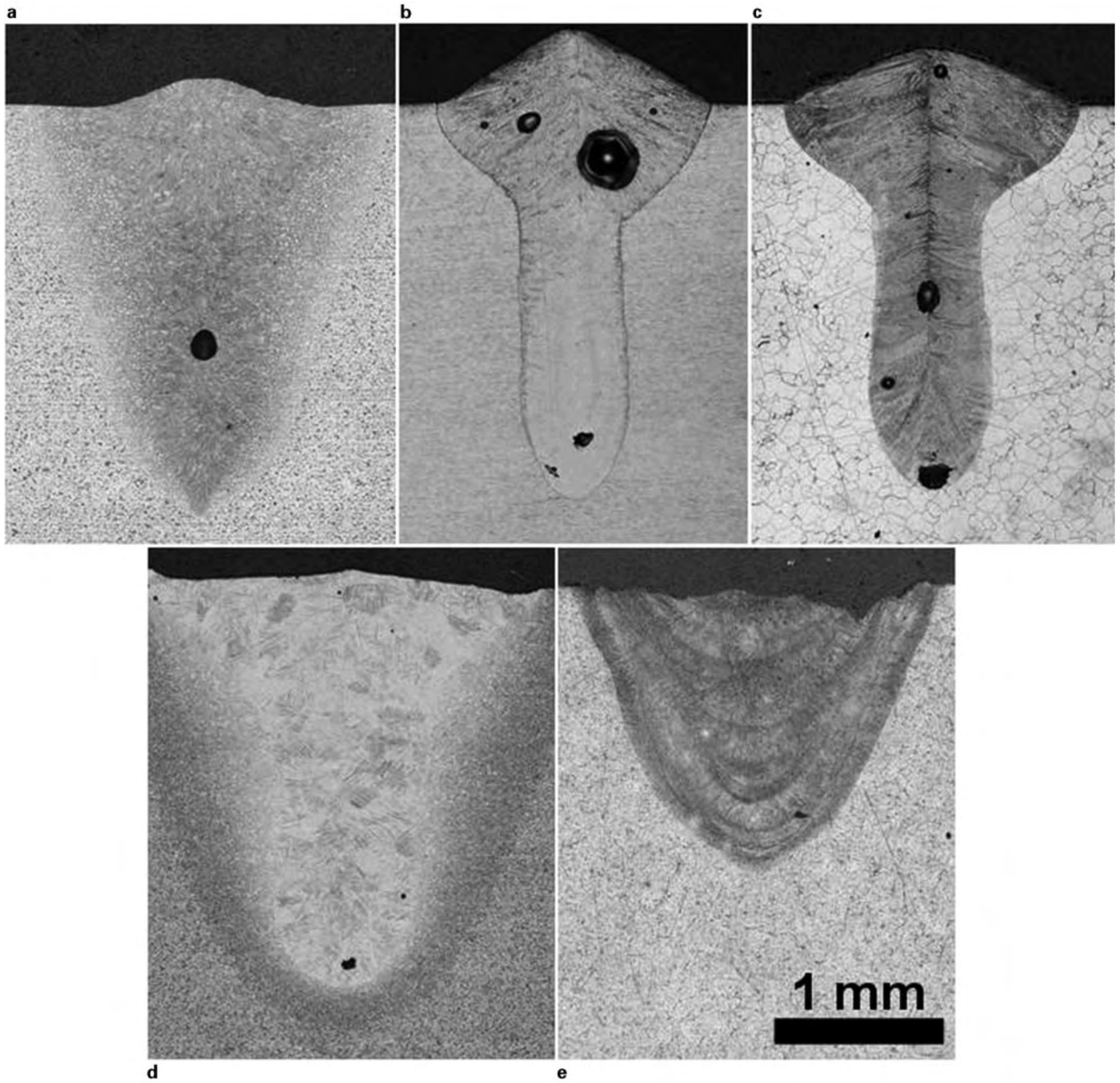

1 **Metallographic cross-sections of *a* DH36 steel, *b* 304 stainless steel, *c* alloy 690, *d* Ti–6Al–4V, and *e* 2219 aluminium are shown: each weld was created with laser power of 1·1 kW and welding speed of 25 mm s^{-1}**

Experiments

An IPG Photonics YLS-1000-IC laser with a 100 μm core process fibre coupled to a Laser Mechanisms AccuFiber head with a 60 mm focal length collimator and a 150 mm focal length lens were used to produce bead on plate welds on DH36 steel, 304 stainless steel, Inconel® Alloy 690, Ti–6Al–4V, and 2219 aluminium alloys. The nominal compositions are given in Table 1. A laser power and welding speed of 1·1 kW and 25 mm s^{-1} respectively, was used with coaxial argon shielding gas for the welding experiments. The focus of the process beam was located at the surface of the material for all experiments. During welding, ICI data were collected in real time. After welding, six transverse sections were prepared from each weld using standard metallographic techniques. A Nikon DS-Fi2 camera attached to a Nikon Epiphot microscope and Nikon NIS Elements software captured micrographs of the welds.

Table 1 Compositions of various alloys that were welded in this study are given

Alloy	Fe	C	Mn	Si	Cr	Ni	Ti	Al	V	Cu
DH36	Bal.	0·18	1·25	0·30	0·25	0·40	…	…	0·10	0·35
304	Bal.	0·08	1·50	2·00	20·00	10·00	…	…	…	…
Alloy 690	10·00	0·03	0·19	0·08	30·00	Bal.	…	…	…	…
Ti–6Al–4V	0·30	0·10	…	…	…	…	Bal.	6·00	4·00	…
AA 2219	…	…	0·30	…	…	…	0·06	Bal.	0·10	6·30

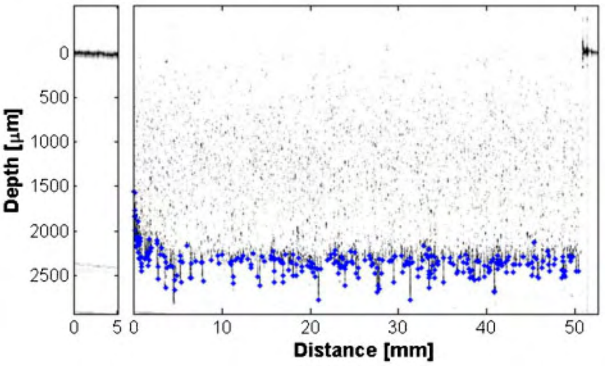

2 ICI image of weld in Alloy 690 is presented: left panel shows height of plate surface determined from pre-scan measurement: large pane shows raw ICI data (dark spots) and keyhole depth (blue dots)

Detailed descriptions of ICI are available in the literature,[18–20] so only a brief discussion of the important features is given here. ICI utilises a Michelson interferometer construction with a reference and probe beam, using a superluminescent diode with a wavelength of 843 nm and FWHM of 20 nm as the light source. The probe beam is directed through the same optics as the high power process beam and into the keyhole, where the probe beam reflects off surfaces along its path. The reference beam is set along a path of known distance with appropriate dispersion matching optics. The two beams are recombined and directed to a spectrometer, which collects the interference pattern (measured integration time: 1·5 μs). The positions of the scattering surfaces along the laser axis are determined with a resolution of 22 μm from the spectral interference pattern. After sampling of the interference pattern at 200 kHz over the length of the weld, the keyhole depth as a function of position is determined.

Results and discussion

Autogenous bead on plate laser welds were made on five alloys while simultaneous ICI measurements were conducted. The metallographic cross-sections for each weld are shown in Fig. 1. Keyhole mode welding was achieved for each alloy, and with the exception of the high thermal conductivity aluminium alloy, the typical wineglass shape is apparent. The weld depths in DH36 steel, 304 stainless steel, Alloy 690, and Ti–6Al–4V appear to be very similar. However, the width of the titanium weld is greater than the others.

An example of the real time ICI measured keyhole depth in Alloy 690 along the length of the weld is shown in Fig. 2. The small panel on the left of the figure shows a small portion of the pre-scan, which gives the position of the surface, shown as the black line at the top, and is necessary to acquire absolute keyhole depth measurements with the greatest possible accuracy. The faint signal around 2400 μm depth in the pre-scan is due to an imaging artifact and does not represent a real scattering surface. The large image displays both the raw ICI data and the depth of the keyhole. Dark spots in the image indicate the position of a reflective interface along the beam path. Typically, the strongest reflections are from the molten metal at the bottom of the keyhole, however due to the dynamic nature of the keyhole shape, scatter from the keyhole front wall and side wall can be observed at intermediate depths. Blue points represent the ICI measured keyhole depth as determined by a depth tracking algorithm. At distance zero in Fig. 2, the laser weld starts, and the keyhole depth increases to 2·3 mm once 4 mm of weld length has been fabricated. Over the course of the weld, the ICI measured keyhole depth fluctuates between extremes of 2·1 and 2·8 mm, which represent a maximum change of 22% in the measured depth of the weld determined from the metallographic cross-section.

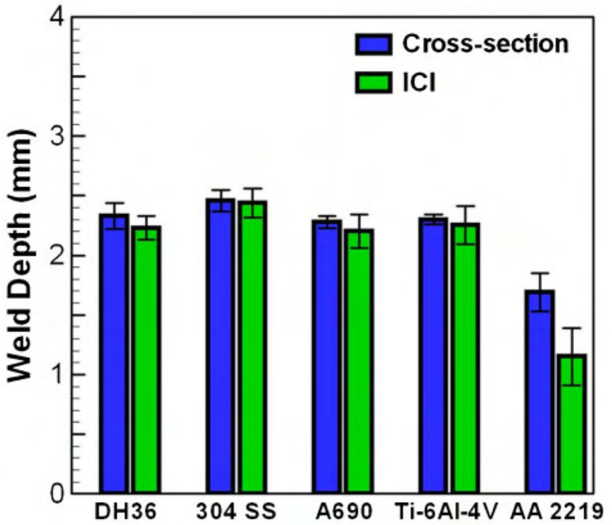

3 Comparison of ICI depth measurements and depths from metallographic cross-sections is shown: ICI weld depth was averaged from depth tracking algorithm across entire weld region; black bars represent standard deviation of depths measured by each technique; two sets of measurements agree except in case of AA 2219

An important issue in any new technique is the accuracy of the measurements. Figure 3 shows a comparison of the average ICI depth measurements and weld depths determined by transverse metallographic cross-sections. The metallographic depths shown in this figure are an average of six measurements taken at different

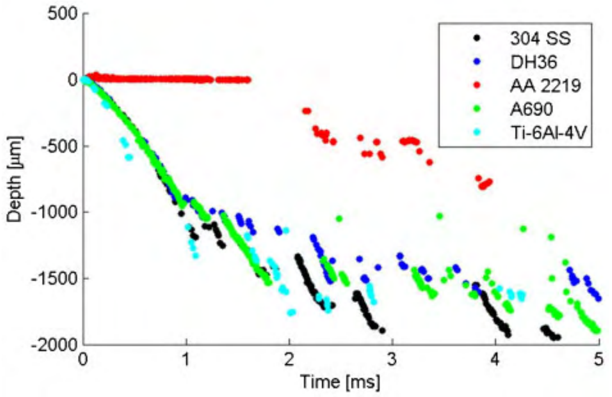

4 ICI measured keyhole depths during first 5 ms, or 0·125 mm, of welding show how fast keyhole initiates and grows for each alloy: aluminium 2219 is slowest to initiate and grow keyhole, while Ti–6Al–4V is fastest

Table 2 Material properties used in heat balance and measured and calculated keyhole growth rates are given

	DH36	304 S.S.	A690	Ti–6Al–4V	AA2219
Absorptivity η	0·33	0·32	0·29	0·31	0·19
Density ρ/kg m^{-3}	7050	7070	7480	3970	2560
Heat of Vaporisation ΔH_v/kJ kg^{-1}	6260	6330	6450	8810	10 720
Measured growth rate u/m s^{-1}	0·91	1·09	0·98	1·11	0·56
Calculated growth rate u/m s^{-1}	0·97	0·93	0·78	1·15	0·90

positions in the weld with the black bars representing one standard deviation, which is estimated from the same six measurements. For the ICI data set, the black bars are given by the standard deviation of measurements taken over the length of the weld and are representative of real variation in the keyhole depth. The precision of an instantaneous ICI keyhole depth measurement is limited by the axial resolution of the system, which at 22 μm, is an order of magnitude smaller than the observed keyhole depth fluctuations. In every case the measured keyhole depth is slightly smaller than the measured weld depth, which agrees with modelling results showing that the weld depth is always slightly greater than the keyhole depth.[7,8] With the exception of the 2219 aluminium alloy, very good agreement is observed between the ICI and the metallographic measurements across a wide alloy composition range, indicating that inline coherent imaging can be used as a real time process monitoring tool for capturing keyhole depths. To give a consistent comparison, the same imaging parameters were used for all five alloys. In the case of aluminium, the high melt reflectivity resulted in intermittent saturation of the ICI system. When combined with the large, rapid fluctuations in keyhole depth characteristic of this alloy, the averaged ICI depth measurements were biased toward artificially shallow values. Optimisation of imaging parameters and algorithmic interpretation of the ICI data is expected to improve the accuracy in aluminium weld depths.

To demonstrate the spatial and temporal resolution of the technique, the initial formation and growth of keyholes are shown in Fig. 4. At time zero, the laser beam turns on, and processing begins. In aluminium, there is a 1·6 ms delay between the beam turning on and a rapid increase in depth at a rate of 0·56 m s^{-1}. The observed delay is consistent with aluminium's relatively high reflectivity and thermal conductivity. In the other alloys during the initial 1 ms of welding, the keyholes grew at rates between 0·91 and 1·11 m s^{-1}. Other studies have found initial growth rates in 304 stainless steel[21] and Ti–6Al–4V[22] for laser powers of 2·3 and 8·7 kW to be 1·50 and 0·66 m s^{-1} respectively, when measured with X-ray transmission videography, which has temporal resolutions[21,22] of 200 μs, compared to the 5 μs achieved here. The difference in temporal resolution is important for two reasons in this case. First, a more accurate determination of the onset of keyhole formation can be made for the aluminium alloy. Second, the growth rates in the other four alloys can be differentiated. With X-ray transmission videography, the growth rates in steel, stainless steel, Alloy 690, and Ti–6Al–4V would have appeared the same. Unfortunately, the accuracy of the X-ray and ICI keyhole depth measurement techniques cannot be compared since this information was not given in the studies of X-ray transmission videography.

Order of magnitude keyhole growth rates can be estimated by equating the laser energy absorbed by the workpiece and the energy necessary to evaporate the liquid metal at any point on the vaporising surface. This theoretical growth rate is

$$u = \frac{\eta I_L}{\rho \Delta H_v} \qquad (1)$$

where η is the absorptivity of the liquid metal, I_L is the peak intensity of the laser, approximately 130 kW mm^{-2}, ρ is the density of the liquid metal, and ΔH_v is the latent heat of vaporisation. The necessary material properties and the measured and calculated growth rates are shown in Table 2. The order of magnitude estimates agree with the ICI measured keyhole growth rates in DH36 steel, 304 stainless steel, Alloy 690, and Ti–6Al–4V, indicating that the scale analysis can be used to estimate the keyhole growth rates in these alloys when the relevant process parameters and material properties are known. In the case of aluminium alloy 2219, the ICI measured keyhole growth rate was lower than that estimated by scale analysis assuming no heat loss. The comparison shows considerable heat loss by conduction in the alloy.

Conclusions

The application of inline coherent imaging to keyhole depth monitoring in laser welding has been demonstrated. The findings from this work are listed below.

1. Real time keyhole depth measurements from autogenous bead on plate welds of five alloys were compared to depths from metallographic transverse cross-sections. The two sets of data show good agreement, indicating that the technique can be applied to a wide range of different alloys and maintain the ability to measure the keyhole depth in real time.
2. The initiation and growth of the keyholes was investigated with real time measurements. The observed keyhole growth rates between 0·56 and 1·11 m s^{-1} compare well to previous measurements, which used X-ray videography. The initial keyhole growth rates measured by the inline coherent imaging technique agree well with the corresponding values estimated by scale analysis.

Acknowledgements

The authors would like to thank Mr. Ed Good for his assistance with the metallography. This research was performed using funding received from the DOE Office of Nuclear Energy's Nuclear Energy University Programs under grant no. 120327, the Natural Sciences and Engineering Research Council of Canada, the Ontario Centres of Excellence, and the Canadian Foundation for Innovation.

References

1. D. Y. You, X. D. Gao and S. Katayama: 'Review of laser welding monitoring', *Sci. Technol. Weld. Join.*, 2014, **19**, 181–201.
2. N. Coniglio and M. Patry: 'Measuring laser weldability of aluminium alloys using controlled restraint weldability test', *Sci. Technol. Weld. Join.*, 2013, **18**, 573–580.
3. E. Assuncao, S. Ganguly, D. Yapp, S. Williams and A. Paradowska: 'Characterisation of residual stress state in laser welded low carbon mild steel plates produced in keyhole and conduction mode', *Sci. Technol. Weld. Join.*, 2011, **16**, 239–243.
4. J. E. Blackburn, C. M. Allen, P. A. Hilton, L. Li, M. I. Hoque and A. H. Khan: 'Modulated Nd:YAG laser welding of Ti-6Al-4V', *Sci. Technol. Weld. Join.*, 2010, **15**, 433–439.
5. Y. Kawahito, M. Mizutani and S. Katayama: 'High quality welding of stainless steel with 10 kW high power fibre laser', *Sci. Technol. Weld. Join.*, 2010, **14**, 288–294.
6. A. Matsunawa, J. D. Kim, N. Seto, M. Mizutani and S. Katayama: 'Dynamics of keyhole and molten pool in laser welding', *J. Laser Appl.*, 1998, **10**, 247–254.
7. R. Rai, G. G. Roy and T. DebRoy: 'A computationally efficient model of convective heat transfer and solidification characteristics during keyhole mode laser welding', *J. Appl. Phys.*, 2007, **101**, 054909.
8. R. Rai, J. W. Elmer, T. A. Palmer and T. DebRoy: 'Heat transfer and fluid flow during keyhole mode laser welding of tantalum, Ti-6Al-4V, 304L stainless steel and vanadium', *J. Phys. D: Appl. Phys.*, 2007, **40**, 5753–5766.
9. A. Ancona, V. Spagnolo, P. M. Lugara and M. Ferrara: 'Optical sensor for real-time monitoring of CO_2 laser welding process', *Appl. Opt.*, 2001, **40**, 6019–6025.
10. D. You, X. Gao and S. Katayama, 'Multiple-optics sensing of high-brightness disk laser welding process', *NDT&E Int.*, 2013, **60**, 32–39.
11. W. Huang and R. Kovacevic, 'Feasibility study of using acoustic signals for online monitoring of the depth of weld in the laser welding of high-strength steels', *Proc. IMechE Part B: J. Eng. Manuf.*, 2009, **223**, 343–361.
12. W. Huang and R. Kovacevic: 'A neural network and multiple regression method for the characterization of the depth of weld penetration in laser welding based on acoustic signatures', *J. Intell. Manuf.*, 2011, **22**, 131–143.
13. D. F. Farson and K. R. Kim: 'Generation of optical and acoustic emissions in laser weld plumes', *J. Appl. Phys.*, 1999, **85**, 1329–1336.
14. D. Farson, A. Ali, and Y. Sang: 'Relationship of optical and acoustic emissions to laser weld penetration', *Weld. J.*, 1998, **77**, 142s–148s.
15. L. Li, D. J. Brookfield and W. M. Steen, 'Plasma charge sensor for in-process, non-contact monitoring of the laser welding process', *Meas. Sci. Technol.*, 1996, **7**, 615–626.
16. C.-H. Kim and D.-C. Ahn, 'Coaxial monitoring of keyhole during Yb:YAG laser welding', *Opt. Laser Technol.*, 2012, **44**, 1874–1880.
17. Y. Kawahito, T. Ohnishi and S. Katayama: 'In-process monitoring and feedback control for stable production of full-penetration weld in continuous wave fibre laser welding', *J. Phys. D: Appl. Phys.*, 2009, **42**, 085501.
18. P. J. L. Webster, B. Y. C. Leung, J. X. Z. Yu, M. D. Anderson, T. P. Hoult and J. M. Fraser: 'Coaxial real-time metrology and gas assisted laser micromachining: process development, stochastic behavior and feedback control', *Proc. SPIE*, 2010, **7590**, 003.
19. P. J. L. Webster, L. G. Wright, K. D. Mortimer, B. Y. Leung, J. X. Z. Yu and J. M. Fraser: 'Automatic real-time guidance of laser machining with inline coherent imaging', *J. Laser Appl.*, 2011, **23**, 022001.
20. P. J. L. Webster, L. G. Wright, Y. Ji, C. M. Galbraith, A. W. Kinross, C. Van Vlack and J. M. Fraser: 'Fully-automatic laser welding and micro-sculpting with universal in situ inline coherent imaging, arXiv:1404·4419, 2014.
21. S. Fujinaga, H. Takenaka, T. Narikiyo, S. Katayama and A. Matsunawa: 'Direct observation of keyhole behaviour during pulse modulated high-power Nd:YAG laser irradiation', *J. Phys. D: Appl. Phys.*, 2000, **33**, 492–497.
22. O. Perret, M. Bizouard, Ph. Naudy, G. Pascal, D. Nore, Y. Horde and Y. Delaisse: 'Characterization of the keyhole formed during pulsed Nd-YAG laser interaction with a Ti-6Al-4V metallic target', *J. Appl. Phys.*, 2001, **90**, 27–30.

Appendix C:

Mitigation of Root Defect in Laser and Hybrid Laser-Arc Welding

Mitigation of Root Defect in Laser and Hybrid Laser-Arc Welding

A model is developed that predicts the range of processing conditions that produce defect-free, complete-joint-penetration welds

BY J. J. BLECHER, T. A. PALMER, AND T. DEBROY

ABSTRACT

Even though laser and hybrid laser-arc welding processes can produce single-pass, complete-joint-penetration welds in excess of 12 mm, root defects, such as root humping, have been observed at these greater plate thicknesses. The competition between the surface tension and the weight of the liquid metal in the weld pool is expected to govern root-defect formation. A series of laser and hybrid laser-gas metal arc welds has been completed in which each force is independently varied. The internal morphologies of the resulting root defects are characterized by X-ray computed tomography and found to vary significantly when welding with either the laser or hybrid laser-arc process. In order to compute the surface tension and liquid metal weight, a model based on the approximate geometry of the weld pool is developed and successfully predicts the range of processing conditions where root defects form. Process maps are then constructed for low-carbon steel and 304 stainless steel alloy systems. These maps can then be used to select welding parameters that produce defect-free complete-joint-penetration welds over a wide range of plate thicknesses.

KEYWORDS

• Laser Welding • Root Defect • Hybrid Welding • Carbon and Low-Alloy Steels

Introduction

High-power laser and hybrid laser-arc welding (Refs. 1–5) offer faster welding speeds, lower heat inputs, and deeper penetration over traditional arc welding processes in a range of different construction and fabrication industries (Ref. 6). However, these processes are also susceptible to unique defects associated with their high aspect ratio and deep penetration. Two of the most common of these defects include porosity from keyhole instability in partial-penetration welds (Refs. 7–9) and complete-joint-penetration welding root defects. The latter defect has also been called chain of pearls (Ref. 10), dropping (Ref. 11), and root humping (Ref. 12). and is characterized by the formation of weld metal spheroids at the bottom surface of a complete-joint-penetration weld. An example of root defects in a DH36 steel hybrid laser-arc weld is shown in Fig. 1A. As higher laser powers become available and deeper penetrations are obtained, these defects will become more problematic, and a deeper understanding of the mechanisms driving these defects will be necessary to take advantage of these high laser powers.

Root defects have been characterized at both high (Refs. 13–16) and low (Refs. 11, 13, 17, 18) heat inputs. Consequently, changes in laser power or welding speed resulted in the appearance or disappearance of root defects. For example, in 304 stainless steel, Zhang et al. (Ref. 14) and Kaplan and Wiklund (Ref. 16) found that root defects occur at lower welding speeds (i.e., higher heat input) during laser welding of 12- and 16-mm-thick plates, respectively. In other cases, increasing the heat input leads to acceptable welds. Havrilla et al. (Ref. 11) increased the laser power by 1 kW from 7.75 to 8.75 kW at a constant welding speed to eliminate root defects in 12-mm-thick steel. Ilar et al. (Ref. 12) employed high-speed imaging to study the formation of root defects in real time during the laser welding of 8-mm-thick 304 stainless steel plate. The high-speed videos showed the initiation of bulges immediately behind the keyhole, and these bulges would occasionally build up and solidify as root defects. Ilar et al. (Ref. 12) concluded that gravity, surface tension, and melt availability play a role in the formation of root defects.

One method for avoiding root defects is supporting the weld pool from the bottom through the use of electromagnetic forces from an oscillating magnetic field (Refs. 15, 19, 20). Bachmann et al. (Refs. 15, 20) complemented physical experiments by utilizing a 3D numerical heat transfer and fluid flow model to calculate the EM forces necessary to balance the hydrostatic pressure, which promoted root defects in 10- and 20-mm-thick steel and aluminum plates, respectively.

J. J. BLECHER (jjb5120@psu.edu) and T. DEBROY are with the Department of Materials Science and Engineering, and T. A. PALMER is with the Applied Research Laboratory, The Pennsylvania State University, University Park, Pa.

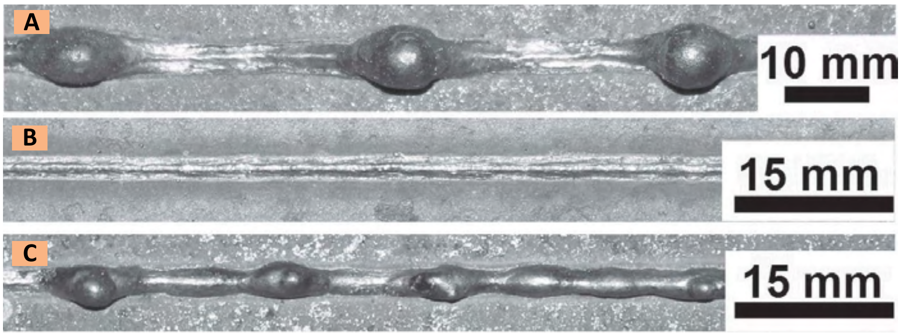

Fig. 1 — A— The typical weld root defects formed during hybrid laser-gas metal arc welding with a laser power, welding speed, and welding wire feed rate of 5 kW, 30 mm/s, and 229 mm/s, respectively; B — the roots of hybrid welds made under identical process conditions (welds 7, 8) without bottom surface oxide scale; C — with bottom oxide scale. On the plate with scale, root defects formed due to the low surface tension.

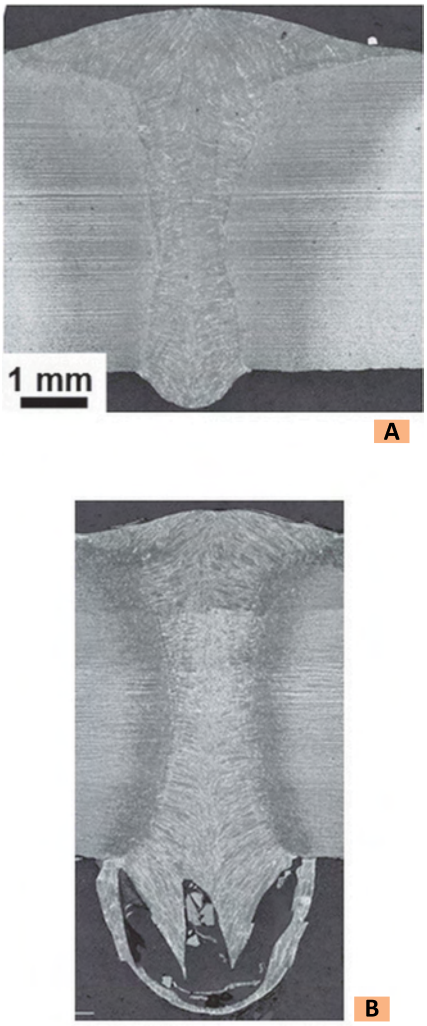

Fig. 2 — A — A comparison of the transverse hybrid weld (welds 7, 8) cross sections with identical welding conditions with the exception of bottom surface oxide scale, which was not present; B — the bottom surface oxide scale was present. The sizes of the welds are similar, suggesting that the weight of the liquid metal is similar and that the reduction in surface tension is due to the oxide scale presence, which led to the root defects.

However, the predicted EM force values were slightly less than the experimental values necessary to hold the liquid in place since only the weight of the liquid metal column above the bottom pool surface was taken into account. While EM support can be used to weld thick sections, utilizing the process in a production environment may not be practical, and the application of EM forces can change the fluid flow patterns during welding (Ref. 20). Therefore, it is necessary to develop a deeper understanding of the conditions that promote root defect formation in order to intelligently select welding parameters that suppress it.

In this paper, the formation of root defects is investigated for laser and hybrid laser-arc welding under a variety of welding conditions. For the first time, the 3D internal structure of the root defect nuggets in a structural steel plate weld was characterized by X-ray-computed tomography (CT) and was found to depend on the welding process employed. The melt volume and the surface tension of the molten DH36 steel were independently varied to determine the effect of each on root defect formation. Melt volume was varied by changing the heat input of the welds, and surface tension was altered by removing the oxide scale on the bottom surface of the plate prior to welding. Increasing melt volume or decreasing surface tension led to root defects being formed. In order to quantify each effect, a force balance considering the weight of the liquid steel and the surface tension at the weld root is developed for an idealized weld pool and used to determine the conditions for the formation of root defects. Process maps for defect-free, complete-joint-penetration laser welds, for which substantial experimental results have been reported, and selected hybrid laser-arc welds were developed for low-carbon steel and 304 stainless steel.

Experimental Methods

Bead-on-plate laser and hybrid laser-arc welds were performed on 4.8- and 9.8-mm-thick DH36 steel plate. An IPG Photonics® YLR-12000-L ytterbium fiber laser with a Precitec® YW50 welding head was used for laser

Table 1— Welding Conditions for LBW and HLAW Welds

Weld Number	Oxide Removed	Welding Process	Plate Thickness (mm)	Root Defects	Weld Speed (mm/s)	WFS (mm/s)
1	no	LBW	4.8	no	30	—
2	no	LBW	4.8	no	40	—
3	no	LBW	9.5	yes	15	—
4	no	HLAW	4.8	yes	30	127
5	no	HLAW	4.8	yes	30	152
6	no	HLAW	4.8	yes	30	229
7	yes	HLAW	4.8	no	40	127
8	no	HLAW	4.8	yes	40	127

Note: Oxide removed refers to the bottom surface oxide scale being removed.

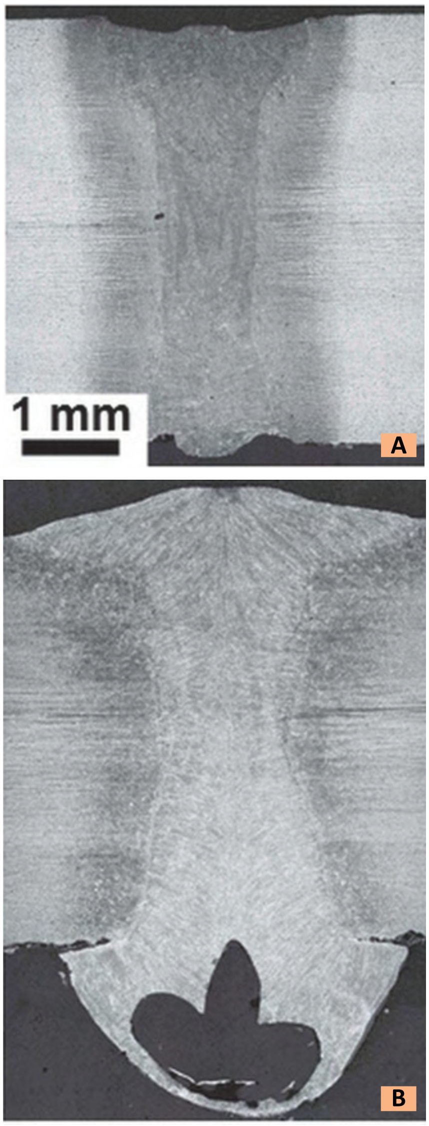

Fig. 3 — The transverse weld cross sections for: A — A laser weld (weld 1); B — a hybrid weld (weld 4) are shown. The laser conditions are the same, but the hybrid weld has increased heat input, larger amount of melted volume, and greater weight that must be supported by the surface tension force.

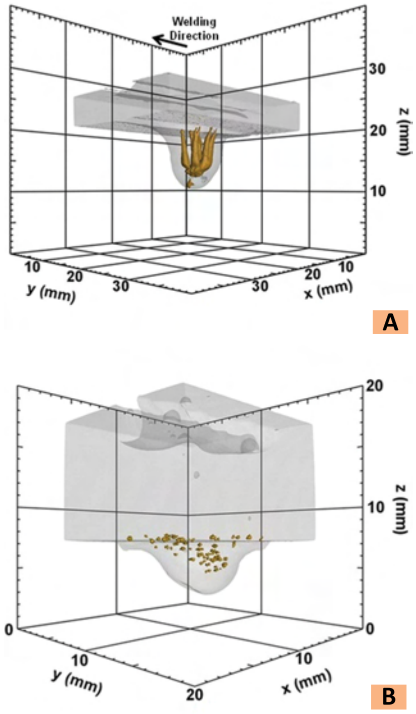

Fig. 4 — The internal structure of root defects in: A — Hybrid laser-gas metal arc weld in 4.8-mm-thick plate (weld 6). The direction of welding is indicated by the arrow. The strands of porosity that stretch from the bottom of the plate and connect in the center of the defect were common in all the hybrid welds where root defects formed; B — laser weld in 9.5-mm-thick plate (weld 3) as determined by X-ray computed tomography. Only individual pores are observed. Evidence of gouging due to material loss to root defects can be observed at the top of the plate.

welding. The optics system utilizes collimating and focusing lenses with 200- and 500-mm focal lengths, respectively. The 1-μm laser wavelength is transported to the welding head through a 200-μm-diameter process fiber. The focused spot size and full divergence angle were measured with a Primes® Focus Monitor and are 0.52 mm and 64 mrad, respectively. A Lincoln Electric® Power Wave 455 M/STT power source with a Binzel® WH 455D water-cooled welding gun was used with ER 70S-6 welding wire for the hybrid welding experiments.

In both the laser and hybrid laser-arc welding processes performed here, laser power, defocus, laser-arc separation distance, and arc voltage were kept constant at 5 kW, 8 mm, 3 mm, and 31 V, respectively, while wire feed speed, arc current and travel speed were varied when welding on 4.8-mm-thick plate. A positive 8-mm defocus indicates that the position of focus is above the plate. When welding on a 9.8-mm-thick plate, 7-kW laser power and zero defocus were selected. Additionally, to test the effect of the oxide presence on the bottom surface, two types of plate were used, one with only the top surface of the plate sand blasted to remove the oxide. The other plate had the oxide removed on both sides. A summary of the welding parameters is given in Table 1. Oxide removed refers to whether the oxide scale was removed on both sides prior to welding. The welding processes were laser beam welding (LBW) and hybrid laser-arc welding (HLAW). Standard metallographic techniques were used to inspect the transverse cross-sections of the welds.

X-ray CT images were captured with a General Electric® v|tome|x CT system. The accelerating voltage and current for each scan were 280 kV and 180 μA, respectively. The voxel (i.e., 3D pixel) size with a magnification of 20× was 50 μm. DatosX® software handled the reconstruction of the individual X-ray images to produce the 3D image. The defect detection module in the Volume Graphics® VGStudio Max software was used to highlight the internal pore structure of the weld defects.

Results and Discussion

Root Defect Formation and Characterization

Based on previous research (Refs. 12, 15, 19, 20), surface tension and weld pool volume are thought to play a part in the formation of root defects. The surface tension at the bottom of the plate will restrain the liquid metal in the weld pool and discourage root defect formation. On the other hand, the weight of the molten metal in the weld pool will act to promote the formation of root defects. The competition between these two forces will determine whether defects will form.

In order to investigate the relationship between the surface tension and weld pool volume, both were independently varied during welding experiments. The presence of oxygen in molten iron has a significant effect on the surface tension. At high oxygen contents between 0.06 and 0.1 wt-%, the surface tension of liquid iron is lowered by 50% or more (Ref. 21) of its oxygen-free value, 1.91 N/m (Ref. 22). Oxygen content can be controlled indirectly by the removal of the oxide scale, which is present on both surfaces of the plate. In these experiments, welds with a high surface tension were ensured by first removing the oxide scale from both surfaces of

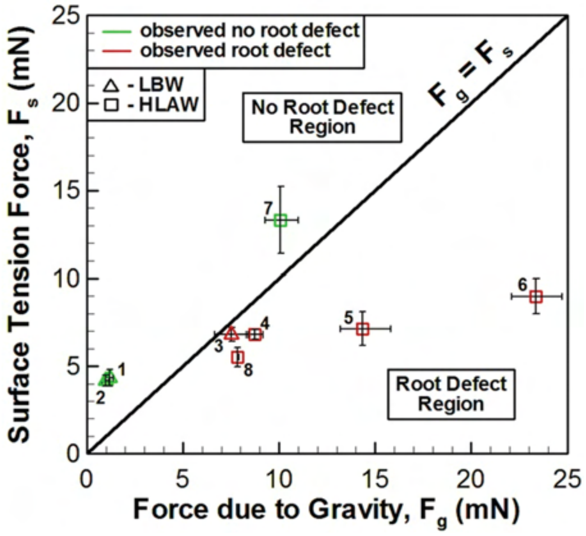

Fig. 5 — The comparison of surface tension force and weight force for the experimental welds considered. The numbers next to each weld indicate the processing conditions as shown in Table 1. Compared to experimental results, all the welds are found to be on the correct side of the $F_g = F_s$ line.

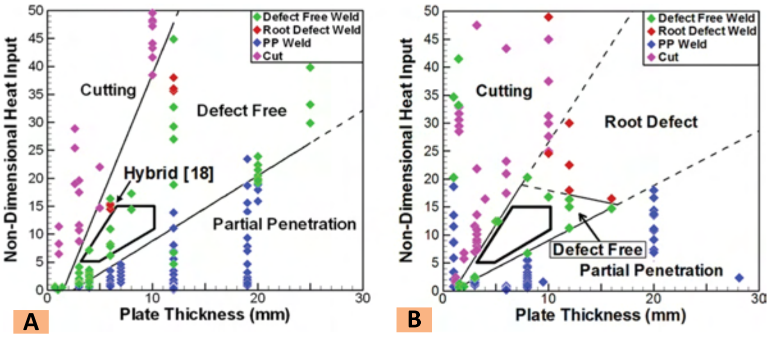

Fig. 6 — Process maps for: A — Low-carbon steels; B — 304 stainless steel — were constructed from available reports of laser welding and cutting experiments. The maps indicate with what processing conditions acceptable complete penetration welds can be made with respect to other interaction modes.

the steel plate. Low surface tension weld pools were acquired by only removing the oxide scale from the top surface and not grinding the bottom surface. Oxygen pickup is a contributor but not the sole source of root defects. In this case, the oxide scale acts as a source of oxygen that leads to a lower surface tension of the molten metal at the root of the weld but is not a necessary condition for root defect formation. The volume of the weld pool was varied by increasing the heat input by transitioning from laser to hybrid laser-arc welding or by increasing plate thickness. Higher heat inputs and greater plate thicknesses produce more molten metal during complete joint penetration welding.

In examining the effect of lower surface tension, hybrid welds (welds 7, 8) were made under the same conditions, with the exception of the oxide scale presence on the bottom surface. The weld with scale (weld 8) formed root defects most likely because the restraining surface tension force was much lower due to the increased oxygen content. On the other hand, the weld without scale (weld 7) formed no root defects. A comparison of the bottom surfaces and transverse weld cross sections are shown in Fig. 1B, C and Fig. 2, respectively. In Fig. 1, irregularly spaced root defects can be observed in the weld with bottom surface oxide scale. While the weld without scale contains some reenforcement on the bottom surface, there are no observable defects. As can be observed in Fig. 2, root defects have a profound effect on the weld cross section. The weld without scale has a clearly identifiable arc zone at the top, which is much wider than the rest of the weld. In the weld with scale, the weld width is much narrower, and the complex shape of the porosity in the root defect nugget is observable. Eleven hybrid welds were made with and eight hybrid welds made without bottom surface oxide scale. In all cases, the welds without bottom surface scale did not form root defects, while those with scale did form defects.

The effect of heat input and liquid metal volume on the root defect formation was investigated next for a series of welds made at a travel speed of 30 mm/s. As shown in Table 1, the laser weld (weld 1) has a heat input of 167 J/mm, while the hybrid welds (welds 4–6) had estimated heat inputs between 426 and 695 J/mm. The higher heat inputs should increase the size of the weld pool, which will increase the overall weight that must be balanced against the surface tension force at the bottom of the pool. At the lowest heat input, there were no root defects, but defects formed at the high heat inputs. The effect of heat input on the size of the weld and amount of material melted can be observed in

Table 2 — Average and Standard Deviations of Three Measurements for the Top Surface and Bottom Surface Weld Width and Weld Length and the Estimated Arc Force

Weld Number	D (mm)	d (mm)	l (mm)	Arc Force (mN)
1	2.2 ± 0.1	1.6 ±0.2	3.7 ± 0.8	0.0
2	1.9 ± 0.2	1.5 ± 0.1	3.4 ± 0.7	0.0
3	4.2 ± 0.2	2.5 ± 0.1	6.9 ± 0.6	0.0
4	4.9 ± 0.2	2.5 ± 0.1	13.8 ± 0.7	9.0
5	6.4 ± 0.9	2.6 ± 0.3	17.0 ± 2.3	39.4
6	7.8 ± 0.4	3.3 ± 0.4	28.6 ± 1.8	74.3
7	6.1 ± 0.3	2.2 ± 0.3	15.8 ± 2.2	14.0
8	3.9 ± 0.5	2.0 ± 0.2	8.4 ± 2.2	14.0

Fig. 3, which shows the transverse weld cross sections of the laser weld (weld 1) and the lowest heat input hybrid weld (weld 4). The hybrid weld is much larger in terms of cross-sectional area compared to the laser weld, and the high pool volume combined with the suppression of surface tension from the bottom surface scale promoted the formation of root defects.

Postweld observation showed that some of the defect nuggets were missing portions of the outer wall, which can be seen in one of the nuggets of Fig. 1C and indicates that porosity may be present. In Figs. 2 and 3, micrographs show complex pore shapes. The internal structure of the root defect nuggets was characterized with X-ray CT, which nondestructively evaluates internal defects by differentiating regions of different density. Within a metal structure, pores appear brighter since fewer X-rays are absorbed.

Typical internal structures of root defects formed during hybrid laser-arc welding and laser welding are shown in Fig. 4. The porosity is represented by the yellow colored shapes within the defects. The large pore in the hybrid weld is fully interconnected. Eight arms start at the edges of the weld and extend down to the bottom of the root defect nugget where they connect to a large central pore. This interconnected porosity contrasts with pores shown in Figure 4B for a laser weld fabricated in thicker plate. In this defect, there is only a dispersion of smaller spherical pores, which are only present in the top half of the defect. Large gouges in the top surface resulting from the loss of material to the defect are also visible in Fig. 4B.

Clearly, the laser and hybrid welding processes produced different pore shapes and sizes within the weld defects. Typically, in laser welding processes, where large spherical pores are present, keyhole collapse (Ref. 7) results in pores centered on the laser beam axis. Based on video evidence of root defects forming and growing along the length of the pool away from the keyhole (Ref. 12) and X-ray CT images of complex pore networks and different characteristics for different welding processes, keyhole dynamics probably cannot be used to explain the porosity structures within the weld defect nuggets. The most likely explanation is that the additional forces in arc welding, such as the arc pressure and droplet impact force, led to the network of pores observed in Fig. 4A.

Mechanism of Root Defect Formation

The formation of weld root defects can be viewed as a force balance between the weight of the liquid metal in the weld pool and the surface tension force. A model has been developed to calculate the magnitude of each force and utilizes an approximate weld pool shape and measured weld bead dimensions. The details of the model are given in Appendix A. The results of the force balance between weight and surface tension are shown in Fig. 5. The numbers next to each point indicate which weld is plotted. Error bars represent the spread in values calculated with the uncertainty for each measured dimension given in Table 2. The model is physically consistent, since as heat input increases, the calculated values for weight due to gravity and surface tension force also increase. The $F_g = F_s$ line defines the boundary between regions where root defects will (to the right of the line) and will not (to the left of the line) occur.

The laser welds (welds 1–3) have the lowest weight forces (i.e., points farthest to the left in Fig. 5) due to the low heat input of the laser and the resulting small pool volumes compared to hybrid welds. Laser welds fabricated on 4.8-mm plate (welds 1, 2) did not form a defect since the surface tension force of 4 mN easily restrained the weight force of 1 mN. However, when complete joint penetration laser welds were made on thicker plate of 9.5 mm (weld 3), the weight force increased to 7.5 mN and exceeded the surface tension of less than 7 mN, and defects formed. The force balance captures the difference in plate thicknesses and predicts the observed outcome for the laser welds.

For the laser and hybrid laser-arc welds with the same 30 mm/s welding speed (welds 1, 4–6), the model predicts increasing weight due to gravity from 1 to 23 mN due to increasing heat input, but the surface tension only increased from 4 to 9 mN. The model predictions for these welds agree with the experimental observations. The force balance also captures the differences in welds on plates with and without bottom surface oxide and identical process conditions (welds 7, 8) with similar weight forces of 8 and 10 mN, respectively. With the presence of the oxide scale, though, weld 8 possesses only 40% of the surface tension force of weld 7, which had no oxide scale. As a whole, agreement is good between the observed and predicted formation of root defects with all of the green symbols, indicating no observed root defects, falling above the $F_g = F_s$ line and all the red symbols, indicating observed defects, below the same line. These results indicate that representation of the root defect formation phenomenon as a quantitative force balance between weight and surface tension allows for a qualitative prediction of an important welding defect.

Process Maps for Complete Joint Penetration Laser Welding

The results described above indicate that both heat input and plate thickness affect the formation of root defects in DH36 steel and are expected to play a role in other alloys. For given laser welding parameters, material properties, and plate thicknesses, however, the developed model cannot provide a broader predictive capability of root defect formation. Additionally, the process parameters that produce defect-free complete-joint-penetration welds are bounded by other laser-material interaction modes, such as cutting and partial-penetration laser welding. In order to address these additional complexities, process maps that tie together laser welding parameters, material properties, heat input, plate thickness, and laser-material interaction modes are constructed for different alloy systems. Comparison of process maps for different alloys should show where similarities exist and what conclusions apply across material types.

Process maps have been constructed for laser processing of low-carbon steels and 304 stainless steel. The nondimensional heat input per unit length, which is similar to that used by De and DebRoy (Ref. 23) includes laser welding parameters and material properties and is defined as

$$H^* = \frac{\frac{\eta P}{U}}{\rho(h+\Delta H_v)\pi r_b^2} \qquad (1)$$

Table 3 — Values Used to Construct the Process Maps

Alloy	$\eta - 1\mu m$	$\eta - 10.6\mu m$	ρ (kg/m^3)	h (kJ/kg)	ΔH_v (kJ/kg)
Steel	0.34	0.12	7030	2390	6260
304SS	0.34	0.12	7070	2290	6330

Note: Absorptivity, η, depends on the wavelength of the laser beam.

where η is absorptivity, P is laser power, r_b is the laser beam radius at focus, U is the welding speed, ρ is the liquid metal density, h is the enthalpy of the liquid at the boiling point, and ΔHv is the heat of vaporization. Both the numerator and denominator have units of energy per unit length, J/m. Equation 1 compares the amount of energy absorbed from the laser per unit length in the numerator to the amount of energy per unit length necessary to heat the alloy from room temperature to the boiling point (denominator). For the experiments considered here, H* is typically greater than one, indicating that absorbed laser energy is a multiple of the energy to heat the alloy to the boiling point. The material property values that were used to calculate H* for each alloy are given in Table 3. Estimated resistivities (Ref. 24) were used to calculate absorptivity (Ref. 25), and density, enthalpy, and heat of vaporization were obtained from available references (Refs. 24, 26).

When H* is plotted as a function of plate thickness, four regions defining cutting, complete-joint-penetration weld without defects, complete-joint-penetration weld with defects, and partial-penetration weld, can be identified. In the case of cutting low-carbon steel or stainless steel in the presence of oxygen gas, laser energy accounts for approximately half of the total energy input into the system with oxidation of liquid iron accounting for the other half (Refs. 27, 28). Other processes, such as hybrid laser-arc welding, are not considered in these maps, but as shown previously, the addition of another heat source can increase the chances of root defect formation.

The process maps for the laser welding of low-carbon steel (Refs. 18, 27, 29–53) and 304 stainless steel (Refs. 14–16, 39, 40, 54–70) are shown in Fig. 6. Experimental H* data for cutting, complete-joint-penetration welds without root defects, and partial penetration welds are determined by macrographs of the welds or explicit statements in the text and plotted for every material type. Root defects reported in the literature are assumed to form because of the competition between the surface tension and liquid metal weight forces and not other phenomena, such as keyhole instability, which leads to macroporosity. The lines defining each region are fit to the complete-joint-penetration laser welding data. All the conditions shown are for a laser only, except as indicated in Fig. 6A, where a set of hybrid laser-GMAW conditions (Ref. 18) is used to show another case of root defects in low-carbon steel.

The points indicating root defect formation for low-carbon steel in 12-mm-thick plate (Ref. 31) are situated close to the cutting-complete joint penetration transition line. On the other hand, because of the availability of data, a line indicating the transition from defect-free welds to welds with root defects can be drawn for 304 stainless steel and fully encloses the complete-joint-penetration laser welding space for the alloy. According to the process map, the laser welding parameters for complete-joint-penetration welds in excess of 16 mm are very limited, so only careful selection of processing parameters can produce a defect-free weld. For the same space in low-carbon steel, relatively thick plates of 25 mm can be welded at nondimensional heat inputs of less than 40.

Comparison of the process maps shows relatively similar behaviors at lower heat inputs and plate thicknesses. This similarity across process maps is highlighted by the thick solid black line, which encloses an identical process space in the defect-free zone, and can be used to produce defect-free complete-joint-penetration welds for each alloy. For example, process parameters yielding an H* of 12 will produce a defect-free weld in 8-mm-thick plate of low-carbon steel and 304 stainless steel. Identical H* values for plate thicknesses between 3.5 and 10 mm can be used across alloy systems. The parameters shown in Fig. 6 can speed process parameter development, especially in thick plates, where greater heat inputs lead to longer cooling times between trial welds. For example, if laser optics are fixed (i.e., minimum laser beam radius cannot change), then welding engineers can quickly select nondimensional heat input from Fig. 6 for a given plate thickness and calculate via Eq. 1 the laser powers and welding speeds that will produce defect-free, complete-joint-penetration welds.

At higher heat inputs and plate thicknesses, the behaviors of each alloy diverge. A very small defect-free complete-joint-penetration process space is observed in 304 stainless steel. The opposite is observed in low-carbon steels. The process maps indicate that two conditions are necessary before root defects can form during laser welding. First, the plate thickness must be 10 mm or greater. Second, the nondimensional heat input must be greater than 16, which is also a minimum value associated with root defects. Once these two conditions are met, the formation of root defects becomes possible. However, as shown in the process maps, satisfying the conditions does not guarantee root defect formation. For example, the mean average H* value for root defect formation in low-carbon steel and 304 stainless steel laser welds is 33, so the chances of forming root defects increases as the heat input increases.

From the process maps, 304 stainless steel is more susceptible to root defect formation than low-carbon steel. The reason is the difference in surface tension, which is 1.91 N/m (Ref. 22) and 1.17 N/m (Ref. 79) for steel and stainless steel, respectively. The density of each liquid alloy is 7030 kg/m^3 for steel and 7070 kg/m^3 for 304 stainless steel (Ref. 24). Both surface tension and density should affect the formation of root defects as shown in Eq. A5 and A7, and only surface tension is very different between the two alloys.

Close inspection of Fig. 6A, B indicates that root defects are associated with relatively higher heat inputs. For low-carbon steel, the root defects in both laser and hybrid welding conditions are close to the cutting transition line, indicating high heat input. In the case of 304 stainless steel, all the heat inputs associated with root defects are greater than the defect-free heat inputs for the same plate thicknesses, 10, 12, and 16 mm.

Some researchers have concluded that the root defects are associated with low heat input (Refs. 11, 18, 31). However, the data compiled in Fig. 6A, B suggest that the opposite is true. In cases where lower heat inputs certainly led to root defect formation, it appears that the researchers were already operating at a high heat input. For example, for 12-mm-thick low-carbon steel plate (Ref. 31) and nondimensional heat inputs between 35 and 40, defects formed, but at lower heat inputs of 29 and 33 and higher heat inputs of 45 and 50 root defects did not form. Additionally, all of these heat inputs are relatively high because complete-joint-penetration defect-free welds were made at nondimensional heat inputs as low as 5 and 7 (Ref. 31). By considering the whole range of process parameters captured in the nondimensional heat input parameter, the fact that root defects are a high heat input phenomenon becomes clear and unambiguous.

Summary and Conclusions

The root defect in complete-joint-penetration laser and hybrid laser-arc welding has been experimentally and theoretically investigated. Welding parameters, plate preparation, and plate size were varied to produce welds with and without root defects. Optical microscopy and X-ray CT characterized the internal structure of the defect nuggets for different welding processes. A force balance between the weight of the liquid metal and the surface tension was developed to describe the competing forces driving the onset of defect formation. Process maps for two alloy systems have been constructed based on the experimental welding and cutting parameters reported in the literature. The conclusions of this work are listed below.

1) The qualitative effect of surface tension and weight of liquid metal on the formation of root defects was determined by varying the welding parameters. A decrease in surface tension due to the presence of oxide scale on the bottom plate surface led to the defect formation while no defects formed for the same conditions on a plate with the oxide scale removed. Larger weld pools were formed either by increasing heat input with the addition of an arc or laser welding on 9.5-mm-thick plate. The larger pools led to root defects, while the laser welds on 4.8-mm-thick plate formed smaller pools and did not result in root defects.

2) With the use of X-ray CT, the internal structure of defect nuggets formed during hybrid laser-arc and laser welding were found to be different. In hybrid welding, the structure consisted of a network of large pore strands that stretched from the edge of the bottom weld bead to the center of the defect nugget. On the other hand, defect nuggets resulting from a laser weld showed a dispersion of small spherical pores. The additional arc pressure and droplet impact forces in hybrid welding are the likely factors for the difference in porosity structure.

3) Based on the observations of surface tension and weight of liquid metal, a force balance between the two was developed for an idealized weld pool and applied to the experimental conditions used in the study. The force balance calculations matched the experimental observations in terms of root defect formation for all of the cases considered. The results showed that the force balance has utility for predicting the defect formation, assuming the pool geometry is known or can be calculated.

4) The process maps for low-carbon steel and 304 stainless steel revealed that identical H* values between 5 and 15 can be used to fabricate defect-free welds in plate thicknesses between 3.5 and 10 mm for the two alloys considered.

5) The compiled data show that two conditions, plate thicknesses greater than 10 mm and H* values greater than 15, must be met before root defects can form. Consideration of the heat inputs necessary to form root defects in low-carbon steel and stainless steel demonstrated that root defects are a high heat input phenomenon, so in most cases, reducing heat input will eliminate defect formation.

Acknowledgments

The authors would like to thank Mr. Jay Tressler for performing the welding experiments and Mr. Ed Good for preparing the metallographic and X-ray specimens. This research was performed using funding received from the DOE Office of Nuclear Energy's Nuclear Energy University Programs under Grant Number 120327.

References

1. Zhang, J., Shan, J. G., Ren, J. L, and Wen, P. 2013. Reducing the porosity in die-cast magnesium alloys during laser welding. *Welding Journal* 92(4): 101-s to 109-s.

2. Roepke, C., Liu, S., Kelly, S., and Martukanitz, R. 2010. Hybrid laser arc welding process evaluation on DH36 and EH36 steel. *Welding Journal* 89(7): 140-s to 150-s.

3. Sachez-Amaya, J. M., Boukha, Z., Amaya-Vazquez, M. R., and Botana, F. J. 2012. Weldability of aluminum alloys with high-power diode laser. *Welding Journal* 91(5): 155-s to 161-s.

4. Victor, B., Farson, D. F., Ream, S., and Walters, C. T. 2011. Custom beam shaping for high-power fiber laser welding. *Welding Journal* 90(6): 113-s to 120-s.

5. Wu, S. C., Yu, X., Zuo, R. Z., Zhang, W. H., Xie, H. L., and Jiang, J. Z. 2013. Porosity, element loss, and strength model on softening behavior of hybrid laser arc welded Al-Zn-Mg-Cu alloy with synchrotron radiation analysis. *Welding Journal* 92(3): 64-s to 71-s.

6. Ribic, B., Palmer, T. A., and DebRoy, T. 2009. Problems and issues in laser-arc hybrid welding. *Int. Mater. Rev.* 54(4): 223–244.

7. Matsunawa, A., Kim, J.-D., Seto, N., Mizutani, M., and Katayama, S. 1998. Dynamics of keyhole and molten pool in laser welding. *J. Laser Appl.* 10(6): 247–254.

8. Tucker, J. D., Nolan, T. K., Martin, A. J., and Young, G. A. 2012. Effect of travel speed and beam focus on porosity in alloy 690 laser welds. *JOM* 64(12): 1409–1417.

9. Madison, J. D., and Aagesen, L. K. 2012. Quantitative characterization of porosity in laser welds of stainless steel. *Scripta Mater.* 67(9): 783–786.

10. Salminen, A., Piili, H., and Purtonen, T. 2010. The characteristics of high power fibre laser welding. *Proc. IMechE, Part C J. Mech. Eng. Sci.* 224(C5): 1019–1029.

11. Havrilla, D., Rominger, V., Holzer, M., Harrer, T., and Andreev, A. 2013. Advanced welding techniques with optimized accessories for high brightness 1 µm lasers. *Proc. SPIE 8603, High-Power Laser Mater. Process.: Lasers, Beam Deliv., Diagn., and Appl. II*. Ed. F. Dorsch, 86030N. SPIE.

12. Ilar, T., Eriksson, I., Powell, J., and Kaplan, A. 2012. Root humping in laser welding — an investigation based on high speed imaging. *7th Conf. Laser Assist. Net Shape Eng./Int. Conf. Photonic Eng.* Eds. M. Schmidt, F. Vollertsen, and M. Geiger, pp. 27–32. Elsevier Sci.

13. Punkari, A., Weckman, D. C., and Kerr, H. W. 2003. Effects of magnesium content on dual beam Nd:YAG laser welding of Al-Mg alloys. *Sci. Technol. Weld. Joining* 8(4): 269–281.

14. Zhang, M., Chen, G., Zhou, Y., and Liao, S. 2014. Optimization of deep penetration laser welding of thick stainless steel with a 10 kW fiber laser. *Mater. Des.* 53: 568–576.

15. Bachmann, M., Avilov, V., Gumenyuk, A., and Rethmeier, M. 2014. Experimental and numerical investigation of an electromagnetic weld pool support system for high power laser beam welding of austenitic stainless steel. *J. Mater. Process. Technol.* 214(3): 578–591.

16. Kaplan, A. F. H., and Wiklund, G. 2011. Advanced welding analysis methods applied to heavy section welding with a 15 kW fibre laser. *Weld. World* 53: 295–300.

17. Ohnishi, T., Kawahito, Y., Mizutani, M., and Katayama, S. 2013. Butt welding of thick, high strength steel plate with a high power laser and hot wire to improve tolerance to gap variance and control weld metal oxygen content. *Sci. Technol. Weld. Joining* 18(4): 314–322.

18. Piili, H., Salminen, A., Harkko, P., and Lehtinen, J. 2008. Study of phenomenon of fibre-laser-mig/mag-hybrid-welding. *ICALEO 2008 – 27th Int. Congr. Appl. Lasers Electro-Opt.* pp. 506–515. Laser Inst. of America.

19. Avilov, V. V., Gumenyuk, A., Lammers, M., and Rethmeier, M. 2012. PA position full penetration high power laser beam welding of up to 30-mm-thick $AlMg_3$ plates using electromagnetic weld pool support. *Sci. Technol. Weld. Joining* 17(2): 128–133.

20. Bachmann, M., Avilov, V., Gumenyuk, A., and Rethmeier, M. 2012. Numerical simulation of full penetration laser beam welding of thick aluminium plates with inductive support. *J. Phys. D: Appl. Phys.* 45(3): 035201.

21. Keene, B. J. 1988. Review of data for the surface tension of iron and its binary alloys. *Int. Mater. Rev.* 33(1): 1–37.

22. Keene, B. J. 1993. Review of data for the surface tension of pure metals. *Int. Mater. Rev.* 38(4): 157–192.

23. De, A., and DebRoy, T. 2004. A smart model to estimate effective thermal conductivity and viscosity in the weld pool. *J. Appl. Phys.* 95(9): 5230–5240.

24. Gale, W. F. 2004. *Smithells Metals Reference Book*, 8th Edition. Burlington, Mass., Elsevier Butterworth-Heinemann.

25. Dowden, J., and Phiroze, K. 1995. A mathematical investigation of the penetration depth in the keyhole welding with continuous CO_2 lasers. J. *Phys. D: Appl. Phys.* 28(11): 2252–2261.

26. Pakratz, L. B. 1982. Thermodynamic properties of elements and oxides. U.S. Dept. of the Interior, Bureau of Mines, District of Columbia.

27. Hsu M. J., and Molian, P. A. 1994. Thermochemical modeling in CO_2 laser cutting of carbon steel. *J. Mater. Sci.* 29(21): 5607–5611.

28. Ivarson, A., Powell, J., and Magnusson, C. 1991. The role of oxidation in laser cutting stainless and mild steel. *J. Laser Appl.* 3(3): 41–45.

29. Krasnoperov, M. Y., Pieters, R. R. G. M., and Richardson, I. M. 2004. Weld pool geometry during keyhole laser welding of thin steel sheets. *Sci. Technol. Weld. Joining* 9(6): 501–506.

30. Sokolov, M., Salminen, A., Kuznetsov, M., and Tsibulskiy, I. 2011. Laser welding and weld hardness analysis of thick section S355 structural steel. *Mater. Des.* 32(10): 5127–5131.

31. Rominger, V., Haug, P., Speker, N., and Holzer, M. 2013. High-power full penetration welding behavior. *Laser Tech. J.* 10(3): 36–40.

32. Assuncao, E., Ganguly, S., Yapp, D., Williams, S., and Paradowska, A. 2011. Characterization of residual stress state in laser welded low carbon mild steel plates produced in keyhole and conduction mode. *Sci. Technol. Weld. Joining* 16(3): 239–243.

33. Cui, C., Hu, J., Gao, K., Pang, S., Yang, Y., Wang, H., and Guo, Z. 2008. Effects of process parameters on weld metal keyhole characteristics with CO_2 laser butt welding. *Lasers Eng.* 18(5-6): 319 –327.

34. Hamatani, H., Miyazaki, Y., Otani, T., and Ohkita, S. 2006. Minimization of heat-affected zone size in welded ultra-fined grained steel under cooling by liquid nitrogen during laser welding. *Mater. Sci. Eng. A* 426(1–2): 21–30.

35. Ion, J. C., Salminen, A. S., and Sun, Z. 1996. Process diagrams for laser beam welding of carbon manganese steels. *Welding Journal* 75(7): 225-s to 232-s.

36. Oefele, F., Musiol, J., Zaeh, M. F. 2008. Influence of remote-laser-welding parameters for an 8 kW fibre laser on the seam quality of steels. *ICALEO 2008 – 27th Int. Congr. Appl. Lasers Electro-Opt.* pp. 399–405. Laser Inst. of America.

37. Mori, K., and Miyamoto, I. 1997. In-process monitoring of laser welding by the analysis of ripples in the plasma emission. *J. Laser Appl.* 9(3): 155–159.

38. Vollertsen, F., Grunenwald, S., Rethmeier, M., Gumenyuk, A., Reisgen, U., Olschok, S. 2010. Welding thick steel plates with fibre lasers and GMAW. *Weld. World* 54(3–4): R62–R70.

39. Brown, R. T. 2008. Keyhole welding studies with a moderate-power, high-brightness fiber laser. *J. Laser Appl.* 20(4): 201–208.

40. Nakamura, S., Sakurai, M., Kamimuki, K., Inoue, T., and Ito, Y. 2000. Detection technique for transition between deep penetration mode and shallow penetration mode and shallow penetration mode in CO_2 laser welding of metals. *J. Phys. D: Appl. Phys.* 33(22): 2941–2948.

41. Kumar, N., Kataria, S., Shanmugarajan, B., Dash, S., Tyagi, A. K., Padmananbham, G., and Raj, B. 2010. Contact mechanical studies on continuous wave CO_2 laser beam weld of mild steel with ambient and under water medium. *Mater. Des.* 31(8): 3610–3617.

42. Miranda, R., Quintino, L., Willams, S., and Yapp, D. 2010. Welding with high power fiber laser API5L-X100 pipeline steel. *5th Int. Mater. Symp./14th Conf. Soc.-Port.-Mater.* Eds. L. G. Rosa and F. Margarido, pp. 592–596. Trans Tech Publ.

43. Quintino, L., Costa, A., Miranda, R., Yapp, D., Kumar, V., and Kong, C. J. 2007. Welding with high power fiber lasers — a preliminary study. *Mater. Des.* 28(4): 1231–1237.

44. Suder, W. J., and Williams, S. 2014. Power factor model for selection of welding parameters in CW laser welding. *Opt. Laser. Technol.* 56: 223–229.

45. Chen, S.-L. 1998. The effect of gas composition on the CO_2 laser cutting of mild steel. *J. Mater. Process. Technol.* 73(1–3): 147–159.

46. Lo, K. H. 2012. A comparative study on Nd:YAG laser cutting of steel and stainless steel using continuous, square, and sine waveforms. *J. Mater. Eng. Perform.* 21(6): 907–914.

47. Malikov, A. G., Orishich, A. M., and Shulyat'ev, V. B. 2009. Experimental optimization of the gas-assisted laser cutting of thick steel sheets. *Quantum Electron.* 39(6): 547–551.

48. O'Neill, W., and Steen, W. M. 1995. A three-dimensional analysis of gas entrainment operating during the laser-cutting process. *J. Phys. D: Appl. Phys.* 28(12):

12–18.

49. Powell, J., Al-Mashikhi, S. O., Kaplan, A. F. H., and Voisey, K. T. 2011. Fibre laser cutting of thin section mild steel: an explanation of the ‘striation free effect. *Opt. Lasers Eng.* 49(8): 1069–1075.

50. Shariff, S. M., Sundararajan, G., and Joshi, S. V. 1999. Parametric influence on cut quality attributes and generation of processing maps for laser cutting. *J. Laser Appl.* 11(2): 54–63.

51. Sobih, M., Crouse, P. L., and Li, L. 2007. Elimination of striation in laser cutting of mild steel. *J. Phys. D: Appl. Phys.* 40(22): 6908–6916.

52. Wandera, C., Kujanpaa, V., and Salminen, A. 2010. Laser power requirement for cutting thick-section steel and effects of processing parameters on mild steel cut quality. *Proc. IMechE Part B: J. Eng. Manuf.* 225(B5): 651–661.

53. Zaied, M., Miraoui, I., Boujelbene, M., and Bayraktar, E. 2013. Analysis of heat affected zone obtained by CO_2 laser cutting of low carbon steel (S235). *3rd Int. Congr. Adv. Appl. Phys. Mater. Sci.* Eds. A. Y. Oral, Z. B. Bahsi, and A. Sonmez, pp. 323–326. Amer. Inst. Phys.

54. Nath, A. K., Sridhar, R., Ganesh, P., and Kaul, R. 2002. Laser power coupling efficiency in conduction and keyhole welding of austenitic stainless steel. *Sadhana* 27: 383–292.

55. Bhargava, P., Paul, C. P., Mundra, G., Premsingh, C. H., Mishra, S. K., Nagpure, D., Kumar, A., and Kukreja, L. M. 2014. Study on weld bead surface profile and angular distortion in 6-mm-thick butt weld joints on SS304 using fiber laser. *Opt. Laser Eng.* 53: 152–157.

56. Nakabayashi, T., Wani, F., Hayakawa, A., Suzuki, S., and Yasuda, K. 2003. Thick plate welding with Nd:YAG laser and COIL. *1st Int. Symp. High-Power Laser Macroprocess*. Eds. I. Miyamoto, K. F. Kobayashi, K. Sugioka, R. Poprawe, H. Helvajian, pp. 416–421. SPIE.

57. Panstar, H., Salminen, A., Jansson, A., and Kujanpaa, V. 2004. Quality and costs analysis of laser welded all steel sandwich panels. *J. Laser Appl.* 16(2): 66–72.

58. Kawahito, Y., Mizutani, M., and Katayama, S. 2007. Elucidation of high-power fibre laser welding phenomena of stainless steel and effect of factors on weld geometry. *J. Phys. D: Appl. Phys.* 40(19): 5854–5859.

59. Ghany, K. A., and Newishy, M. 2005. Cutting of 1.2-mm-thick austenitic stainless steel sheet using pulsed and CW Nd:YAG laser. *J. Mater. Process. Technol.* 168(3): 438–447.

60. Hsu, M. J., and Molian, P. A. 1995. Off-axial, gas-jet-assisted, laser cutting of 6.35-mm-thick stainless steel. *Trans. ASME* 117(2): 272–276.

61. Ilavarasan, P. M., and Molian, P. A. 1995. Laser cutting of thick sectioned steels using gas flow impingement on the erosion front. J. *Laser Appl.* 7(4): 199–209.

62. Purtonen, T., and Salminen, A. 2014. A study on the effect of cutting position on performance of fiber laser cutting of stainless steel tubes. *Weld. World* 58(2): 193–204.

63. Sheng, P. S., and Joshi, V. S. 1995. Analysis of heat-affected zone formation for laser cutting of stainless steel. *J. Mater. Process. Technol.* 53(3–4): 879–892.

64. Sparkes, M., Gross, M., Celotto, S., Zhang, T., and O’Neill, W. 2008. Practical and theoretical investigations into inert gas cutting of 304 stainless steel using a high brightness fiber laser. *J. Laser Appl.* 20(1): 59–67.

65. Stelzer, S., Mahrle, A., Wetzig, A., and Beyer, E. 2013. Experimental investigations on fusion cutting stainless steel with fiber and CO_2 laser beams. *7th Int. WLT Conf. Lasers Manuf.* Eds. C. Emmelmann, M. F. Zaeh, T. Graf, and M. Schmidt, pp. 392–397. Elsevier Sci. BV.

66. Wandera, C., Salminen, A., and Kujanpaa, V. 2009. Inert gas cutting of thick-section stainless steel and medium-section aluminum using a high power fiber laser. *J. Laser Appl.* 21(3): 154–161.

67. Kuo, T. Y., and Jeng, S. L. 2005. Porosity reduction in Nd-YAG laser welding of stainless steel and inconel alloy by using a pulsed wave. *J. Phys. D: Appl. Phys.* 38(5): 722–728.

68. Rizzi, D., Sibillano, T., Calabrese, P. P., Ancona, A., and Lugara, P. M. 2011. Spectroscopic, energetic, and metallographic investigations of the laser lap welding of AISI 304 using the response surface methodology. *Opt. Lasers Eng.* 49(7): 892–898.

69. Hartwig, L., Ebert, R., Kloetzer, S., Weinhold, S., Dreschel, J., Peuckert, F., Schille, J., and Exner, H. 2010. Material processing with a 3 kW single mode fibre laser. *J. Laser Micro/Nanoeng.* 5(2): 128–133.

70. Kawahito, Y., Mizutani, M., Katayama, S. 2009. High quality welding of stainless steel with 10 kW high power fibre laser. *Sci. Technol. Weld. Joining* 14(4): 288–294.

71. Mills, K. C. 2002. *Recommended Values of Thermophysical Properties for Selected Commercial Alloys*. Cambridge, Woodhead.

72. Blecher, J. J., Palmer, T. A., and DebRoy, T. 2014. Solidification map of a nickel base alloy. *Metall. Mater. Trans.* A 45A(4): 2142–2151.

73. Brohnstein, I. N. 2007. *Handbook of Mathematics*, 5th Edition. New York, N.Y., Springer.

74. Halliday, D., Resnick, R., and Walker, J. 2005. *Fundamentals of Physics*, 7th Ed. Hoboken, N.J., John Wiley & Sons, Inc.

75. Lin, L., and Eagar, T. W. 1986. Pressures produced by gas tungsten arcs. *Metall. Trans. B.* 17B(3): 601–607.

76. Rai, R., and DebRoy, I. 2008. Numerical simulation of heat transfer and fluid flow in GTA/ laser hybrid welding. *Sci. Technol. weld. Joining* 13(8): 683–693.

77. Zhang, W., Kim, C.-H., and DebRoy, T. 2004. Heat and fluid flow in complex joints during gas metal arc welding — Part II: Application to fillet welding of mild steel. *J. Appl. Phys.* 95(9): 5220–5229.

78. Basu, S., and DebRoy, T. 1992. Liquid metal expulsion during laser irradiation. *J. Appl. Phys.* 72(8): 3317–3322.

79. He, X., Norris, J. T., Fuerschbach, P. W., and DebRoy, T. 2006. Liquid metal expulsion during laser spot welding of 304 stainless steel. *J. Phys. D: Appl. Phys.* 39(3): 525–534.

80. Garandet, J. P., Vinet, B., and Gros, P. 1994. Considerations on the pendant drop method: a new look at Tate’s law and Harkin’s correction factor. J. *Colloid Interface Sci.* 165(2): 351–354.

Appendix A

Calculation of Surface Tension and Liquid Metal Weight

To calculate the force balance between surface tension and liquid metal weight, the approximated weld pool is split into two general parts as illustrated in Fig. A1. The leading segment of the weld pool, where the laser is interacting with the liquid metal, is rounded and semicircular in shape and extends through the thickness of the plate. The trailing section of the weld, especially at higher welding speeds, can take a triangular appearance at the top surface but does not extend through the entire plate thickness. There is some boundary between the pool and solidified material that extends from the end of the pool on the top surface to the edge of the pool on the bottom surface. Similarly, the volume of the idealized weld pool, shown in Fig. A1, is split into two parts, a cylinder surrounded by half of a truncated cone, which are numbered 1 and 2, respectively, near the heat sources and an overlapping trapezoid base pyramid, which is divided between a rectangular base pyramid (3) and two triangle base pyramids (4 and 5). This idealized volume is comparable to numerical modeling results of partial-penetration laser welds made under similar conditions with depths of penetration close to the plate thickness used here (Ref. 72).

The various shapes are numbered as 1) cylinder, 2) truncated cone, 3) rectangle base pyramid, and 4) and 5) triangle base pyramid. The volumes are calculated as (Ref. 73)

$$V_1 = \tfrac{1}{4}\pi d^2 t \qquad \text{(A1)}$$

$$V_2 = \tfrac{1}{24}(\pi t)(D^2 + d^2 + Dd) - \tfrac{1}{2}V_1 \qquad \text{(A2)}$$

$$V_3 = \tfrac{1}{3}dtl - \tfrac{1}{2}V_1 \qquad \text{(A3)}$$

$$V_4 = V_5 = \tfrac{1}{12}(D - d)tl \qquad \text{(A4)}$$

where d is the bottom surface weld width, t is the plate thickness, D is the top surface weld width, and l is the distance from the position of maximum weld width to the trailing edge of the weld pool. Plate thickness is known, and the top and bottom surface widths can be measured from the weld bead. The distance, l, can be estimated from the top surface weld bead. Three measurements were made for the values D, d, and l in each weld and are given in Table 2 along with the standard deviations.

Most of the liquid steel in the weld is supported partially by underlying solid material, which either solidified or never melted. So, the entire weight of the liquid metal is not supported by the surface tension force at the bottom of the pool. This situation is accounted for by assuming each column of liquid is supported by a surface acting as an inclined plane (Ref. 74). The volume of liquid unsupported by any surface is the cylinder lying in the center of the truncated cone. The force of the liquid metal in the idealized weld pool that must be supported by the surface tension force is

$$F_g = \rho g[V_1 + (V_2 + V_4 + V_5 + V_s)\sin^2\theta_1 + V_3\sin^2\theta_2] \qquad \text{(A5)}$$

where ρ is the density of liquid iron, 7200 kg/m^3 (Ref. 24), g is acceleration due to gravity, θ_1 is the angle that the cone and the triangle base pyramids make with the bottom of the plate, and θ_2 is the angle that the rectangle base pyramid makes with the plate bottom. V_s is a small volume that is not considered in the five volumes and is determined by disc integration of triangle ABC in Fig. 7B.

Some of the welds considered are hybrid laser-arc welds, where filler metal is added to the molten pool. In this case, the filler metal was assumed to be spread evenly over the area of the idealized weld with each of the five volumes increasing based on top surface area fractions of each shape. The volume of filler metal added over the length of the weld pool is

$$V_M = \frac{V_w \pi d_w^2}{4}\,\frac{\frac{1}{2}D + l}{U} \qquad \text{(A6)}$$

where v_w is the wire feed speed, d_w is the diameter of the filler metal wire, and U is the welding speed. The first fraction describes the volume of filler metal added to the weld per unit time. The time necessary for the arc to traverse the length of the weld pool is calculated in the second fraction. Additionally, arc pressure from the plasma will act on the weld pool during hybrid laser-gas metal arc welding. The total arc force has been measured by Lin and Eagar (Ref. 75) in gas tungsten arc welds for various torch angles and welding currents. The estimated forces (Ref. 75) are listed in Table 2, and since the arc is located over the rectangle base pyramid, the forces have been added to the rectangle base pyramid.

In the above derivations, recoil force and droplet impact force have not been taken into account. The recoil force results from evaporation at the molten pool surface, and the droplet impact force is due to the addition of liquid metal to the pool from the consumable electrode. The recoil pressure is a function of the equilibrium vapor pressure, which itself depends on the temperature of the liquid metal. Using the vapor pressure of liquid iron (Ref. 24), the recoil force (Ref. 76) with a 46 mm^2 weld pool surface area and 2500 K surface temperature is 0.4 mN. Due to the relatively low value of recoil force at a fairly high temperature, the effects of recoil pressure were neglected. Similarly, when the droplet mass and acceleration are estimated (Ref. 77) for the welding conditions studied, the maximum force is less than 1 mN, which is negligible compared to the other forces.

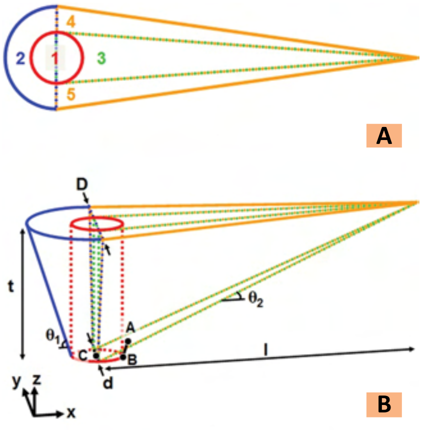

Fig. A1 — The idealized weld pool, which is used to estimate the volume and weight of the liquid metal, is shown as — A — A top-down view outlining the five volumes used to calculate total volume; B — a 3D view with the various variables, dimensions, and individual volumes.

The surface tension force is the restraining force that holds the liquid metal in the pool and prevents the formation of the root defect. This force is calculated as (Refs. 78,79)

$$F_s = \pi\sigma d \qquad \text{(A7)}$$

where σ is the surface tension of liquid steel at the melting point. In this geometry, the root of the weld pool acts as a pendant drop prior to detachment (Ref. 80). According to this formulation, the maximum surface tension force is normal to the plate. The determination of the surface tension for the pendant drop is calculated the same as Eq. A7 when the force is set equal to the weight of the droplet. For the plate that was ground on the bottom, the surface tension was taken as 1.91 N/m (Ref. 22), the value for pure iron. For those welds made on plates containing oxide scale on the bottom surface, the surface tension was taken as 0.88 N/m (Ref. 21), a value consistent with oxygen impurities in iron.

Appendix D:

Microstructure and Geometry in Low Alloy Steel Laser-Arc Hybrid Welding

Fusion Zone Microstructure and Geometry in Complete-Joint-Penetration Laser-Arc Hybrid Welding of Low-Alloy Steel

A process map indicates a martensite-free microstructure can be maintained over a wide range of welding parameters

BY H. L. WEI, J. J. BLECHER, T. A. PALMER, AND T. DEBROY

ABSTRACT

The fusion zone geometry and microstructure in complete-joint-penetration hybrid laser gas metal arc welds of a low-alloy steel are examined experimentally and theoretically. Weld geometry and spatially variable cooling rates are investigated using a three-dimensional heat transfer and fluid flow model. Experimentally measured microstructures are compared with those estimated from a microstructure model based on kinetics and thermodynamics of phase transformations, for a range of laser arc separation distances and heat inputs. Considerable variations in both cooling rates and microstructure were observed for the range of process parameters utilized. In fact, the experimental results and calculations show that for the same heat input, a predominantly ferritic and predominantly martensitic microstructure can be obtained, depending on the laser arc separation distance and resulting cooling rate. A process map is constructed showing the effect of welding speed, laser power, and laser arc separation distance on cooling rates and microconstituent volume fractions. The map indicates a martensite-free microstructure can be maintained over a wide range of welding parameters.

KEYWORDS

- Hybrid Welding • Heat Transfer and Fluid Flow • Microstructure
- Complete Joint Penetration • Laser • Gas Metal Arc • Cooling Rate

Introduction

Hybrid laser-arc welding is a process that combines laser beam welding and conventional arc welding in order to incorporate the benefits of both processes (Refs. 1–4). Hybrid laser-gas metal arc (GMA) welding produces wider weld pools than autogenous laser welding, and deeper weld penetration than GMA welding with the same parameters (Refs. 5–8). The combination of laser and arc energy sources allows for complete-joint-penetration welds to be achieved at significantly higher welding velocities in a single pass, while at the same time allowing large root openings in weld joints to be bridged (Refs. 9, 10). As a result, welding productivity can be greatly enhanced over that achieved by either laser or GMA welding alone (Refs. 11–13). In addition, hybrid laser-GMA welding has significant advantages in acquiring the desired weld metal microstructures, since lower cooling rates can be more easily obtained than in autogenous laser welding. However, martensite, which has very low ductility and toughness (Ref. 14), can still form in hybrid welding (Ref. 15).

Previous work on the hybrid laser-GMA welding of steels has largely focused on the experimental postcharacterization of weld geometries, microstructures, and mechanical properties (Refs. 15–21). However, these postmortem evaluations provide little detail on the evolution of weld pool geometries and the cooling rates within the fusion zone. In order to understand and predict weld metal microstructural evolution, the thermal cycles experienced during these welding processes must be known. The interactions between the heat sources and materials during complete-joint-penetration hybrid laser-GMA welding lead to rapid thermal cycles in the weld pool, which in turn impacts microstructure evolution. Phase transformations during cooling in the weld fusion zone have been extensively investigated both experimentally and theoretically. Bhadeshia et al. developed a phase transformation model (Refs. 22–24) based on thermodynamics and phase transformation kinetics. This model can quantitatively predict the microstructures and properties of weld deposits for different alloy compositions, cooling rates, and prior austenite grain sizes.

Direct measurement of temperature profiles in the interior of the weld pool still remains a major challenge. On the other hand, a well-tested three-dimensional mathematical model can provide accurate temperature fields and cooling rates at discrete locations throughout the fusion zone (Refs. 25, 26). Several studies focused on the numerical modeling of the fluid flow and heat transfer conditions within the molten weld pool of hybrid laser-arc welding (Refs. 6, 27). Ribic et al. (Ref. 27) numerically studied the effect of laser arc separation distance and laser power on heat transfer and fluid flow in partial-penetration hybrid laser-gas tungsten arc (GTA) welding by using a three-dimensional numerical model. They found that the distance between the laser and arc signifi-

H. L. WEI (huw15@psu.edu)*, J. J. BLECHER, and T. DEBROY are with Department of Materials Science and Engineering, and T. A. PALMER is with Applied Research Laboratory, The Pennsylvania State University, University Park, Pa.*

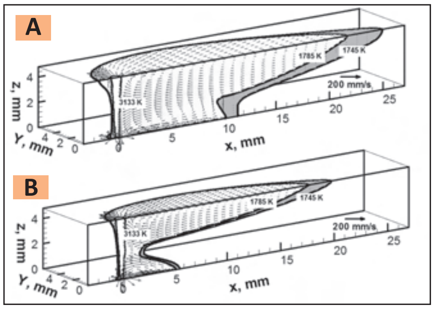

Fig. 1 — Top surface and symmetry plane of weld pool with temperature contours and velocity fields for the following: A — Welding speed of 20.0 mm/s, laser arc separation distance of 1 mm; B — welding speed of 30.0 mm/s, laser arc separation distance of 1 mm.

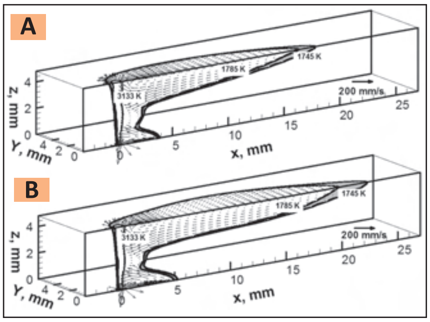

Fig. 3 — Top surface and symmetry plane of weld pool with temperature contours and velocity vectors for the following: A — Welding speed of 40.0 mm/s, laser arc separation distance of 1 mm; B — welding speed of 40.0 mm/s, laser arc separation distance of 5 mm.

cantly affected the cooling rates and that the weld penetration was maximized at an optimal laser arc separation distance (Ref. 27). Cho et al. (Ref. 6) simulated the molten weld pool geometry in laser-arc hybrid welding by solving the equations of continuity, momentum, and energy using a commercial package. They reported that the width of the weld was determined mainly by the GMA heat source and the penetration depth was strongly influenced by the laser (Ref. 6). However, there are very few systematic studies focused on the numerical simulation of weld profile evolution, cooling rates within the fusion zone, and the corresponding influence on the weld metal microstructures in complete-joint-penetration hybrid laser-GMA welding. The previous numerical studies (Refs. 6, 27) have discussed partial-penetration hybrid welding, where the fluid flow and heat transfer at the bottom of the molten weld pool are significantly different than those in complete-joint-penetration welding.

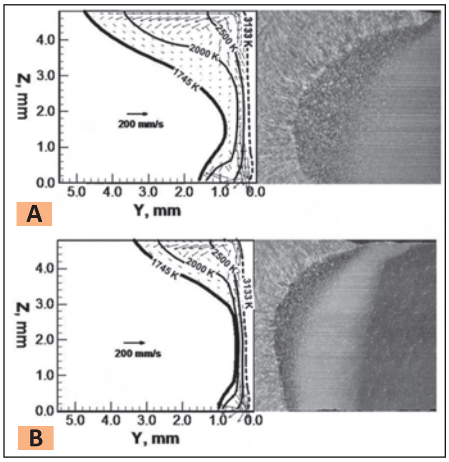

Fig. 2 — Comparison of experimental and simulated weld cross sections for the hybrid laser-GMA complete-joint-penetration welding of DH 36 steel for the following: A — Welding speed of 20.0 mm/s, laser arc separation distance of 1 mm; B — welding speed of 30.0 mm/s, laser arc separation distance of 1 mm.

In this work, the evolution of macro- and microstructures of complete-joint-penetration laser-GMA hybrid welds in DH 36 steel is analyzed using fundamental transport phenomena and phase transformation theory. A three-dimensional heat transfer and fluid flow model has been developed to study the effect of welding velocity and laser arc separation distance on weld geometries and cooling rates. Using the calculated cooling rates from the heat transfer and fluid flow model, a phase transformation model (Refs. 22–24) based on thermodynamics and phase transformation kinetics is used to provide a quantitative description of the final microstructures of the weld metal. The computed volume fractions of the weld metal allotriomorphic ferrite, Widmanstätten ferrite, acicular ferrite, and martensite are validated with corresponding experimental results for various welding conditions. The combined models are used to construct process maps capable of predicting the effect of welding parameters on resulting cooling rates and microstructures.

Experimental Procedure

Bead-on-plate complete-joint-penetration hybrid laser-GMA welds were made on 4.8-mm-thick DH 36 steel. An IPG Photonics® YLR-12000-L ytterbium fiber laser with a Precitec® YW50 welding head and a Lincoln Electric® Power Wave 455 M/STT welding power source with a Binzel® WH 455D water-cooled welding gun were used for hybrid welding. The maximum power of the fiber laser is 12 kW, with a wavelength of 1070–1080 nm. The optics system utilizes collimating and focusing lenses with 200- and 500-mm focal lengths, respectively. The laser is transported to the welding head through a 200-µm-diameter process fiber. The focal spot of the laser beam in the absence of plasma was approximately 0.56 mm in diameter. The laser was focused 8 mm above the surface of the plate. The laser power used in the welding experiments was fixed at 5.0 kW for all the cases. The electrode was 0.045-in.- (1.1-mm-) diameter ER70S-6 wire. The chemical compositions of DH 36 steel and ER70S-6 welding wire are given in Table 1. The metal transfer mode for the welding wire was in spray mode. The shielding gas was a mixture of 95% argon and 5% CO_2 with a flow rate of 95 ft^3/h (44.8 L/min). The welding velocities and laser arc separation distances were varied to study their effects on the weld profiles and weld metal microstructures. The key welding parameters are listed in Table 2. The top and bottom surfaces of the plate were

Table 1 — Chemical Composition of Base Metal DH 36 Steel (Ref. 10) and Welding Wire ER 70S-6 (wt-%)

	C	Mn	Si	Ni	Mo	Cr	V	P	S	Al	Nb	Ti	Cu
Base Metal	0.06	1.39	0.19	0.14	0.03	0.11	0.06	0.011	0.004	0.025	0.01	0.01	0.25
Welding Wire	0.09	1.63	0.90	0.05	0.05	0.05	0.05	0.007	0.007	0.000	0.00	0.00	0.20

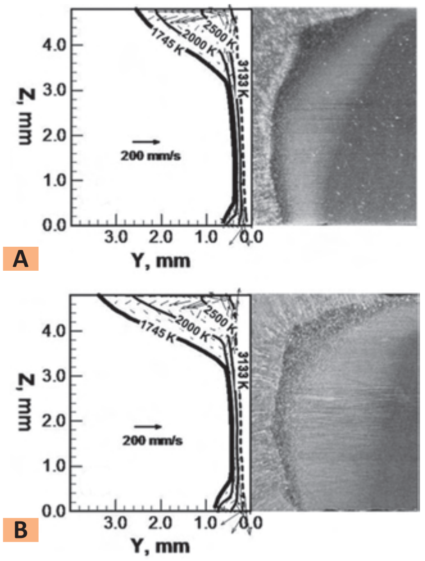

Fig. 4 — Comparison of experimental and simulated weld cross sections for the hybrid laser-GMA complete-joint-penetration welding of DH 36 steel for the following: A — Welding speed of 40.0 mm/s, laser arc separation distance of 1 mm; B — welding speed of 40.0 mm/s, laser arc separation distance of 5 mm.

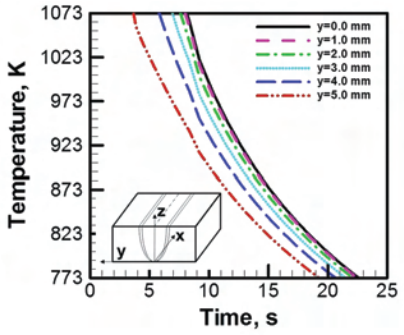

Fig. 5 — Calculated cooling curves at different y locations on the top surface of the fusion zone of weld 1 with welding speed of 20.0 mm/s, laser arc separation distance of 1 mm. The symbol y represents the distance from the weld centerline.

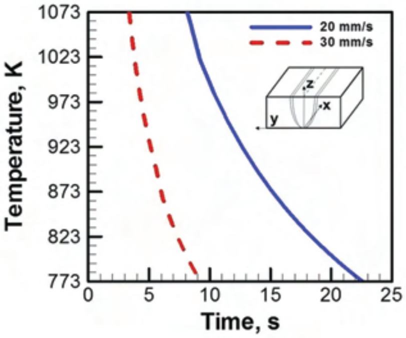

Fig. 6 — Comparison of the calculated cooling rates of the top center fusion zone for weld 1 with welding speed of 20.0 mm/s, laser arc separation distance of 1 mm, and weld 2 with welding speed of 30.0 mm/s, laser arc separation distance of 1 mm.

ground to remove scale prior to welding in order to avoid weld root defects during complete-joint-penetration welding. The sides of the plate were supported, so the welds were made without contacting the table below. Selected welds were sectioned, polished, etched, and photographed to reveal the weld fusion zone profile and microstructures. The volume fractions of selected microconstituents in the weld metal are determined by using the point counting method following the International Institute of Welding (IIW) guidelines (Ref. 28).

Mathematical Model

A three-dimensional heat transfer and fluid flow model for complete-joint-penetration hybrid laser-GMA welding was developed by modifying previous numerical simulation work (Refs. 27, 29, 31). Zhao et al. (Ref. 31) developed a transport phenomena-based numerical model to predict the keyhole geometry and temperature profiles in the weldment during keyhole laser welding. Rai et al. (Ref. 29) developed a convective heat transfer model for both partial and complete-joint-penetration keyhole mode laser welding of a structural steel based on the work of Zhao et al. (Ref. 31). Ribic et al. (Ref. 27) proposed a three-dimensional heat transfer and fluid flow model for partial-penetration hybrid laser-GTA welding. In this work, complete-joint-penetration hybrid laser-GMA welding is studied. Marangoni force-driven velocity boundary conditions at the bottom surface are assumed, which is different from that of partial-penetration hybrid welding. In addition, the heat transfer from the metal droplets during GMAW is integrated into the numerical model for hybrid laser-GMA welding. The material properties used in order to complete the welding calculations are given in Table 3. Details of the numerical simulation model are presented below.

Calculation of Keyhole Profile

The keyhole geometry is calculated using a model that considers material properties, welding process parameters, and specimen geometries. The detailed information about the model is available elsewhere (Refs. 30, 31) and only the salient features are presented here. The keyhole profile is calculated based on a point by point energy balance at the keyhole walls and is determined iteratively. Multiple reflections of the laser beam within the keyhole are assumed and the number of reflections is dependent on the keyhole geometry. The keyhole wall local temperature is taken as the boiling point of the alloy (Refs. 30, 31). Planar heat conduction from the keyhole wall into the workpiece is assumed due to the significantly higher temperature gradient in all directions in the horizontal plane compared to the vertical directions. Once the profile calculation is completed, the temperature distribution from the keyhole model is stored in a data file with all temperatures inside the keyhole assigned the boiling point temperature. This file is read into the heat transfer and fluid flow model, and at each horizontal x-y plane, the keyhole boundary is identified by a minimum and a maximum x value for any y value.

Heat Transfer in Weld Pool and Boundary Conditions

After the calculation of the keyhole profile, equations of conservation of mass, momentum, and energy are solved in three dimensions in the heat transfer and fluid flow model. Details about this model are available in the literature (Refs. 22, 23, 29) and only the

Table 2 — Welding Process Parameters for Complete-Joint-Penetration Hybrid Laser GMA Welding of DH 36 Steel

Weld Number	Laser Power (kW)	Arc Current (A)	Arc Voltage (V)	Welding Speed (mm/s)	Laser Arc Separation (mm)
1	5.0	248	31	20.0	1.0
2	5.0	235	31	30.0	1.0
3	5.0	232	31	40.0	1.0
4	5.0	232	31	40.0	5.0

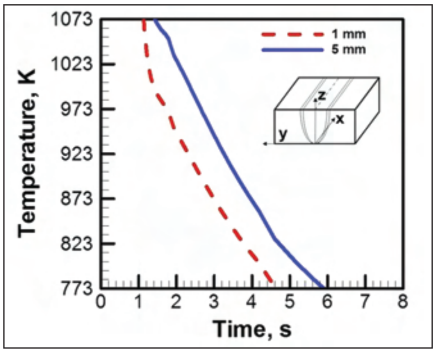

Fig. 7 — Comparison of the calculated cooling rates of the fusion zone located 1 mm above the bottom surface for weld 3 with welding speed of 40.0 mm/s, laser arc separation distance of 1 mm, and weld 4 with welding speed of 40.0 mm/s, laser arc separation distance of 5 mm.

salient features are presented here. The molten metal is assumed to be an incompressible, laminar, and Newtonian fluid. The liquid metal flow in the weld pool can be represented by the following momentum conservation equation (Refs. 30, 31):

$$\rho\frac{\partial u_j}{\partial t}+\rho\frac{\partial\left(u_i u_j\right)}{\partial x_i} = \frac{\partial}{\partial x_i}\left(\mu\frac{\partial u_j}{\partial x_i}\right)+S_j \qquad (1)$$

where ρ is the density, t is the time, x_i is the distance along the ith (i = 1, 2, and 3) orthogonal direction, u_j is the velocity component along the j direction, μ is the effective viscosity, and S_j is the source term for the jth momentum equation and is given as

$$S_j=-\frac{\partial p}{\partial x_j}+\frac{\partial}{\partial x_j}\left(\mu\frac{\partial u_j}{\partial x_j}\right) -C\left(\frac{\left(1-f_L\right)^2}{f_L^3+B}\right)u_j +\rho g\beta\left(T-T_{ref}\right)-\rho U\frac{\partial u_j}{\partial x_j} \qquad (2)$$

where p represents pressure, U is the welding speed, and β is the coefficient of volume expansion. The third term represents the frictional dissipation in the mushy zone according to the Carman-Kozeny equation for flow through a porous media (Refs. 32, 33) where f_L is the liquid fraction, B is a very small computational constant to avoid division by zero, and C is a constant accounting for the mushy zone morphology [a value of 1.6×10^4 was used in the present study (Ref. 34)]. The fourth term is the buoyancy source term (Refs. 23, 34, 35). The last term accounts for the relative motion of the workpiece relative to the laser and arc heat sources (Ref. 23).

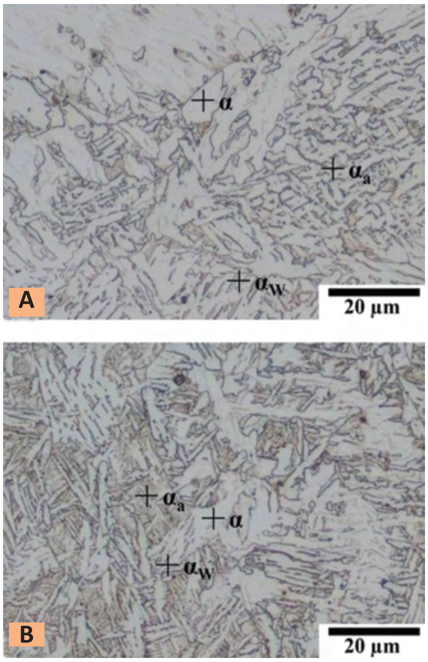

Fig. 8 — Comparison of the optical microstructures of the top center of the fusion zone by different welding speeds. Magnification 500x. A — Welding speed of 20.0 mm/s, laser arc separation distance of 1 mm; B — welding speed of 30.0 mm/s, laser arc separation distance of 1 mm. The symbols α, α_W, and α_a represent allotriomorphic, Widmanstätten, and acicular ferrite, respectively.

The following continuity equation is solved in conjunction with the momentum equation to obtain the pressure field.

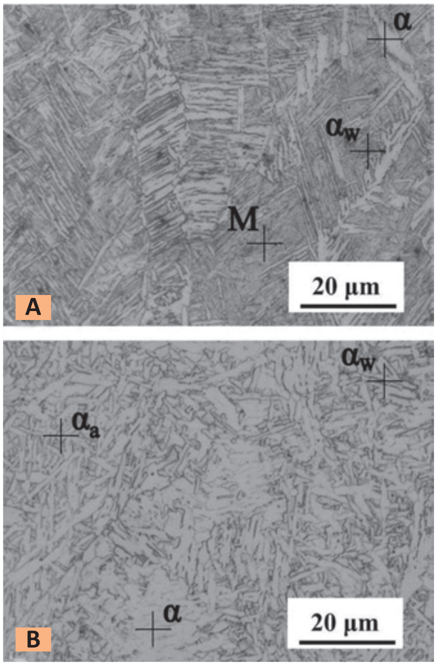

Fig. 9 — Comparison of the optical microstructures of the fusion zone located 1 mm above the bottom surface by different laser arc separation distances. Magnification 500x. A — Welding speed of 40.0 mm/s, laser arc separation distance of 1 mm; B — welding speed of 40.0 mm/s, laser arc separation distance of 5 mm. The symbols α, α_W, α_a, and M represent allotriomorphic, Widmanstätten, acicular ferrite, and martensite, respectively.

$$\frac{\partial\left(\rho u_i\right)}{\partial x_i}=0 \qquad (3)$$

In order to trace the weld pool liquid/solid interface, i.e., the phase change, the total enthalpy H is represented by a sum of sensible heat h and latent heat content ΔH, i.e., $H = h + \Delta H$

Table 3 — Material Properties Used for the Calculation of Temperature and Velocity Fields (Ref. 29)

Physical Property	DH 36 Steel
Boiling point (K)	3133
Solidus temperature (K)	1745
Liquidus temperature (K)	1785
Density (kg/m^3)	7200
Thermal conductivity (W/m-K)	21
Inverse Bremsstrahlung absorption coefficient (1/m)	100
Absorption coefficient (flat surface)	0.16
Molecular viscosity (Pa-s)	0.0067
Coefficient of thermal expansion (l/K)	1.96×10^{-5}
Temperature coefficient of surface tension (N/m K)	-0.5×10^{-3}
Enthalpy of solid at melting point (J/kg)	1.20×10^{6}
Enthalpy of liquid at melting point (J/kg)	1.26×10^{6}
Specific heat of solid (J/kg K)	710.6
Specific heat of liquid (J/kg K)	836.0

(Ref. 36). The sensible heat h is expressed as $h = \int C_p dT$, where C_p is the specific heat and T is the temperature. The latent heat content ΔH is given as $\Delta H = f_L L$, where L is the latent heat of fusion. The liquid fraction f_L is assumed to vary linearly with temperature for simplicity (Ref. 23) and is given as

$$f_L = \begin{cases} 1 & T > T_L \\ \dfrac{T - T_S}{T_L - T_S} & T_S \le T \le T_L \\ 0 & T < T_S \end{cases} \qquad (4)$$

where T_L and T_S are the liquidus and solidus temperature, respectively. Thus, the thermal energy transportation in the weld workpiece can be expressed by the following modified energy equation:

$$\rho\frac{\partial h}{\partial t} + \rho\frac{\partial(u_i h)}{\partial x_i} = \frac{\partial}{\partial x_i}\left(\frac{k}{C_p}\frac{\partial h}{\partial x_i}\right) + S_h \qquad (5)$$

where k is the thermal conductivity. The source term S_h is due to the latent heat content and is given as

$$S_h = -\rho\frac{\partial(\Delta H)}{\partial t} - \rho\frac{\partial(u_i \Delta H)}{\partial x_i} - \rho U\frac{\partial h}{\partial x_i} - \rho U\frac{\partial \Delta H}{\partial x_i} \qquad (6)$$

The heat transfer and fluid flow equations were solved for the complete workpiece. For the region inside the keyhole, the coefficients and source terms in the equations were adjusted to obtain boiling point temperature and zero fluid velocities.

A 3D Cartesian coordinate system is used in the calculation. Only half of the workpiece is considered since the weld is symmetrical about the weld centerline. At the bottom of the weld pool, Marangoni force-driven fluid velocity boundary conditions are assumed for complete-joint-penetration welding. A 187 × 77 × 26 grid system is used in the calculation and the corresponding calculation domain dimensions are 522 mm in length, 36 mm in half-width, and 4.8 mm in depth. The interactions between laser and arc as well as the heat transfer and fluid flow within the weld pool are affected by the separation distance between laser and arc. In the numerical model, the effect of arc energy on the formation of the keyhole and the energy transportation from the keyhole wall to the liquid weld pool are calculated. However, the laser-arc interaction, which has been characterized experimentally with optical emission spectroscopy (Ref. 37), is not rigorously simulated here.

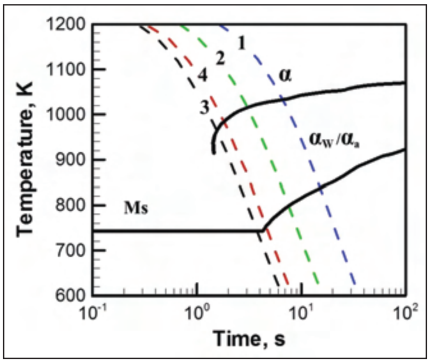

Fig. 10 — Calculated CCT diagrams with the cooling curves superimposed. Cooling rates are taken at the top center of welds with 1 mm laser arc separation distance and 20 and 30 mm/s welding speed (welds 1 and 2, respectively). Cooling rates are taken at 1 mm from the bottom surface of welds with 40 mm/s welding speed and 1 and 5 mm laser arc separation (welds 3 and 4, respectively). The symbols α, α_W, and α_a represent allotriomorphic, Widmanstätten, and acicular ferrite, respectively. Ms is the starting temperature for martensite formation.

During laser-GMA hybrid welding, the rates of heat, mass, and momentum transport are often enhanced because of the presence of fluctuating velocities in the weld pool. The contribution of the fluctuating velocities is considered by the incorporation of a turbulence model that provides a systematic framework for calculating effective viscosity and thermal conductivity (Refs. 32, 33). The values of these properties vary with the location in the weld pool and depend on the local fluid flow characteristics. In this work, a turbulence model based on Prandtl's mixing length hypothesis (Ref. 32) is used to estimate the turbulent viscosity.

Calculation of Heat Transfer from GMA Metal Droplets

The hot molten metal droplets produced by the GMAW process impinge into the weld pool at high velocities and carry a significant amount of heat into the liquid weld pool (Refs. 34–36, 38, 39). The heat transfer from the metal droplets was simulated by considering a cylindrical heat source with a time-averaged uniform power density (S_v). The use of a cylindrical volumetric heat source assumes the spray transfer mode of the droplets, which is consistent with the welding conditions in the present study.

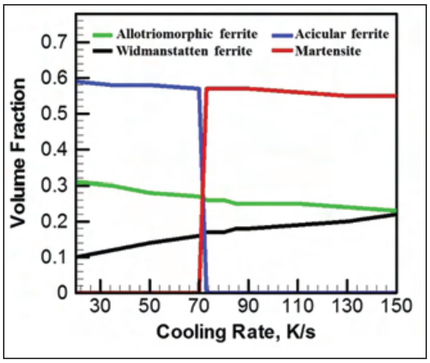

Fig. 11 — Variation of the volume fractions of allotriomorphic ferrite, Widmanstätten ferrite, acicular ferrite, and martensite with different cooling rates.

In order to calculate S_v, the radius of the heat source, its effective height, and the total sensible heat input by the droplets are required. The radius of the volumetric heat source is assumed to be twice that of the droplet radius, and the effective height, d, is calculated from the following equation (Refs. 34, 38, 39):

$$d = h_v - x_v + D_d \qquad (7)$$

where h_v is the estimated height of the cavity caused by the impact of metal droplets, x_v is the distance traveled by the center of the two successive impinging droplets, and D_d is the droplet diameter. The total sensible heat input from the metal droplets, Q_d, is given as (Ref. 34)

$$Q_d = \pi\rho_w r_w^2 w_f C_p (T_d - T_l) \qquad (8)$$

where ρ_w is the density of the electrode wire, r_w is the radius of the wire, w_f is the wire feeding rate, T_d is the droplet temperature, and T_l is the liquid temperature.

The values of h_v and x_v in Equation 7 are calculated based on an energy balance as (Ref. 39):

$$h_v = -\frac{2\gamma}{D_d \rho g} + \sqrt{\left(\frac{2\gamma}{D_d \rho g}\right)^2 + \frac{D_d v_d^2}{6g}} \qquad (9)$$

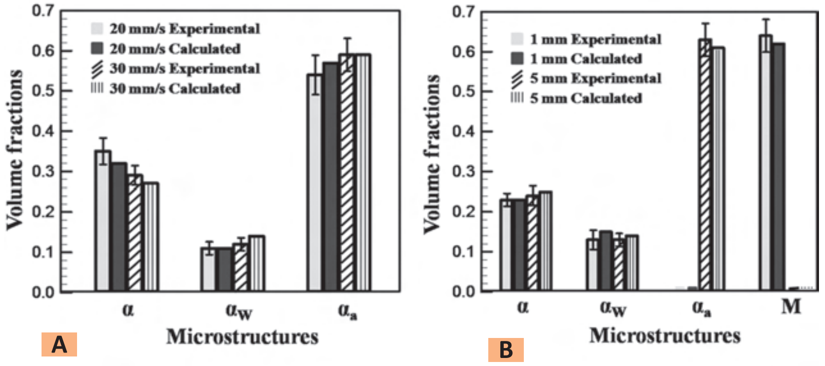

Fig. 12 — Comparison of the experimental and calculated microstructure volume fractions of the weld metal for weld 1 with welding speed of 20.0 mm/s, laser arc separation distance of 1 mm; weld 2 with welding speed of 30.0 mm/s, laser arc separation distance of 1 mm; weld 3 with welding speed of 40.0 mm/s, laser arc separation distance of 1 mm; and weld 4 with welding speed of 40.0 mm/s, laser arc separation distance of 5 mm. The symbols α, α_W, and α_a represent allotriomorphic, Widmanstätten, and acicular ferrite, respectively.

$$x_v = \left(h_v + \frac{2\gamma}{D_d \rho g}\right) \left\{1 - cos\left[\left(\frac{g}{h_v}\right)^{1/2} \Delta t\right]\right\} \qquad (10)$$

where γ is the surface tension of the molten metal, ρ is the density, g is acceleration due to gravity, v_d is the droplet impingement velocity, and Δt is the time interval between two successive drops, which is the inverse of the droplet transfer frequency. As shown in Equations 9 and 10, calculation of the dimensions of the volumetric heat source requires the knowledge of the droplet transfer frequency, radius, and impingement velocity, which can be determined from literature (Refs. 34, 38, 39). From the calculated values of Q_d, D_d, and d, the time-averaged power density of the volumetric heat source, S_v, is calculated as follows (Ref .34)

$$S_v = \frac{Q_d}{\pi D_d^2 d} \qquad (11)$$

Equation 11 is only valid for grid points within the cylindrical heat source, and the power density is zero outside the cylinder. Free surface calculation of the weld top and bottom surface is not considered in the current model, and the simplification of flat pool surfaces is not expected to affect the calculated weld shape and microstructure significantly (Ref. 40).

Phase Transformation Calculation

In the weld fusion zone of low-alloy steels, allotriomorphic ferrite is the first phase to form and it nucleates heterogeneously at the boundaries of the columnar austenite grains during cooling. It is a reconstructive transformation involving diffusion (Ref. 26). As temperature decreases, diffusion becomes sluggish and gives way to a displacive transformation. At relatively low undercoolings, plates of Widmanstätten ferrite form by a displacive mechanism. At further undercoolings, bainite nucleates and grows in the form of sheaves of small platelets. Acicular ferrite nucleates intragranularly around inclusions inside the austenite (Ref. 26). The diffusionless martensite transformation may take place if the cooling rate is high enough.

The isothermal time-temperature-transformation (TTT) and continuous-cooling-transformation (CCT) diagrams together with various transformation starting temperatures are calculated using the phase transformation model based on thermodynamics and phase transformation kinetics with weld deposit compositions as input variables (Refs. 22–24). The incubation times for both reconstructive and displacive transformations are calculated by Russell's expression:

$$\tau = T^a \times \left(\Delta G_{max}\right)^b \times exp\left(\frac{c}{T}\right) \times d \qquad (12)$$

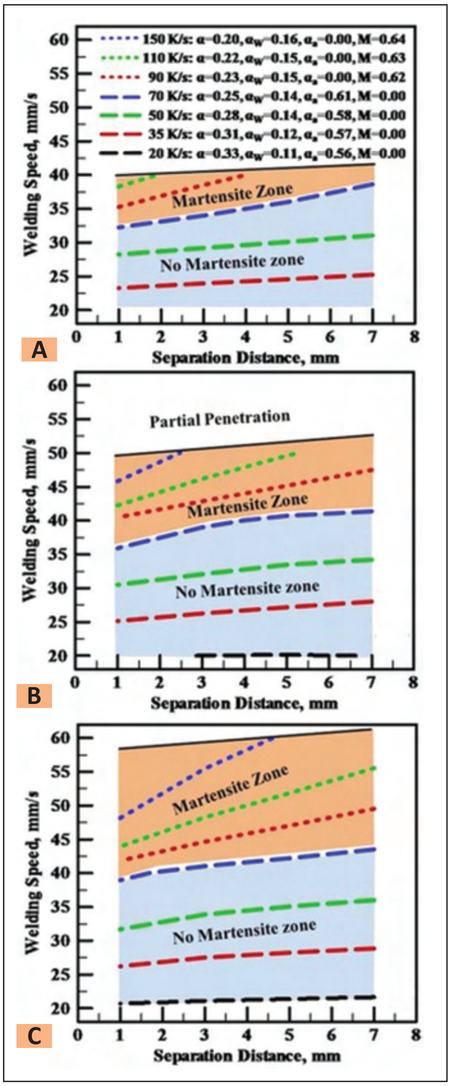

Fig. 13 — Computed volume fractions of allotriomorphic, Widmanstätten, and acicular ferrite, and martensite with corresponding cooling rates from 1073 to 773 K of the fusion zone lower center as a function of laser arc separation distance and welding speed by different laser powers. A — Laser power = 4.0 kW, arc current = 232 A, arc voltage = 31 V; B — laser power = 5.0 kW, arc current = 232 A, arc voltage = 31 V; C — laser power = 6.0 kW, arc current = 232 A, arc voltage = 31 V. The symbols α, α_W, α_a, and M represent allotriomorphic, Widmanstätten, and acicular ferrite, and martensite, respectively.

where τ is the incubation time for a transformation, T is the temperature, ΔG_{max} is the maximum driving force for nucleation, and a, b, c, and d are constants. The details of calculation of ΔG_{max} and determination of a, b, c, and d are given in the literature (Ref. 22).

The CCT diagrams are calculated from the corresponding TTT diagrams based on the Scheil additive rule (Ref. 41):

$$\int_0^t \frac{dt}{t_a(T)} = 1 \qquad (13)$$

where t_a is the incubation time required to reach a specified state on a TTT diagram for isothermal reactions, *t* is the time to that stage for the nonisothermal reactions, and *dt* is the time interval at temperature *T*. In this procedure, the total time to reach a specified state of transformation for nonisothermal reactions is obtained by adding the fractions of time to reach this stage isothermally until the sum reaches unity.

The inclusion of the weld deposit compositions also leads to the calculation of the appropriate part of the phase diagram needed to obtain paraequilibrium compositions for kinetic analysis. These data are combined with austenite grain parameters and the computed cooling curves from the heat transfer and fluid flow model to calculate the volume fractions of allotriomorphic, Widmanstätten ferrite, acicular ferrite, and martensite (Ref. 23). The modeling results are used to better understand the experimentally observed microstructures of the weld metal in complete-joint-penetration hybrid laser-GMA welding.

Results and Discussion

Calculated Temperature and Velocity Fields

The effects of welding speed and laser arc separation distance on weld profiles and temperature and velocity fields are studied separately for complete-joint-penetration hybrid laser-GMA welding. Both these parameters have been shown to significantly affect the weld quality and welding productivity. Figure 1 shows the calculated temperature and fluid flow fields in three dimensions when the welding speed increases from 20 to 30 mm/s with a constant laser arc separation distance of 1 mm. The temperature is indicated by contour lines and the velocity field is represented by arrows. There is an intense temperature gradient on the top and bottom surfaces of the weld pool because the temperature of the liquid metal at the keyhole wall equals the boiling point, while the liquid metal at the weld pool boundary remains at the solidus temperature. The molten metal moves radially outward for both the top and bottom surfaces because of the Marangoni convection produced by the spatial gradient of surface tension resulting from the temperature gradient. The maximum outward flow velocities of the top surface are 155.6 and 194.2 mm/s for welding speeds of 20 and 30 mm/s, respectively. The momentum is then transferred by viscous dissipation to the inner layers of the weld pool adjacent to the surface.

The comparison between these calculated and experimental weld pool geometries is shown in Fig. 2. The top surface width decreases from 9.6 to 7.0 mm, and the bottom surface width decreases from 3.6 to 2.0 mm when the welding speed increases from 20 to 30 mm/s. The boiling point contours indicate the cross-sectional geometry of the keyhole, while the solidus temperature contours indicate the fusion zone boundary. It is observed that the widths of the top and bottom surfaces, as well as the shape of the fusion zone predicted by the heat transfer and fluid flow model, agreed well with the corresponding experimental results. The weld pool dimensions decrease significantly with the increasing welding speed as the top surface widens due to Marangoni convection. Furthermore, the bottom width is also larger than the minimum weld profile width at the middle of the plate thickness, indicating the significant effect of convective heat transfer.

Figure 3 shows the calculated temperature and fluid flow fields when the laser arc separation distance increases from 1 to 5 mm with a welding speed of 40 mm/s. When the laser arc separation distance is changed, the nominal total heat input of the welding process is constant, while the heat input decreases from 0.63 to 0.41 kJ/mm with a welding velocity increase from 20 to 30 mm/s, as shown in Fig. 2. The computed length of the weld pool increases from 18 to 23 mm with the increasing laser arc separation distance. The heat from the laser and arc as well as the droplet is more concentrated near the laser beam incident point at shorter laser arc separation distance. The heat distribution over the top surface of the weld pool significantly changes when the arc axis is further separated from the laser beam. The top part of the liquid weld pool is stretched and the distance along the welding direction from the maximum weld width to the laser beam incidental point is significantly increased.

Figure 4 shows the comparison between these calculated and experimental weld pool geometries. The top surface width increases from 5.1 to 6.8 mm, and the bottom surface width increases from 1.2 to 1.6 mm when the laser arc separation distance increases from 1 to 5 mm. It can be observed from Figs. 1 and 3 that the effects of welding speed and laser arc separation distance on the weld profiles are different. When the welding speed increases from 20 to 30 mm/s, the weld pool shrinks significantly in all locations along the weld depth. However, only the top part of the weld pool significantly increases when the laser arc separation distance increases from 1 to 5 mm. The bottom part has a slight change and the middle part of the weld pool is almost unaffected by the laser arc separation distance. Changes in these processing conditions impact the resulting weld pool geometries in different ways. For example, the increase of the welding speed reduces the net energy absorbed by the workpiece. On the other hand, the increase of the laser arc separation distance mainly influences the energy distribution of the heat sources.

Cooling Rates

The cooling rates over the austenite decomposition range from 1073 to 773 K within the weld fusion zone are calculated using this same heat transfer and fluid flow model. The calculated cooling rates are then used in the modeling of the weld metal microstructures of low-alloy steels. Figure 5 shows the calculated cooling curves between 773 and 1073 K at different locations on the top surface of the weld with a welding speed of 20 mm/s. It can be seen that the cooling rates are almost independent of position. The cooling rates within the fusion zone and the cooling rate in the heat-affected zone (HAZ) are both at a level of approximately 20 K/s. These similarities in cooling rates allow a single cooling condition to be assumed for each horizontal plane across the weld depth.

The comparison of the calculated

cooling curves at the top surface of the fusion zone for welding velocities of 20 and 30 mm/s and a 1-mm separation distance are shown in Fig. 6. The calculated cooling rate between 1073 and 773 K increases from 21.3 to 48.4 K/s with the increasing weld speed. The corresponding cooling times are 14.1 and 6.2 s, respectively. As expected, the cooling rate increases with increasing welding speed and resulting decrease in heat input.

The calculated cooling curves between 1073 and 773 K along the centerline 1.0 mm above the bottom surface of the weld for laser arc separation distances of 1 and 5 mm at a welding speed of 40 mm/s are shown in Fig. 7. This position is chosen because the width of the weld pool is the smallest at this depth, which indicates that the weld metal at this region is more prone to contain martensite. The calculated cooling rates from 1073 to 773 K are 83.3 and 66.7 K/s when the laser arc separation distance increases from 1 to 5 mm. The corresponding cooling times are 3.6 and 4.5 s, respectively. Ribic et al. (Ref. 27) reported that for hybrid laser-GTA welding with heat input of 0.10 kJ/mm, the cooling time from 1073 to 773 K increased from 0.45 to 0.75 s with the increase of laser arc separation distance from 3.5 to 9.2 mm. As can be seen from Fig. 3A, B, the weld pool length increases with the increasing laser arc separation distance. The isothermals also expand for regions beyond the liquid weld pool so that the spatial gradient of temperature decreases for the temperature range from 1073 to 773 K. Therefore, the cooling rate decreases with increasing laser arc separation distance, which is consistent with the result reported by Ribic et al. (Ref. 27).

In order to validate the calculation of the cooling rates between 1073 and 773 K, the calculated cooling rates for different welding conditions are compared with the results available in the literature that examine the effects of changes in heat input and plate thickness on the cooling rate during arc welding (Ref. 42). The literature results show the cooling time from 1073 to 773 K for the welding speeds of 20, 30, and 40 mm/s are approximately 13.1, 6.0, and 3.9 s, compared with the values of 14.1, 6.2, and 3.6 s calculated by the heat transfer and fluid flow model. Therefore, the cooling rates between 1073 and 773 K obtained from the literature and the 3D heat transfer and fluid flow model show good agreement.

Microstructures

The comparison of the fusion zone microstructures located at the top surface of the weld for welding speeds of 20 and 30 mm/s at laser arc separation distance of 1 mm is shown in Fig. 8. For a welding speed of 20 mm/s, the microstructure contains 35% allotriomorphic ferrite, 11% Widmanstätten ferrite, and 54% acicular ferrite. When the welding speed increases to 30 mm/s, the amount of allotriomorphic ferrite decreases to 29%, Widmanstätten ferrite increases to 12%, and acicular ferrite increases to 59%. The average length of the acicular ferrite decreases from 13.1 to 7.1 μm and the width decreases from 3.1 to 1.2 μm when the welding speed increases from 20 to 30 mm/s. The hardness testing results show the microhardness value increases from 223 to 248 HV. The average microhardness of the base metal is 174 ± 11 HV. The differences in microstructure contribute to the higher microhardness of the weld metal with a higher welding speed.

The comparison of the fusion zone microstructures located 1.0 mm above the bottom surface of the weld for a laser arc separation distance of 1 and 5 mm at a welding speed of 40 mm/s is shown in Fig. 9. The volume fraction of martensite is about 64% for the laser arc separation distance of 1 mm, compared with a separation distance of 5 mm when no martensite is present. The amounts of allotriomorphic ferrite and Widmanstätten ferrite are about 23 and 13%, respectively, for 1-mm separation distance. The volume fraction of acicular ferrite is about 63%, and the amounts of allotriomorphic ferrite and Widmanstätten ferrite are about 24 and 13%, respectively, for a laser arc separation distance of 5 mm. The microhardness decreases from 283 to 238 HV when the laser arc separation distance increases from 1 to 5 mm. The higher microhardness indicates martensite is present and signifies a lower toughness of the weld (Refs. 21, 43, 44), which is detrimental to the mechanical properties of the joint.

Figure 10 shows the CCT diagrams computed from the TTT diagram based on the Scheil additive rule, superimposed with the cooling curves at selected locations in the four welds. The cooling curves of the welds with welding speeds of 20 and 30 mm/s at a laser arc separation distance of 1 mm both intercept with the diffusive and displacive transformation curves, so allotriomorphic ferrite, Widmanstätten ferrite, bainite, and acicular ferrite are expected. The cooling curve of the weld with a laser arc separation distance of 1 mm at the welding speed of 40 mm/s intercepts with the upper C curve and the martensite transformation line while the cooling curve for the weld with a laser arc separation distance of 5 mm at the welding speed of 40 mm/s intercepts with both the upper and lower C curves but not the martensite transformation line. As a result, martensite is expected with the laser arc separation distance of 1 mm but not for the laser arc separation distance of 5 mm, although the net heat input of the welding process is identical.

The variation of the calculated volume fractions of allotriomorphic and Widmanstätten ferrite, acicular ferrite, and martensite with cooling rates is shown in Fig. 11. For the composition of DH 36 steel and austenite grain sizes observed in the experimental welds, acicular ferrite is the predominant phase, comprising nearly 60% of the microstructure up to the critical cooling rate for martensite. Widmanstätten ferrite increases with cooling rate at the expense of allotriomorphic ferrite. These two phases combine to make up 40% of the microstructure. The calculated results are consistent with the data reported in previous work (Ref. 24).

Both the experimentally measured and calculated quantitative volume fractions of different phases of the four welds are shown in Fig. 12. Good agreement between the two sets of data is observed. Figure 12A shows the volume fractions of allotriomorphic ferrite and acicular ferrite slightly decrease while Widmanstätten ferrite increases with the increasing welding speed. Figure 12B shows the martensite volume fraction is about 52% when the laser arc separation distance is 1 mm, but no martensite is observed when the laser arc separation distance increases to 5 mm. A very small amount of acicular ferrite is observed experimentally for a laser arc separation distance of 1 mm, compared to 5-mm separation distance when acicular ferrite is the predominant phase.

It should be noted the welding conditions including the heat input are all identical when the laser arc separation distance changes from 1 to 5 mm. The reason for the large difference of the weld metal microstructures with the changing laser arc separation distance lies in the fact that the cooling condition, especially the cooling rate between 1073 and 773 K, significantly decreases when the laser arc separation distance increases from 1 to 5 mm. The cooling rate exceeds the critical cooling rate for martensite transformation with laser arc separation distance of 1 mm while it decreases to a value lower than the critical cooling rate for martensite transformation when the laser arc separation distance increases to 5 mm.

Process Map

In order to further understand the influence of welding parameters on the cooling rates and corresponding volume fractions of the microstructures of the weld fusion zone, a comprehensive process map is presented in Fig. 13. The map considers various combinations of welding speed, laser arc separation distance, and laser power. The arc current and arc voltage are 232 A and 31 V, respectively, for all the welding conditions. The laser powers for Fig. 13A–C are 4, 5, and 6 kW, respectively. The maps show the combinations of separation distance and welding speed that produce a given cooling rate and corresponding microstructure in terms of volume fractions of different phases and microconstituents. The critical cooling rate for martensite transformation is about 71 K/s, which is calculated by the model for microstructure evolution (Refs. 22–24). Cooling rates below 71 K/s are shown in dashed lines as a zone without martensite, while cooling rates greater than 71 K/s are shown in dotted lines as another zone with martensite in Fig. 13. The upper bound on the process maps is the partial penetration line, above which complete penetration is not possible.

In general, welding speed has a greater effect on cooling rate than separation distance, and at low welding speeds of 20 mm/s, the cooling rate is almost independent of separation distance. The effect of power can also be observed in Fig. 13. As power increases, the cooling rates shift to higher welding speeds for a given separation distance. For example, at 1 mm separation distance, the required welding speeds to obtain a 70 K/s cooling rate are 32 and 39 mm/s for 4 kW and 6 kW laser powers, respectively. It is important to know how cooling rates affect the microstructure. As the cooling rate increases from 20 to 150 K/s, the volume fraction of Widmanstätten ferrite increases from 0.10 to 0.22 at the expense of the allotriomorphic ferrite, which decreases from 0.31 to 0.23. The amount of acicular ferrite decreases from 0.59 to 0.57 from low cooling rates up to the critical cooling rate when acicular ferrite disappears and martensite forms instead.

These maps provide a means for understanding microstructure evolution during hybrid laser-arc welding and can be used to select welding parameters that optimize the weld microstructure or minimize welding time yet limit the formation of martensite. For example, as stated previously, if the power is increased from 4 to 6 kW for a constant separation distance of 1 mm, then the welding speed can be increased by 22% from 32 to 39 mm/s without the formation of martensite. Increasing the separation distance from 1 to 7 mm further increases the possible welding speed to 42 mm/s. Compared to the initial conditions in this example, the total increase in welding speed is 31% due to a 33% increase in laser power and a 6-mm increase in separation distance. The welding speed and the resulting time to make a weld are important. When comparing the costs of hybrid laser-GMA welding with conventional arc welding for pipe joining applications, Reutzel et al. (Ref. 45) found that weld time comprised between 24 and 41% of the total fabrication time, depending on pipe diameter, with other tasks, such as fitup, preparation of the weld, and movement of the part, making up the rest of the time. Additionally, since the welding is occurring with the same cooling rate, there would be no change in the microstructure. The utility of the process map indicates significant promise for understanding the evolution of microstructures in the fusion zone of hybrid laser-GMA complete-joint-penetration welding by a combination of phase transformation model and the thermal cycles calculated from the heat transfer and fluid flow model.

Summary and Conclusions

The effect of laser arc separation distance and welding speed on fusion zone geometry and microstructure during complete-joint-penetration hybrid laser-gas metal arc welding of low-alloy steel was investigated experimentally and theoretically. A heat transfer and fluid flow model was used to calculate the weld pool geometry and cooling rates, which were applied to a microstructure model to compute the phase fractions of selected microconstituents. Experimental weld geometries and microstructures were compared to the calculated values, and the two sets of data agreed well. The following conclusions can be drawn from this work:

1. The effect of welding speed and laser arc separation distance on weld pool geometry was investigated in complete-joint-penetration hybrid laser-arc welding. The weld length and width both at the top and bottom of the pool increased with increasing laser arc separation distance for the same heat input. The weld pool dimensions decreased with increasing welding speed as expected.
2. Cooling rate was also affected by the hybrid welding parameters. When the welding speed increased, which changed the net heat input, the cooling rate increased. When the laser arc separation distance decreased, which altered the heat distribution of the combined power sources but not the heat input, the cooling rate increased. At high welding speeds, the decrease in separation distance can have a significant enough effect on the cooling rate to form martensite in the microstructure.
3. The experimental weld microstructures consisted of acicular ferrite, allotriomorphic ferrite, Widmanstätten ferrite, and martensite. Martensite existed only in the weld with the laser arc separation distance of 1 mm and a welding speed of 40 mm/s. Acicular ferrite formed at the expense of martensite when the separation distance increased to 5 mm. Increasing the welding speed from 20 to 30 mm/s resulted in a decrease of allotriomorphic

ferrite and an increase in Widmanstätten and acicular ferrite.

4. Utilizing the combined models, a process map has been constructed that illustrates the effects of welding speed, separation distance, and laser power on cooling rate and microconstituent volume fractions. Identical cooling rates and microconstituent volume fractions can be obtained with various combinations of process parameters. In general, welding speed and laser power have a more significant effect on cooling rates than separation distance; however, at high welding speeds, the separation distance can be the deciding factor for martensite formation.

Acknowledgments

The authors would like to thank Mr. Jay Tressler for performing the hybrid welding experiments, Mr. Ed Good and Dr. Jay Keist for assisting with the metallography, and Prof. Lars-Erik Svensson for assisting with the microstructure identification and quantification. This research was performed using funding received from the DOE Office of Nuclear Energy's Nuclear Energy University Programs under Grant Number 120327.

References

1. Steen, W. M. 1980. Arc augmented laser processing of materials. *Journal of Applied Physics* 51(11): 5636–5640.
2. Tusek, J., and Suban, M. 1999. Hybrid welding with arc and laser beam. *Science and Technology of Welding and Joining* 4(5): 308–311.
3. Page, C. J., Devermann, T., Biffin, J., and Blundell, N. 2002. Plasma augmented laser welding and its applications. *Science and Technology of Welding and Joining* 7(1): 1–10.
4. Chen, Y. B., Lei, Z. L., Li, L. Q., and Wu, L. 2006. Experimental study on welding characteristics of CO_2 laser TIG hybrid welding process. *Science and Technology of Welding and Joining* 11(4): 403–411.
5. Zhou, J., and Tsai, H. L. 2008. Modeling of transport phenomena in hybrid laser-MIG keyhole welding. *International Journal of Heat and Mass Transfer* 51(17-18): 4353–4366.
6. Cho, J. H., and Na, S. J. 2009. Three-dimensional analysis of molten pool in GMA-laser hybrid welding. *Welding Journal* 88(2): 35-s to 43-s.
7. Vollertsen, F., Grunenwald, S., Rethmeier, M., Gumenyuk, A., Reisgen, U., and Olschook, S. 2010. Welding thick steel plates with fibre lasers and GMAW. *Welding in the World* 54(3–4): R62–R70.
8. Le Guen, E., Fabbro, R., Carin, M., Coste, F., and Le Masson, P. 2011. Analysis of hybrid Nd:YAG laser-MAG arc welding processes. *Optics and Laser Technology* 43(7): 1155–1166.
9. Cao, X., Wanjara, P., Huang, J., Munro, C., and Nolting, A. 2011. Hybrid fiber laser-arc welding of thick section high strength low alloy steel. *Materials and Design* 32(6): 3399–3413.
10. Roepke, C., Liu, S., Kelly, S., and Martukanitz, R. 2010. Hybrid laser arc welding process evaluation on DH36 and EH36 steel. *Welding Journal* 89(7): 140-s to 150-s.
11. Bagger, C., and Olsen, F. O. 2005. Review of laser hybrid welding. *Journal of Laser Applications* 17(1): 2–14.
12. Gao, M., Zeng, X. Y., and Hu, Q. W. 2006. Effects of welding parameter on melting energy of CO_2 laser-GMA hybrid welding. *Science and Technology of Welding and Joining* 11(5): 517–522.
13. Rao, Z. H., Liao, S. M., and Tsai, H. L. 2011. Modeling of hybrid laser-GMA welding: Review and challenges. *Science and Technology of Welding and Joining* 16(4): 300–305.
14. Callister, W. D., and Rethwisch, D. G. 2009. *Materials Science and Engineering*. Wiley, U.S.A.
15. Roepke, C., and Liu, S. 2009. Hybrid laser arc welding of HY-80 steel. *Welding Journal* 88(8): 159-s to 167-s.
16. Gao, M., Zeng, X. Y., Hu, Q. W., and Yan, J. 2008. Weld microstructure and shape of laser-arc hybrid welding. *Science and Technology of Welding and Joining* 13(2): 106–113.
17. Moore, P. L., Howse, D. S., and Wallach, E.R. 2004. Microstructures and properties of laser-arc hybrid welds and autogenous laser welds in pipeline steels. *Science and Technology of Welding and Joining* 9(4): 314–322.
18. Swanson, P. T., Page, C. J., Read, E., and Wu, H. Z. 2007. Plasma augmented laser welding of 6 mm steel plate. *Science and Technology of Welding and Joining* 12(2): 153–160.
19. Chen, Y. B., Feng, J. C., Li, L.Q., Chang, S., and Ma, G. L. 2013. Microstructure and mechanical properties of a thick-section high-strength steel welded joint by novel double-sided hybrid fibre laser-arc welding. *Materials Science and Engineering A – Structural Materials Properties Microstructure and Processing* 582: 284–293.
20. Gao, M., Zeng, X. Y., Yan, J., and Hu, Q. W. 2008. Microstructure characteristics of laser-MIG hybrid welded mild steel. *Applied Surface Science* 254(18): 5715–5721.
21. McPherson, N. A., Suarez-Fernandez, N., Moon, D. W., Tan, C. P. H., Lee, C. K., and Baker, T. N. 2005. Laser and laser-assisted arc welding process for DH 36 microalloyed steel ship plate. *Science and Technology of Welding and Joining* 10(4): 460–467.
22. Bhadeshia, H. K. D. H. 1982. Thermodynamic analysis of isothermal transformation diagrams. *Metal Science* 16(3): 159–165.
23. Bhadeshia, H. K. D. H., Svensson, L. E., and Gretoft, B. 1985. A model for the development of microstructure in low-alloy steel (Fe-Mn-Si-C) weld deposits. *Acta Metallurgica* 33(7): 1271–1283.
24. Bhadeshia, H. K. D. H., and Svensson, L. E. 1993. Modeling the evolution of microstructure in steel weld metal. *Mathematical Modeling of Weld Phenomena*. H. Cerjak and K. E. Eastering, eds. Institute of Materials, London, pp. 109–180.
25. Mundra, K., and DebRoy, T. 1996. Numerical prediction of fluid flow and heat transfer in welding with a moving heat source. *Numerical heat transfer, Part A* 29: 115–129.
26. Mundra, K., and DebRoy, T. 1993. Calculation of weld metal composition change in high-power conduction mode carbon-dioxide laser welded stainless steels. *Metallurgical Transactions B – Process Metallurgy* 24(1): 145–155.
27. Ribic, B., Rai, R., and DebRoy, T. 2008. Numerical simulation of heat transfer and fluid flow in GTA/Laser hybrid welding. *Science and Technology of Welding and Joining* 13(8): 683–693.
28. International Institute of Welding (IIW), Guide to the light microscope examination of ferritic steel weld metals. 1991. *Welding in the World* 29: 160–176.
29. Rai, R., Kelly, S. M., Martukanitz, R. P., and DebRoy, T. 2008. A convective heat transfer model for partial and full penetration keyhole mode laser welding of a structural steel. *Metallurgical and Materials Transactions A* 39A: 98–112.
30. Kaplan, A. 1994. A model of deep penetration laser welding based on calculation of the keyhole profile. *Journal of Physics D: Applied Physics* 27: 1805–1814.
31. Zhao, H., and DebRoy, T. 2003. Macroporosity free aluminum alloy weldments through numerical simulation of keyhole mode laser welding. *Journal of Applied Physics* 93: 10089–10097.
32. Wilcox, D. C. 1993. *Turbulence Modeling for CFD* (California: DCW Industries).
33. Launder, B. E., and Spalding, D. B. 1972. *Lectures in Mathematical Models of Turbulence*. London, UK: Academic Press.
34. Zhang, W., Kim, C. H., and DebRoy, T. 2004. Heat and fluid flow in complex joints during gas metal arc welding — Part II: Application to fillet welding of mild steel. *Journal of Applied Physics* 95(9): 5220–5229.
35. Essers, W. G., and Walter, R. 1981. Heat transfer and penetration mechanisms with GMA and plasma-GMA welding. *Welding Journal* 60(2): 37-s to 42-s.
36. Lancaster, J. F. 1984. *The Physics of Welding*. New York, N.Y.: Pergamon Press.
37. Ribic, B., Burgardt, P., and DebRoy, T. 2011. Optical emission spectroscopy of metal vapor dominated laser-arc hybrid welding plasma. *Journal of Applied Physics* 109(8): 083301.
38. Kumar, S., and Bhaduri, S. C. 1994. Three-dimensional finite element modeling of gas metal-arc welding. *Metallurgical and Materials Transactions B* 25B: 435–441.
39. Yang, Z., and DebRoy, T. 1999. Modeling macro- and microstructures of gas-metal-arc welded HSLA-100 steel. *Metallurgical and Materials Transactions B — Process Metallurgy and Materials Processing Science* 30(3): 483–493.
40. Kou, S. 2012. Fluid flow and solidification in welding: Three decades of fundamental research at the university of Wisconsin. *Welding Journal* 91(11): 287-s to 302-s.
41. Takahashi, M., and Bhadeshia, H. K. D. H. 1991. A model for the microstructure of some advanced bainitic steels. *Materials Transactions* 32(8): 689–696.
42. Masubuchi, K. 1980. *Analysis of Welded Structures*. New York, N.Y.: Pergamon Press.
43. Ribic, B., Palmer, T. A., and DebRoy, T. 2009. Problems and issues in laser-arc hybrid welding. *International Materials Reviews* 54(4): 223–244.
44. Sevim, I. 2006. Effect of hardness to fracture toughness for spot welded steel sheets. *Materials and Design* 27(1): 21–30.
45. Reutzel, E. W., Sullivan, M. J., and Mikesic, D. A. 2006. Joining pipe with the hybrid laser-GMAW process: Weld test results and cost analysis. *Welding Journal* 85(6): 66–71.

Appendix E:

Summary of 690 Ductility Dip Cracking Testing Using Gleeble and Digital Image Correlation

Summary of 690 ductility dip cracking testing using Gleeble and digital image correlation

Xinghua Yu, Stan David and Zhili Feng

Oak Ridge National Laboratory

Introduction:

A hot ductility test is commonly used to evaluate ductility dip cracking. In conventional hot ductility tests, the ductility can be only determined from the reduction in cross-sectional area of the specimen, which is an indirect estimation of high temperature ductility. Extensometer can be used to measure the total strain of the specimen. However, due to thermal gradient in the specimen, there is a high temperature and strain gradient on the specimen from the center to the end. Total strain is not a good indication of real ductility. As a result, there is a need to measure local total strain before failure to access ductility. High-temperature digital image correlation (DIC) can be a powerful tool to track in situ development of non-uniform strain and distortion. It is a promising technique to track localized development of strain as a function of time. Current research applied hot ductility test with high temperature DIC to study ductility dip cracking of Alloy 690.

Experimental:

3 690 specimens with 7mm in diameter and 70mm gauge length were machined from a thick-wall tube provided by electric power research institute. Composition of Alloy 690 is listed in Table 1. 2 specimens were annealed in furnace in argon atmosphere at 1100°C for 1 hour. Tensile tests have been performed on both as-machined condition and as- annealed condition with staining rate of 0.0003/s. Hot ductility tests were conducted in a Gleeble® 3500 thermomechanical simulator. The system setup is shown in Fig. 1. Random patterns were created by painting white background and black speckles on to the specimen surface. The sample was heated to 1327°C at 110°C/s and cooled to 871°C at 50°C/s. Load was then applied at a stroke rate of 7mm/s while the temperature was maintained at 871°C. During testing, an in-situ optical image correlation method was used to measure displacement on the surface of an object by tracking random patterns on the samples. Digital cameras (Point Grey GRAS-50S5C-C) linked

with a computer were used for image acquisition. Sigma® lenses (28-300mm f/3.5-6.3 DG) were used for zooming purpose. Since the thermal radiation from the hot sample at elevated temperature will lessen image contrast, therefore results in large errors in DIC, current study adopted monochromatic light illumination and narrow bandpass filter. 3x4 high-brightness green LED array (Visual Instrumentation model 900405, wavelength 530±5nm) and Edmund® 532nm hard-coated bandpass filter (Part number 65155) were used. Images were taken at 0.1 second intervals. Images were post-processed by the Vic-3D® software developed by Correlated Solutions and the strain maps were obtained. A region of interest (ROI) in the middle of each sample, which is about 5 mm by 55 mm in area, was selected for strain analysis.

Table 1. Composition of Alloy 690

C	S	Si	Cu	Mn	Fe	Cr	Ni
0.018	0.0006	0.03	<0.01	0.19	9.67	29.73	Balanced

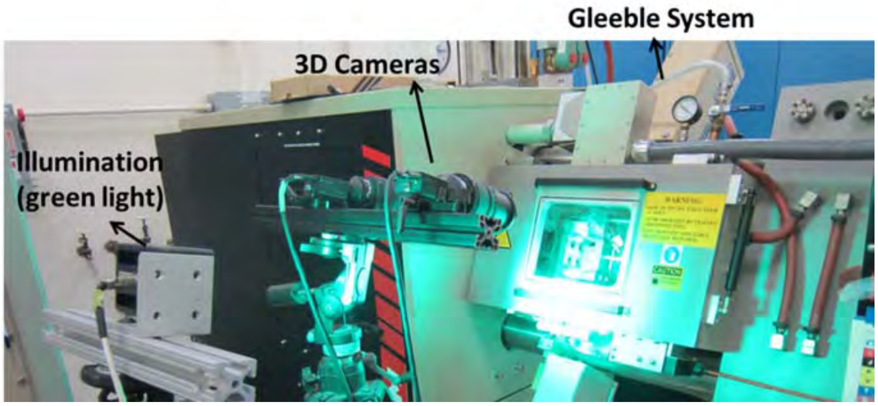

Figure 1. System setup for full field strain measurement during hot ductility test

Results:

Tensile tests: Engineering strain stress curves from tensile tests and hot ductility test are shown in Fig 2. The yield stresses and ultimate tensile stresses have been summarized in Table 2.

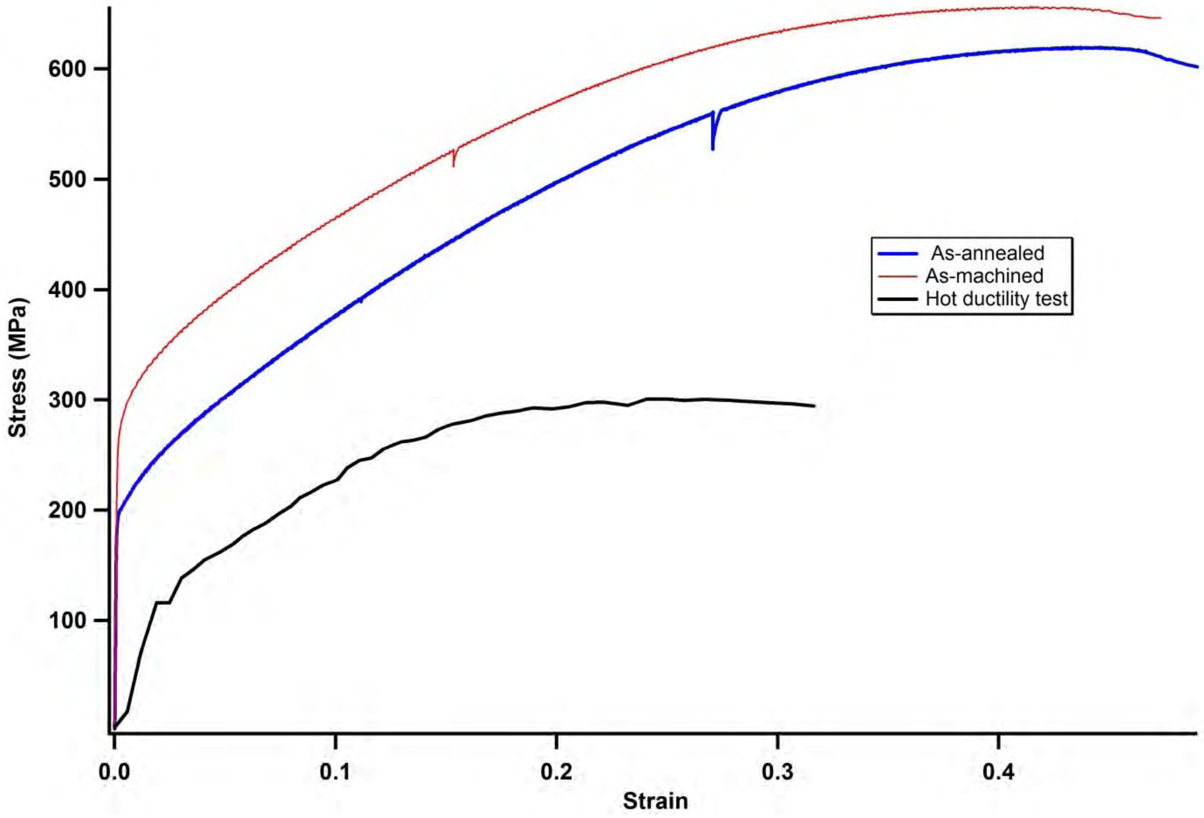

Figure. 2 stress-strain curves for Alloy 690 tensile and hot ductility tests.

Table 2 yield stresses and ultimate tensile stresses for tensile and ductility tests.

	As-machined	As-annealed	Hot ductility
Yield strength (MPa)	280	201	148
Ultimate Tensile Strength (MPa)	646	601	240

DIC results: High temperature DIC with tradition speckle coating technique is capable of obtaining full field strain map at slow strain rate for temperature lower than 1100°C. However, exposure of the organic speckle coating required to measure strain was found to degrade and spall when exposed to high temperatures (871°C) and at a strain rate of 0.1/s. Fig. 3 shows strain maps in the tensile direction (e_{xx}) superimposed with original specimen images at different stages during hot ductility test. Fig. 2a clearly shows good contrast between black speckles and white background at 871°C before tension was applied. Speckle coatings were still bonded to the specimen surface when 0.03 strain is applied. Coatings, however, start to spall when strain reaches 0.05 and correlation calculation cannot proceed anymore.

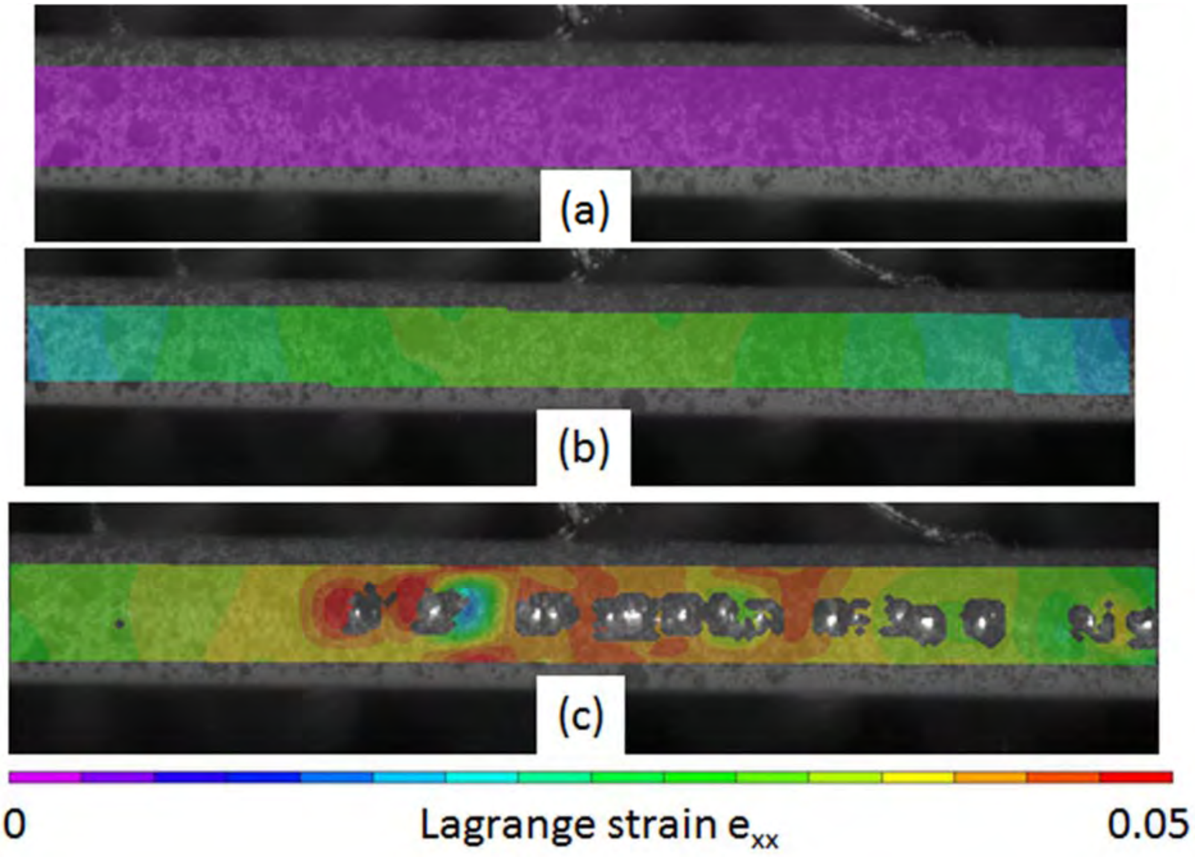

Figure 3. e_{xx} Strain maps of (a) before loading (b) when 0.03 strain was applied (c) when 0.05 strain is applied

Improving coating technique: The problem was overcome at Oak Ridge National Laboratory (ORNL) by modifying the surface condition of the samples and applying very thin coating of the surface speckle patterns. Upon surface treating the paint adheres extremely well on to the specimen. Fig 4 shows the strain map of an annealed Alloy 600 sample with improved coating technique before fracture. The measured local strain was as high as 119%. The current surface treated coating can be used up to 1100°C and can withstand strain rate >0.1/s.

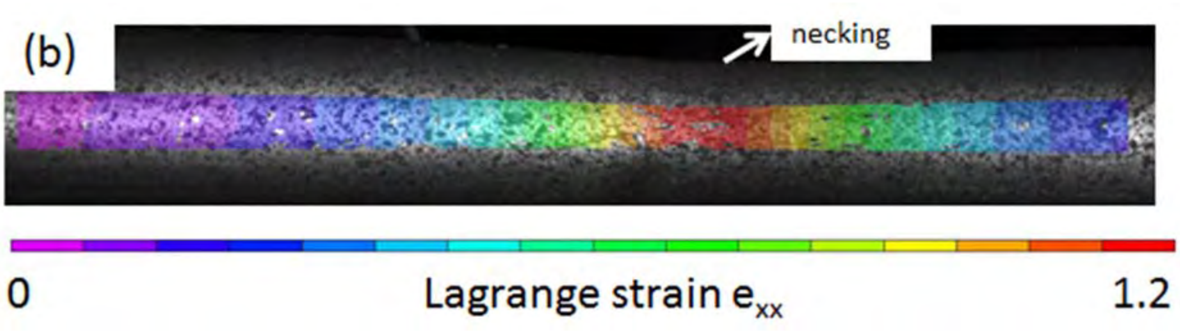
(b)
necking
0
Lagrange strain e_{xx}
1.2

Figure 4. Strain map of an annealed Alloy 600 sample with improved coating showing good speckles up to 1.2 strain

Appendix F:

Porosity in Thick Alloy 690 Welds – Experiments, Modeling, Mechanism, and Remedy

Porosity in Thick Alloy 690 Welds – Experiments, Modeling, Mechanism, and Remedy

J. J. Blecher[1], T. A. Palmer[2], and T. DebRoy[1]

[1]Department of Materials Science and Engineering, The Pennsylvania State University,
University Park, Pennsylvania, 16802, USA

[2]Applied Research Laboratory, The Pennsylvania State University, University Park,
Pennsylvania, 16802, USA

Abstract

Laser welding processes present significant opportunities for thick section welding during the construction and repair of nuclear power plant components. However, the impact of laser-based welding processes on the fusion zone geometry and defect levels in Alloy 690 are not well understood. A series of laser and hybrid laser-arc welds are fabricated with varying laser powers and welding speeds. While the porosity levels attributed to keyhole collapse remain high in the laser welds for all power levels, the addition of the arc in the hybrid laser-arc welds appears to inhibit the presence of the porosity at laser powers in excess of 4 kW. At lower powers, the region where filler metal enters the weld pool at a high speed, is relatively large compared to the overall pool size and inhibits the motion and escape of bubbles, resulting in large amounts of trapped porosity. The dimensions of the volumetric heat source, which serves as a proxy for region where filler metal enters the weld pool, are calculated for various electrode diameters and currents.

I. Introduction

Joining thick sections of Inconel® Alloy 690, a Ni-Cr-Fe alloy, is critical for construction and repair of nuclear power plants [1]. The current joining techniques include submerged metal arc welding (SAW) [2,3] and gas tungsten arc welding (GTAW) [4-6]. These traditional welding processes are widely available, but they are limited by slow welding speeds, high heat inputs, and shallow weld penetrations, which require a large number of passes to fabricate thick section components in excess of 6 mm [4]. On the other hand, laser and hybrid laser-gas metal arc (GMA) welding processes produce deeper penetrations per pass and reduce the total heat input compared to arc welding, limiting distortion and heat affected zone size [7]. In addition, these processes can produce single-pass welds in joints where multipass arc welding would typically be used. However, the effects of laser and hybrid welding on fusion zone geometry and porosity characteristics in Alloy 690 must be characterized before their wider deployment in power plant component fabrication.

Several researchers have investigated the effects of Alloy 690 laser welding on joint geometry [8-13] and porosity [11-13]. These previous studies have been limited to laser powers of 4 kW or less in full penetration welds of 3 mm and partial penetration weld depths of 6 mm or less. In terms of joint geometry, low power laser welds in Alloy 690 have a high depth to width ratio [8-13] with a relatively narrow width and high depth, which is similar to that observed in the laser welding of common structural alloys [14,15]. Thick section joining of Alloy 690 will require higher laser powers and larger penetration depths.

Aside from these attractive weld pool geometries, porosity has been found to be a major obstacle for implementation of laser welding in the fabrication of Alloy 690 joints [11-13]. In general, there are three possible types of porosity during welding. One type of porosity results from high solubility of monatomic and diatomic O, N, and H in molten metal and low solubility in the solid [16]. During solidification, the solubility decreases, gas evolution occurs, and the bubbles become trapped as pores. Pore coalescence is another form of porosity in welds [17] and is found in base metals with high pre-existing levels of porosity, such as die-cast magnesium alloys. For example, Zhao and DebRoy [17] found an increase in porosity compared to the base metal during laser welding of die-cast Mg due to the expansion and coalescence of pre-existing pores during laser welding. The third form of porosity is produced by keyhole instability, where the bottom tip of the keyhole acts as the source of large bubbles, and is limited to high energy beam welding processes [18]. Keyhole porosity is by far the largest cause of macroporosity in laser and hybrid laser-arc welding [19-22].

Several researchers have investigated the effects of laser welding on keyhole porosity in Alloy 690. Kuo et al. [11] found Alloy 690 to be more susceptible to keyhole porosity than AISI 304 stainless steel during pulsed laser welding. Tucker et al. [13] found that optimized values of defocus and welding speed could not fully remove porosity in laser welded Alloy 690. Equilibrium vapor pressure-temperature relations [23,24], such as those shown in Figure 1, may explain why Alloy 690 is more prone to keyhole porosity. An ideal solution is assumed for the calculation of vapor pressure, which is the sum of the product of the alloying element mole fraction and the vapor pressure for the pure substance (i.e. Fe, Cr, Ni, Ti, Al, and V) at each temperature. Near the boiling point at 1 atmosphere, the temperature gradient of vapor pressure is higher for Alloy 690 as compared to other common structural alloys. As a result, small changes in temperature at the keyhole wall, which will be close to the boiling point, will produce larger changes in pressure, resulting in more instability and porosity. Power modulation [10], a defocused beam, and increased welding speeds help to reduce porosity levels in laser welded Alloy 690, but there is no generally accepted methodology for eliminating keyhole porosity. For specific conditions, trial and error optimization and design of experiments may be used to remove porosity. However, such an approach can be time-consuming and overly expensive.

Previous research shows that laser welding has significant difficulty producing defect free welds in Alloy 690. However, hybrid welding processes may have the potential to overcome the inability of autogenous laser welding to produce single pass, thick section, low defect content Alloy 690 joints. This welding method is an especially attractive option for Ni-base alloys because of its ability to add filler metals and to produce weld metal compositions that can promote desirable weld metal properties [25]. Over a range of laser powers and welding speeds, the effects of laser and hybrid laser-gas metal arc welding processes on weld shape and size and porosity formation have been compared. Characterization of porosity in laser and hybrid welds is undertaken using X-ray computed tomography (CT). A mechanism for reducing porosity levels at higher powers is presented. In this physical model, the overall size of the molten pool and the addition of filler metal are suspected to play a role in the porosity characteristics. Calculations of the interaction volume dimensions are made to demonstrate the difference in process parameters.

II. Experimental Methods

Bead on plate laser and hybrid laser-GMA welds were made on 12.7 mm thick Alloy 690 plate. For both the laser and hybrid welds examined here, the same combinations of laser welding conditions were used. A 200 µm diameter transport fiber connected an IPG Photonics® YLR-12000-L fiber laser to a YW50 Precitec® welding head. Within the head, the optics included a 200 mm and 500 mm focal length collimator and focal lenses, respectively. A PRIMES® Focus Monitor beam characterization tool measured the beam diameter at focus and the divergence angle as 0.52 mm and 64 mrad, respectively. The focus position was placed 8 mm below the top plate surface, so the beam diameter at the top surface was 0.73 mm. Consistent with beam characterization studies [26], the beam profile near focus was top hat, while one Rayleigh length (8.1 mm in this case) or more from focus the beam profile had a Gaussian shape. The welding speed and laser power was varied between 10 and 20 mm/s and 2 and 6 kW, respectively.

For the hybrid welds, a Lincoln Electric® Power Wave 455 M/STT power source with a Binzel® WH 455D water cooled welding gun were used. The torch angle was maintained at 15˚ from vertical. A gas mixture of Ar-25% He shielded the weld from the atmosphere at a 2.7 m/hr flow rate. Inconel® Filler Metal (FM) 52 wire with a diameter of 1.1 mm was used as the consumable electrode and is compositionally identical to Alloy 690, as shown in Table 1. The wire feed speed was set to 121 mm/s. The laser-arc separation distance was held constant at 3 mm with the laser leading. The arc voltage was set to 32 V, and the current was estimated as 200 A based on the instantaneous values displayed on the power source, the wire feed speed, and the diameter of the filler metal wire. Standard metallographic techniques were used to prepare and analyze transverse cross section samples of each weld. The samples were electrolytically etched in a 10 wt.% oxalic acid solution.

A General Electric® v|tome|x X-ray computed tomography (CT) system was used to inspect and characterize the internal porosity in each weld. An accelerating voltage of 250 kV and current of 200 µA were used to image the laser welds. Because the hybrid welds were approximately 10 mm wider at the top surface of the weld than the relatively narrow laser welds, the voltage and current were increased to 285 kV and 230 µA, respectively, during characterization of the hybrid weld. In order to image the entire weld volume, the resolution in all directions was 50 µm and 66 µm for the laser and hybrid welds, respectively. DatosX® software reconstructed the individual

X-ray images into a 3D representation. Volume Graphics® VGStudio Max software with the defect detection module measured the sizes and locations of individual pores within the welds.

III. Results and Discussion

The fusion zone geometry is an important characteristic for comparing laser and hybrid welds. For example, the depth of the weld is related to the maximum weldable plate thickness in a single pass, and the width is related to the plate gap bridgeability with higher weld widths allowing for higher tolerances during plate fit-up before welding. Generally, hybrid welds have a greater width than laser welds, while the depths are similar. Transverse weld profiles obtained from a series of laser and hybrid welds produced here are shown in Figure 2. The linear heat input during laser welding was varied between 100 W/mm and 600 W/mm. On the other hand, the heat input during hybrid laser-arc welding was higher with the addition of the arc and ranged between 400 W/mm and 1200 W/mm.

The measured weld pool widths and depths are shown in Table 2. For the laser welds, the widths and depths increase steadily with laser power with maximum widths and depths of 5.9 and 7.6 mm, respectively, at a laser power of 6 kW and a welding speed of 10 mm/s. Hybrid weld depth increases with power up to 9.1 mm, but the width does not increase significantly and ranges from 11.2 to 15.2 mm across the power range from 2 kW to 6 kW. The hybrid weld widths are significantly greater than the laser weld widths due to the addition of the arc, which acts as a broad heat source. The difference in width is 5 mm or more in most cases, but the weld pool depths did not differ significantly between the two processes, although the hybrid welds were about 1 to 2 mm deeper than the laser welds under similar conditions.

Due to the addition of the arc and the increased heat input, the hybrid welds also display a much larger cross-sectional area compared to the laser welds. At laser powers of 2 kW, the influence of the arc on the hybrid weld pool shape is evident [27] and dominates the characteristics of the weld pool. For example, the characteristic shape of a GMA weld is obvious at a welding speed of 20 mm/s, while at the very bottom of the weld, the finger penetration of the laser can be observed. Since the arc parameters are 31 V and about 200 A, the arc power is on the order of 6 kW compared to the 2 kW of the laser. At higher laser powers of 4 and 6 kW, the influence of the arc on the weld pool shape is diminished due to the parity in power of the arc and laser with only the increased width of the arc being evident.

Large pores in the solidified weld metal are formed when bubbles from the bottom of the keyhole become trapped by the advancing solid liquid interface [18]. Using AISI 304 stainless steel as the base metal, Naito et al. [28] found that keyhole induced porosity is reduced but not entirely eliminated in hybrid laser-GTA welding compared to laser welding. The same is true here in the laser and hybrid welds produced as part of this study. A comparison of porosity in laser and hybrid welds (6 kW, 10 mm/s) measured with X-ray CT is shown in Figure 3. X-ray CT provides a high degree of spatial resolution for the precise location and size of pores. The solid metal regions are light colored, while the pores are shown in a darker color. For the laser weld shown in Figure 3, the level of porosity is much greater, with 103 pores identified in the X-ray CT scan with a median pore volume of 0.14 mm^3. The 17 pores in the hybrid weld have a smaller median volume of 0.02 mm^3. Figure 3 shows the superiority of the hybrid welding process in terms of overall porosity compared to the laser welding process. Outside of the start of the weld, which may be on a ‘run-off plate’ in a welding shop, and the weld reinforcement, which can removed in a production environment, there is only one pore in the entire hybrid weld.

Total porosity volume and pore size distributions are important for understanding how and why the porosity characteristics differ in laser and hybrid welds. The total pore volume for a constant weld length (70 mm in this case) shows significance of the overall porosity, while size distributions show how the pore sizes change with welding process and conditions. These porosity characteristics among laser and hybrid welds for a variety of conditions are shown in Figure 4. Clearly, the two highest heat input hybrid welds (i.e. 4 and 6 kW and 10 mm/s) have the lowest porosity values. The 4 kW weld has only 3 pores with two of those being in the weld reinforcement. These same high heat input welding conditions, which would be used for thick section welding of Alloy 690, produce the lowest levels of porosity. The laser welds with the same laser power and welding speed conditions show much higher overall porosity levels, which are up to 90.5 mm^3 in 1600 mm^3 of weld metal. These porosity levels are many times higher than the hybrid welds, which can have porosity values as low as 0.2 mm^3 in 3000 mm^3 of weld metal.

In the 4 and 6 kW cases, porosity decreased when transitioning from laser to hybrid welding. The 2 kW, 10 mm/s hybrid weld does not show the same low porosity as the 4 and 6 kW hybrid welds and, in fact, has a higher porosity than the laser weld made with the same conditions. The same is true in the welds made at a welding speed of 20 mm/s. This difference in behavior may be traced to a combination of filler metal addition and small weld pool volume during the 2 kW welds. The filler metal is entering the molten pool at a relatively high rate of speed, on the order of 1.5 m/s or faster [29]. Bubbles that form near the bottom of the keyhole need to move towards the top of the weld pool to escape. This mobility towards the top is likely hindered by the filler metal entering the pool at a high velocity. In addition, the pool volume is relatively small compared to the higher laser power welds, further limiting the bubble mobility towards the top of the pool.

The size of the filler metal-weld pool interaction zone can be estimated, using a cylindrical volumetric heat source (VHS) model [29,30]. The model assumes that liquid droplets are accelerated from the end of the consumable electrode, strike the molten pool, and transfer heat and momentum to the weld. The height, depth, and energy intensity of the VHS can be calculated based on the material properties and welding parameters. A detailed description of the VHS model is available in the literature [30-32], and the equations necessary for the calculations performed here are available in Appendix A. Knowledge of the relationship between the arc current and droplet detachment frequency is an important component of the calculations. Especially important is the transition current from globular to spray transfer. However, most studies of droplet detachment have focused on mild steel electrodes with little attention paid to other filler metals, such as FM 52. The welding recommendations for spray transfer mode from the FM 52 manufacturer have been used to estimate the transition currents [33]. The transition current for mild steel is around 290 A, so a current of 300 A or greater will lead to spray transfer mode. The recommended parameters for FM 52 suggest the transition current varies between 150 A and 225 A, depending on the electrode diameter.

Using the experimental welding parameters and material properties, the VHS height and width can be computed. The height and width are calculated as 3.7 and 2.1 mm, respectively. The VHS profile has been overlaid on the transverse cross-sections of the 10 mm/s welding speed hybrid welds in Figure 5. As the power increases, the gap between the bottom of the VHS and the bottom of the weld increases from 1 mm to more than 5 mm. The impinging droplet velocity, which is expected to interrupt pore motion through high fluid velocity turbulence, has a value of 1.6 m/s. The maximum calculated fluid flow velocity in a recent study of hybrid welding of steel was less than 0.3 m/s [34], so the high velocity of the impinging droplets would have significant impact on fluid flow in the weld pool and would interrupt the pore motion upwards and out of the pool.

The evidence for this low mobility model can be extracted from Figure 4, which shows a shift to higher pore sizes when going from laser to hybrid welding. This behavior is only seen in the 2 kW welds and suggests that bubbles stay trapped at the bottom of the weld and combine to form larger bubbles before the solidification front traps them as pores. In addition, the bubbles in the hybrid welds should be trapped in the bottom part of the weld and not show a great deal of variation in location distributions if the combination of the filler metal addition and small pool volume are limiting mobility. Figure 6 shows the pore location distributions as a percentage of the total depth in the 2 kW, 10 mm/s laser and hybrid welds along with part of the X-ray CT image. In both welds, more pores are located near the bottom of the weld pool. In the laser weld, the top third of the weld contains 16% of the total number of the pores, but in the hybrid weld, zero pores are found in the same third of the weld.

Since the likelihood of low porosity in the hybrid welds can be related to the distance between the bottom of the VHS and the bottom of the weld, the effects of available welding parameters, such as arc currents, and FM 52 electrode diameters should be compared to determine if certain conditions provide benefits compared to other conditions. Figure *7* shows the effect of arc current (wire feed speed was increased linearly with current for calculation purposes) on VHS height for different filler metal electrode diameters. The solid lines indicate the hybrid weld depths for given linear heat inputs on the right y-axis, so the bottom line represents the 2 kW hybrid weld, which had large amount of porosity. The middle and top line represent the low porosity 4 kW and 6 kW hybrid welds, respectively. The weld depth-heat input relationship from the experimental welds is shown in Figure 7b.

There is a linear increase of VHS height with current with each electrode diameter falling along the same line. According to the graph, the minimum heat input from the laser for low porosity increases with both arc current and electrode diameter. The minimum heat input for the 1.1 mm diameter filler metal was found experimentaly to be 400 J/mm. For the 0.9 and 1.6 mm diameter electrodes, the minimum heat inputs are 240 and 490 J/mm, respectively. For a 10 mm/s welding speed, reasonable laser powers of 5 kW can be used to fabricate low porosity welds up to 7.5 mm in depth with any FM 52 electrode diameter. However, if greater productivity is desired in terms of welding speed or penetration depth, much higher powers will be required. For example, an increase of the welding speed to 20 mm/s would require 10 kW laser power to make pore free welds with 1.6 mm diameter electrodes. Lasers systems with 10 kW of output power are most likely less available and more expensive than systems that can output 5 kW power.

IV. Summary and Conclusions

The characteristics of laser and hybrid laser-gas metal arc welded Alloy 690 with a compositionally identical filler metal have been analyzed for several processing conditions. The transverse fusion zone geometries and porosity resulting from keyhole collapse have been compared and found to have significant differences, which affect the choice of welding process. The following conclusions were drawn from this work.

1. Due to the arc, which acts as a distributed heat source, the fusion zones in the laser and hybrid welds differ significantly. At the top of the plate, hybrid welds are wider by 8 to 10 mm for similar laser powers and welding speeds. Laser welds are also shallower by 1 to 2 mm compared to hybrid welds fabricated with an identical welding speed and laser power.
2. Total porosity amounts were reduced to the lowest levels in the hybrid welds at powers of 4 kW and 6 kW and a welding speed of 10 mm/s. A minimum porosity total of 0.2 mm^3 in a total weld volume of 3000 mm^3 was found in a hybrid weld with 4 kW laser power and 10 mm/s welding speed. In contrast a laser weld made at a power of 6 kW and a travel speed of 10 mm/s displayed a porosity volume of 90.5 mm^3 in 1600 mm^3 of weld metal.
3. A transition from high levels of porosity to virtually no porosity was observed in the hybrid welds as power increased above 2 kW. Filler metal transfer and low weld pool volume at 2 kW laser power is expected to limit bubble mobility upwards out of the pool. As the power increases, the size of the filler metal interaction relative to the weld pool decreases, allowing the bubbles to more easily escape. Evidence of this mechanism was a shift in the pore size distribution to larger pores when going from hybrid to laser welding and more pores located at the bottom of the pool in hybrid welding compared to laser welding.
4. Calculations, which account for the current-volumetric heat source dimensions relation, laser heat input-weld depth relation, and filler metal 52 electrode dimensions, were used to determine the minimum laser heat input to produce a pore-free hybrid weld for a given electrode diameter. The minimum heat input varied between 240 and 490 J/mm with greater heat inputs required for larger electrode diameters. With welding speeds of 10 mm/s or less, no more than 5 kW laser power would be required to produce pore free welds with every

electrode diameter. Increasing welding speed or current to improve productivity or filler metal deposition would require higher laser powers.

Based on the results of this study, hybrid welding is recommended for welding thick sections of Alloy 690, especially at laser powers above 2 kW. The large amounts of porosity in the laser welds are mostly eliminated when the arc is added to the process. With optimized process parameters, this minimal porosity could be eliminated completely.

Acknowledgments

The authors would like to thank Mr. Jay Tressler for performing the welding experiments and Mr. Ed Good for preparing the metallographic and X-ray specimens. This research was performed using funding received from the DOE Office of Nuclear Energy's Nuclear Energy University Programs under Grant Number 120327.

References

[1] T. Allen, J. Busby, M. Meyer, and D. Petti, "Material challenges for nuclear systems", Mater. Today, **13**, 14-23 (2010).

[2] H.T. Lee and T.Y. Kou, "Effects of niobium on microstructure, mechanical properties, and corrosion behavior in weldments of alloy 690", Sci. Technol. Weld. Joining, **4**, 246-256 (1999).

[3] S.-L. Jeng, H.-T. Lee, J.-Y. Huang, and R.-C. Kou, "Effects of Nb on the microstructure and elevated-temperature mechanical properties of Alloy 690-SUS 304L dissimilar welds", Mater. Trans., **49**, 1270-1277 (2008).

[4] H.T. Lee and T.Y. Kou, "Analysis of microstructure and mechanical properties in alloy 690 weldments using filler metals I-82 and I-52", Sci. Technol. Weld. Joining, **4**, 94-103 (1999).

[5] H.T. Lee and S.L. Jeng, "Characteristics of dissimilar welding of alloy 690 to 304L stainless steel", Sci. Technol. Weld. Joining, **4**, 225-234 (2001).

[6] S.L. Jeng, H.T. Lee, T.E. Weirich, and W.P. Rebach, "Microstructural study of the dissimilar joints of alloy 690 and SUS 304L stainless steel", Mater. Trans., **48**, 481-489 (2007).

[7] B. Ribic, T.A. Palmer, and T. DebRoy, "Problems and issues in laser-arc hybrid welding", Int. Mater. Rev., **54**, 223-244 (2009).

[8] J.J. Blecher, C.M. Galbraith, C. Van Vlack, T.A. Palmer, J.M. Fraser, P.J.L. Webster, and T. DebRoy, "Real time monitoring of laser beam welding keyhole depth by laser interferometry", Sci. Technol. Weld. Joining, **19**, 560-564 (2014).

[9] H.T. Lee, C.T. Chen, and J.L. Wu, “3D numerical study of effects of temperature field on sensitization of Alloy 690 butt welds fabricated by gas tungsten arc welding and laser beam welding”, Sci. Technol. Weld. Joining, **15**, 605-612 (2010).

[10] J.J. Blecher, T.A. Palmer, and T. DebRoy, “Solidification map of a nickel-base alloy”, Metall. Mater. Trans. A, **45A**, 2143-2151 (2014).

[11] T.-Y. Kuo, “Effect of pulsed and continuous Nd-YAG laser beam waves on welding of Inconel alloy”, Sci. Technol. Weld. Joining, **10**, 557-565, (2005).

[12] T.-Y. Kuo and Y.-D. Lin, “Effects of different shielding gases and power waveforms on penetration characteristics and porosity formation in laser welding of Inconel 690 alloy”, Mater. Trans., **48**, 219-226 (2007).

[13] J.D. Tucker, T.K. Nolan, A.J. Martin, and G.A. Young, “Effect of travel speed and beam focus on porosity in alloy 690 laser welds”, JOM, **64**, 1409-1417 (2012).

[14] W.J. Suder and S. Williams, “Power factor model for selection of welding parameters in CW laser welding”, Opt. Laser Technol., **56**, 223-229 (2014).

[15] L. Quintino, A. Costa, R. Miranda, D. Yapp, V. Kumar, and C.J. Kong, “Welding with high power fiber lasers – a preliminary study”, Mater. Des., **28**, 1231-237 (2007).

[16] S. Kou, “Welding Metallurgy”, John Wiley & Sons, Inc., Hoboken, NJ (2003).

[17] H. Zhao and T. DebRoy, “Pore formation during laser beam welding of die-cast magnesium alloy AM60B – mechanism and remedy”, Weld. J., **80**, 204s-210s (2001).

[18] A. Matsunawa, J.D. Kim, N. Seto, M. Mizutani, and S. Katayama, “Dynamics of keyhole and molten pool in laser welding”, J. Laser Appl., **10**, 247-254 (1998).

[19] S. Katayama, Y. Kobayashi, M. Mizutani, and A. Matsunawa, “Effect of vacuum on penetration and defects in laser welding”, J. Laser Appl., **13**, 187-192 (2001).

[20] Y. Kawahito, M. Mizutani, and S. Katayama, “Elucidation of high-power fibre laser welding phenomena of stainless steel and effect of factors on weld geometry”, J. Phys. D: Appl. Phys., **40**, 5854-5859 (2007).

[21] M. Pastor, H. Zhao, R.P. Martukanitz, and T. DebRoy, “Porosity, underfill and magnesium loss during continuous wave Nd:YAG laser welding of thin plates of aluminum alloys 5182 and 5754”, Weld. J., **78**, 207s-216s (1999)

[22] H. Zhao and T. DebRoy, “Macroporosity free aluminum alloy weldments through numerical simulation of keyhole mode laser welding”, J. Appl. Phys., **93**, 10089-10096 (2003).

[23] W. F. Gale, 2004. *Smithells metals reference book, 8th Edn.* Burlington, MA, Elsevier Butterworth-Heinemann.

[24] C.L. Yaws, “The Yaws handbook of vapor pressure: Antoine coefficients”, Houston, TX, Gulf Publishing Company, 2007.

[25] N.E. Nissley and J.C. Lippold, “Ductility-dip cracking susceptibility of nickel-based weld metals part 1: strain-to-fracture testing”, Weld. J., **87**, 257s-264s (2008).

[26] J.J. Blecher, T.A. Palmer, S.M. Kelly, and R.P. Martukanitz, “Identifying performance differences in transmissive and reflective laser optics using beam diagnostic tools”, Weld. J., **91**, 204s-214s (2012).

[27] Z. Yang and T. DebRoy, “Modeling macro-and microstructures of gas-metal-arc welded HSLA-100 steel”, Metall. Mater. Trans. B, **30**, 483-493 (1999).

[28] Y. Naito, S. Katayama, and A. Matsunawa, “Keyhole behavior and liquid flow in molten pool during laser-arc hybrid welding”, Proc. SPIE, **4831**, 357-362 (2003).

[29] L.A. Jones, T.W. Eagar and J.H. Lang, “A dynamic model of drop detaching from a gas metal arc welding electrode”, J.Phys.D:Appl.Phys., **31**, 107–123 (1998).

[30] C.-H. Kim, W. Zhang and T. DebRoy, “Modeling of temperature field and solidified surface profile during gas metal arc fillet welding”, J.Phys.D:Appl.Phys.,**94**, 2667-2679 (2003).

[31] J.F. Lancaster, “The physics of welding”, 2nd Edition, Oxford, Pergamon, 1986.

[32] S. Kumar and S.C. Bhaduri, “Three-dimensional finite element modeling of gas metal-arc welding”, Metall. Mater. Trans. B, 25B, 435-441 (1994).

[33] Special Metals Corporation, “Joining”, accessed 30 April 2015, pg. 9, <www.specialmetalswelding.com>.

[34] H.L. Wei, J.J. Blecher, T.A. Palmer, and T. DebRoy, “Fusion Zone Microstructure in Full Penetration Laser-Arc Hybrid Welding of Low Alloy Steel”, Weld. J., **94**, 135s-144s (2015).

[35] S. Rhee and E. Kannatey-Asibu Jr.,”Observation of metal transfer during gas metal arc welding”, Weld. J., **71**, 381s-386s (1992).

Appendix A

Calculation of Volumetric Heat Source Dimensions

The volumetric heat source (VHS) calculation assumes a cylindrical shape with dimensions of diameter and height. The VHS is commonly used to model consumable electrode heat transfer during gas-metal arc welding [30,32]. In these experiments, spray metal transfer, where small droplets form at the end of the electrode and accelerate into the molten pool, is expected. Several variables are required for the calculation, including material properties, welding parameters, and droplet frequency.

The height of the VHS is given as

$d = h_v - x_v + D_d$

where h_v is height of the cavity formed by the impinging droplets, x_v is the distance traveled in the cavity by each droplet before the arrival of the next impinging droplet, and D_d is the droplet diameter. The cavity height is

$$h_v = \left(-\frac{2\gamma}{D_d \rho g} + \sqrt{\left[\left(\frac{2\gamma}{D_d \rho g} \right)^2 + \frac{D_d v_d^2}{6g} \right]} \right)$$

where γ is surface tension of the liquid metal, ρ is the liquid metal density, g is acceleration due to gravity, and v_d is the droplet impingement velocity. The surface tension and density of FM 52 were taken as 1.1 N/m and 6500 kg/m^3, respectively. The distance traveled by each droplet is defined as

$$x_v = \left(h_v + \frac{2\gamma}{D_d \rho g} \right) \left\{ 1 - cos \left[\left(\frac{g}{h_v} \right)^{1/2} \Delta t \right] \right\}$$

where Δt is the time interval between the impingement of two droplets and can be defined as $\Delta t = 1/f$. The frequency of droplets, f, is

$$f = \frac{-243.44}{1 + exp\left(\frac{I - I_t}{6.06437} \right)} + 323.506 - 0.874I + 0.0025I^2$$

where I (A) is current and I_t is the transition current from globular to spray transfer. The transition current for FM 52 has been estimated based on the suggested process parameters by the electrode manufacturer [33]. The frequency current relations are shown in Figure A1 for three FM 52 electrode diameters and, for reference [29,35], a fitted line to experimental data for mild steel. The droplet shape is assumed to be spherical, and the radius of the sphere is expressed as

$$r_d = \sqrt[3]{\frac{3}{4} r_w^2 w_f / f}$$

where r_w is the radius of the filler metal wire and w_f is the wire feed speed. The VHS diameter is four times the droplet radius. The droplet velocity is

$$v_d = \sqrt{v_0^2 + 2aL_a}$$

where v_0 is the initial velocity, a is the droplet acceleration, and L_a is the arc length. Arc length was assumed to be 3 mm. Acceleration is taken as

$$a = \frac{3}{8}\frac{v_g^3\rho_g}{r_d\rho}C_d + g$$

where v_g is the velocity of the plasma, ρ_g is the density of the plasma, and C_d is the drag coefficient. The plasma density was taken as 0.06 kg/m^3. The velocity of the plasma is estimated with the effective velocity (in m/s), which is

$$v_{eff} = k_1 \times I$$

where k_1 is a constant coefficient of ¼. The drag coefficient is

$$C_d = -242.74Re^{-2} + 59.67Re^{-1} + 0.44793$$

where Re is the Reynolds number, which is defined as

$$Re = \frac{r_d v_{eff}}{\nu_k}$$

The variable ν_k is kinetic viscosity and is 3.4 x 10^{-3} m^2/s. The initial velocity is calculated as

$$v_0 = \sqrt{-0.33692 + 0.00854(I/D_d)}$$

Table 1: Composition of the Alloy 690 base metal and filler metal 52.

	Ni	Cr	Fe	Mn	Si	Ti	Al	Cu	C
Alloy 690	59.80	29.63	9.65	0.28	0.36	0	0	0.25	0.03
FM 52	60.88	29.22	8.65	0.24	0.14	0.38	0.4	0.01	0.02

Table 2: Summary of weld widths and depths as a function of laser power, welding speed, and welding technique.

		Width (mm)		Depth (mm)	
Power (kW)	Speed (mm/s)	Laser	Hybrid	Laser	Hybrid
2	10	3.7	13.6	3.5	4.7
4	10	4.5	15.1	5.7	7.0
6	10	5.9	15.2	7.6	9.1
2	20	2.7	12.4	2.7	3.5
4	20	3.6	11.2	4.7	5.8
6	20	4.4	11.6	6.2	7.6

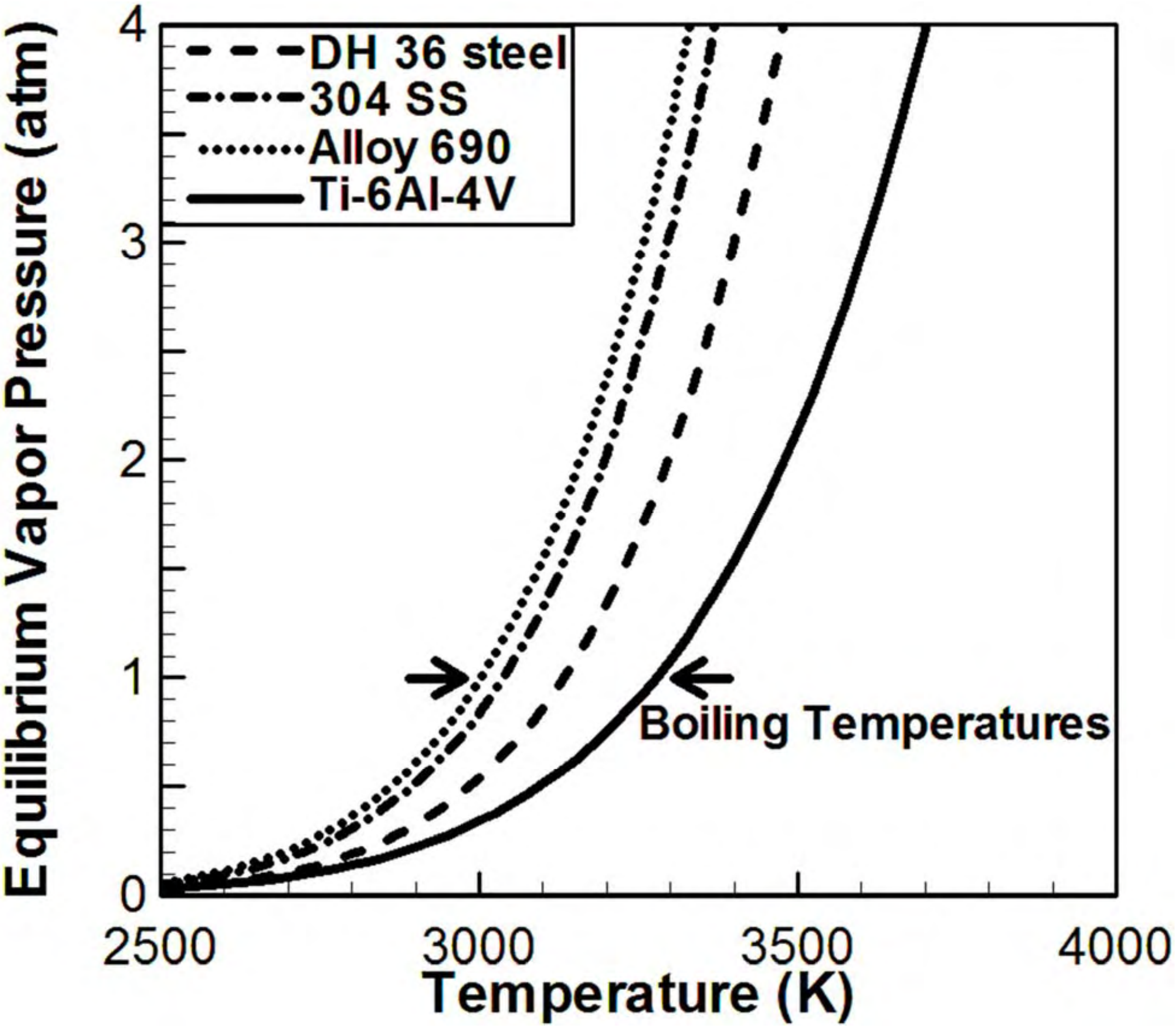

Figure 1: The vapor pressure-temperature relations may explain why increased porosity is observed in Alloy 690 welds compared to other common engineering alloys.

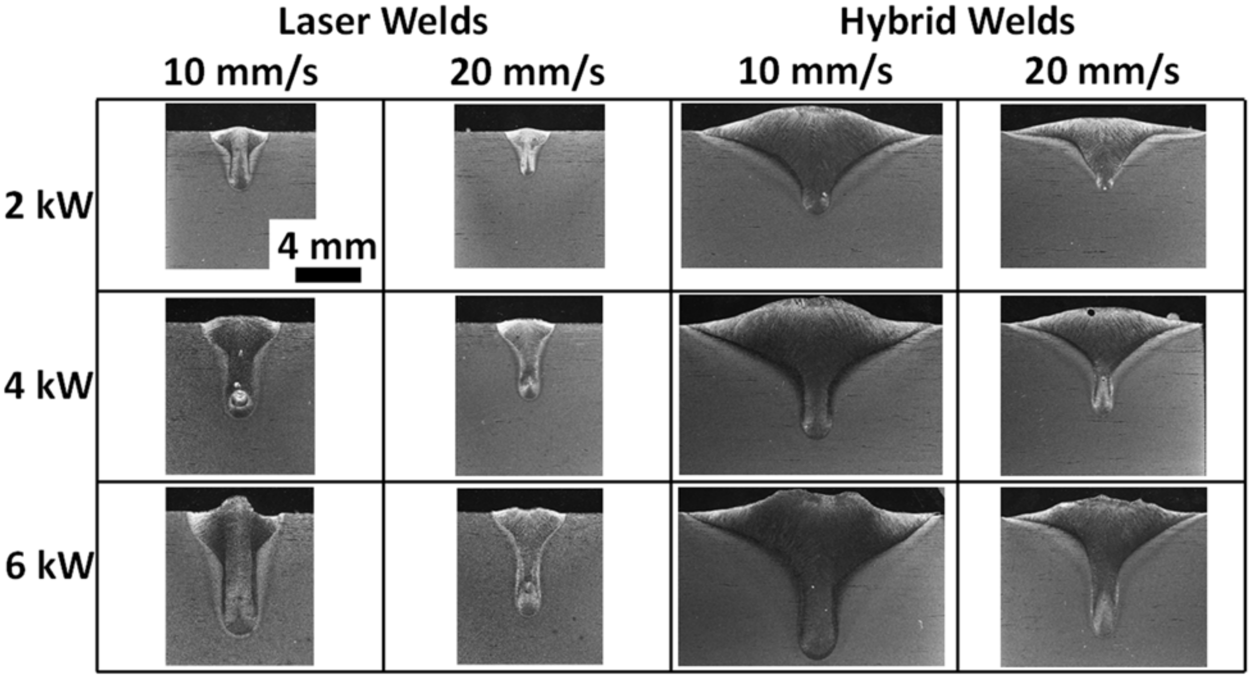
Laser Welds
Hybrid Welds
10 mm/s
20 mm/s
10 mm/s
20 mm/s
2 kW
4 kW
6 kW
4 mm

Figure 2: Laser and hybrid laser-weld transverse cross-sections of Alloy 690 are shown. The additional heat source in the hybrid welds produces much larger and lower aspect ratio welds.

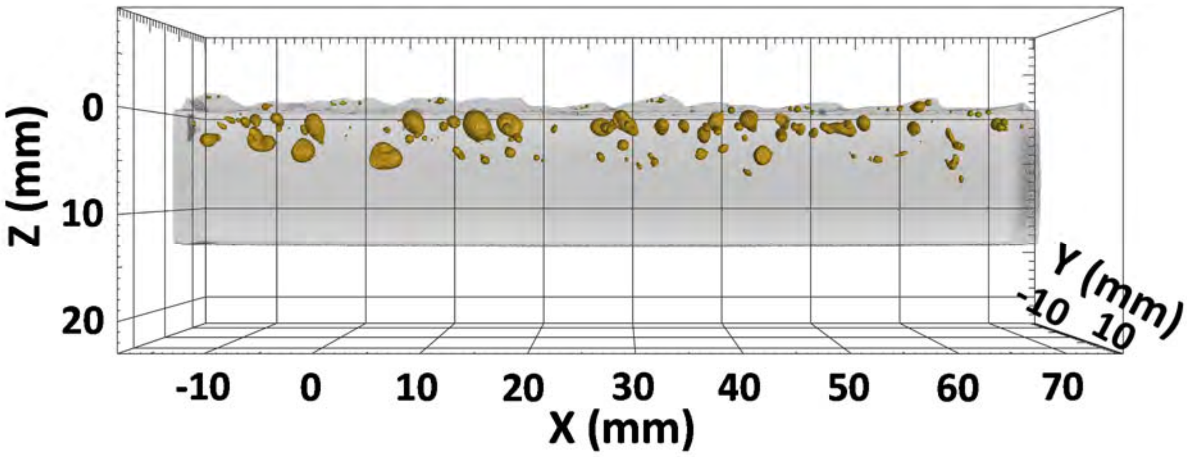
Z (mm)
0
10
20
Y (mm)
-10
10
-10
0
10
20
30
40
50
60
70
X (mm)

(a)

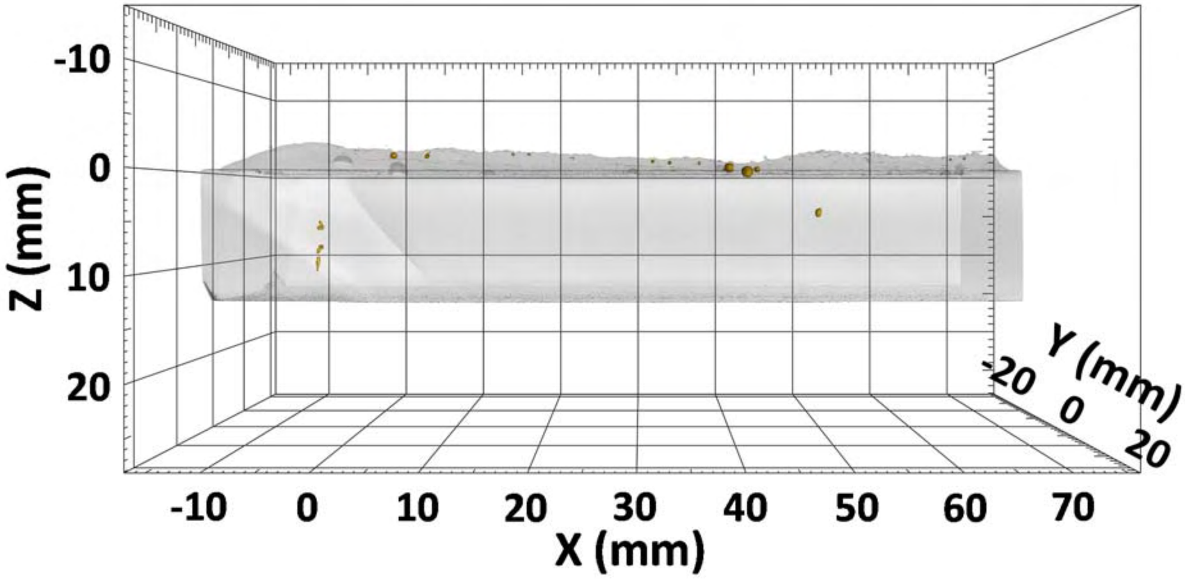
Z (mm)
-10
0
10
20
Y (mm)
-20
0
20
-10
0
10
20
30
40
50
60
70
X (mm)

(b)

Figure 3: X-ray CT scans reveal the porosity in 6 kW 10 mm/s (a) laser welds and (b) hybrid welds. Hybrid welding appears to significantly reduce the amount of porosity in the weld. Include welding conditions.

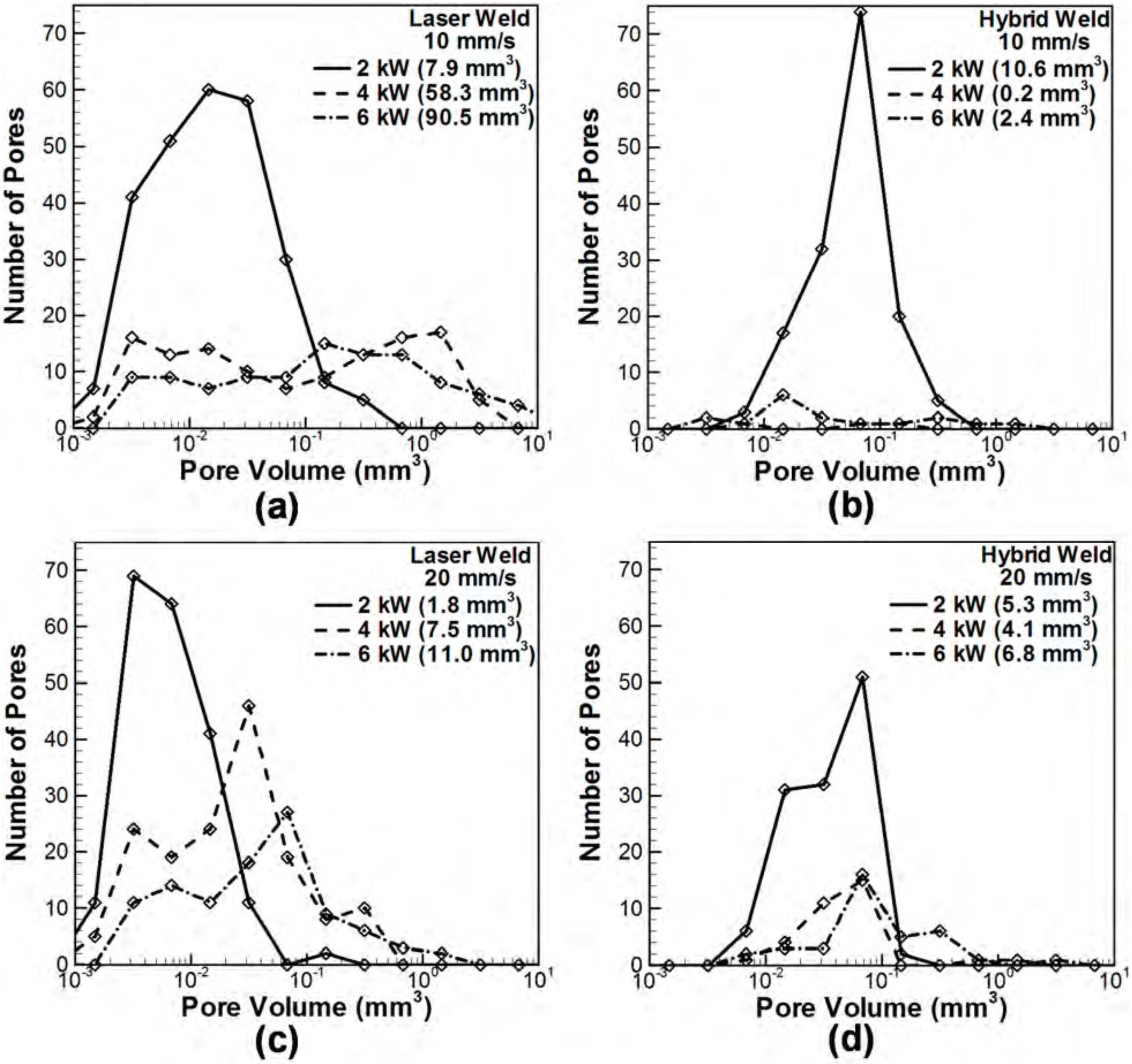

Figure 4: The porosity size distributions for (a and c) laser welds and (b and d) hybrid welds and the total porosity volumes in parentheses are shown. The number of pores for almost all sizes decrease when going from laser to hybrid welding at laser powers of 4 and 6 kW.

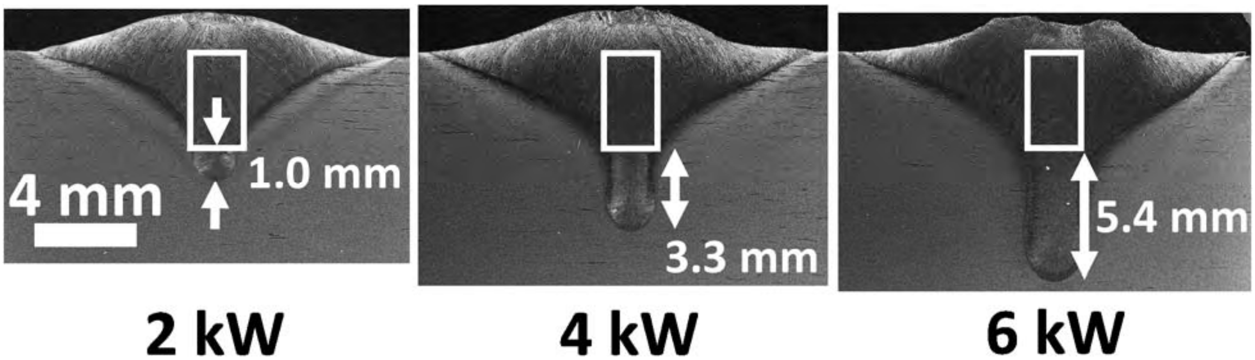

2 kW **4 kW** **6 kW**

Figure 5: The calculated cylindrical volumetric heat source outline is overlaid on the 10 mm/s hybrid welds. The gap between the bottom of the heat source and weld bottom becomes increasing larger with laser power. The larger gap combined with a larger of weld volume behind the gap led to more pores escaping in the 4 and 6 kW welds.

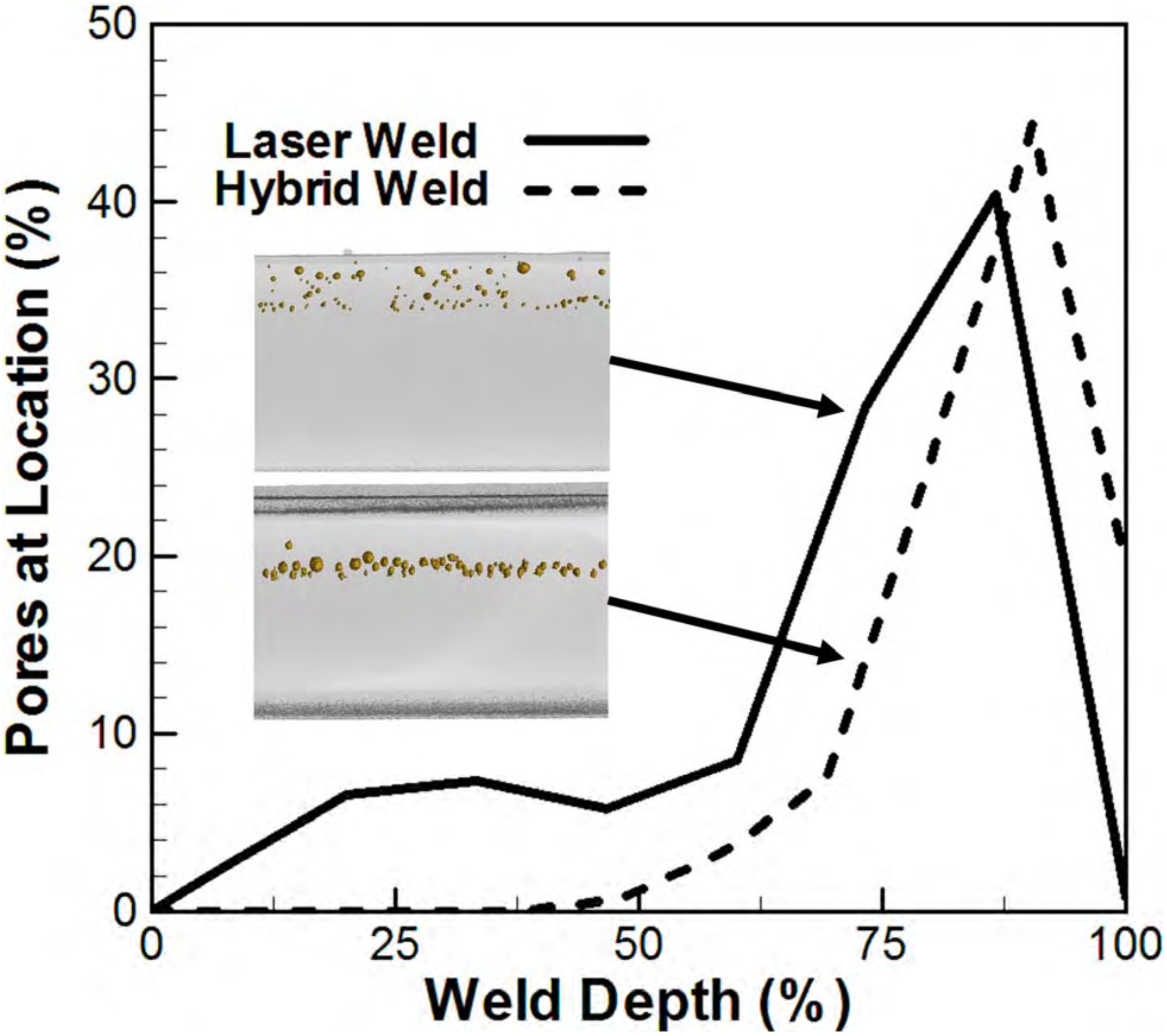

Figure 6: The pore location distributions in laser and hybrid welds for 2 kW of laser power and 10 mm/s welding speed are shown.

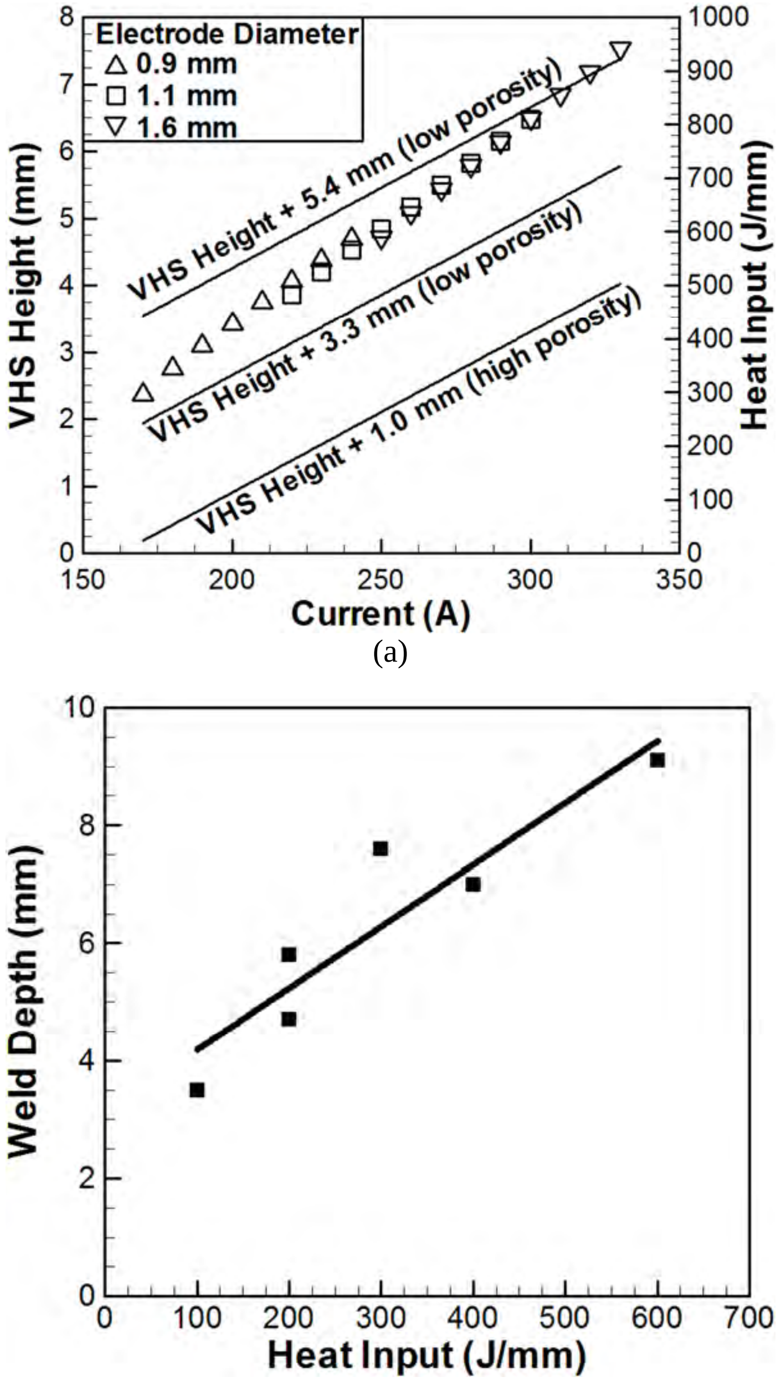

(a)

(b)

Figure 7: The volumetric heat source height for different arc currents and electrode diameters are shown in (a). The laser heat inputs to provide different porosity values is also shown in (a). The relation between weld depth and laser heat input used in (a) is shown in (b).

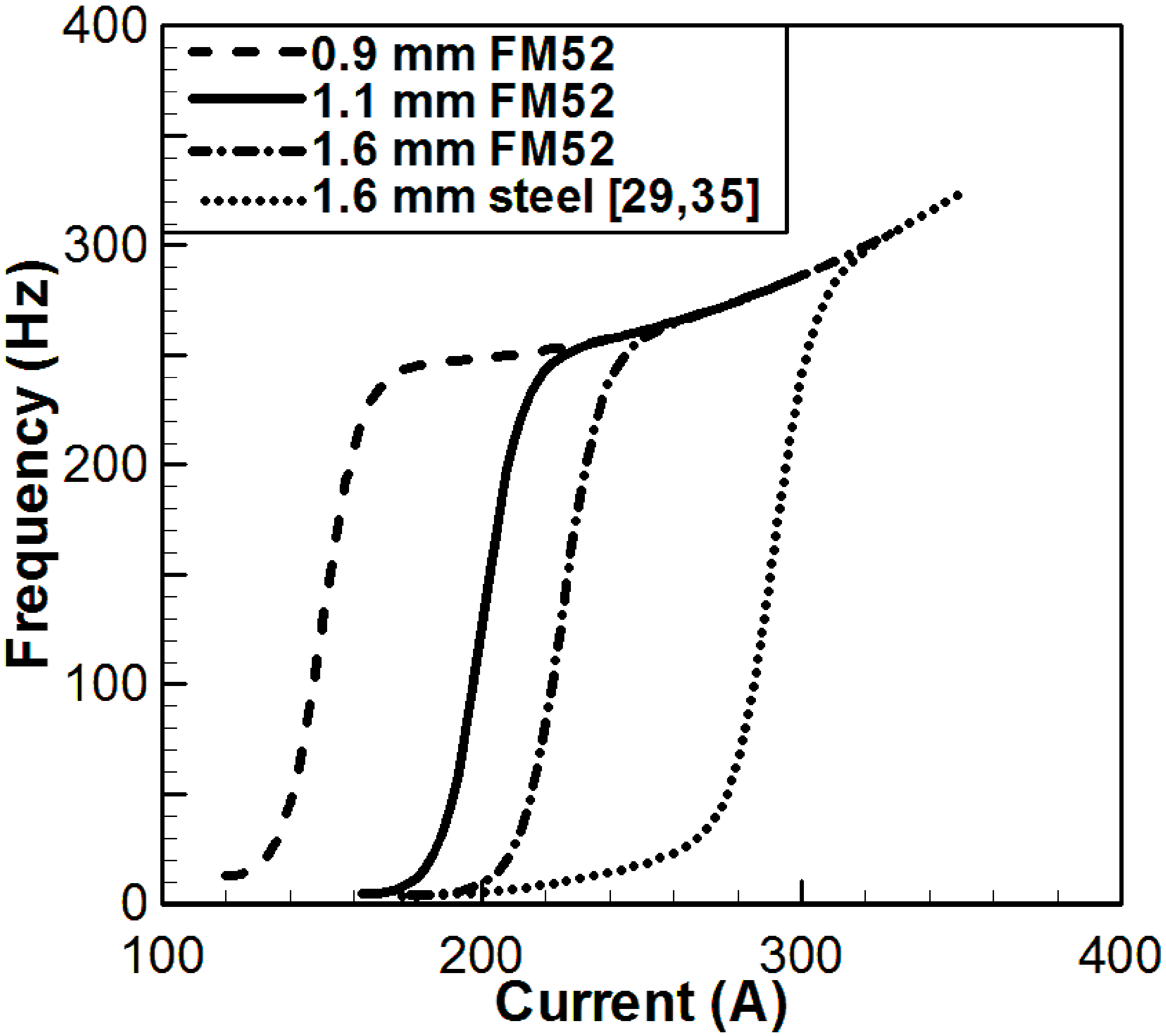

Figure A1: The current-droplet detachment frequencies for filler metal 52 are not experimentally known. Based on suggested currents, voltages, shielding gases, and wire feed speeds for different electrode diameters from the manufactures, the relations have been estimated. The fit line for experimental data [29,35] for steel in Ar-5%CO2 shielding gas is shown for reference.